SCUOLA DI DOTTORATO

UNIVERSITÀ DEGLI STUDI DI MILANO-BICOCCA

Department of Earth and Environmental Sciences

PhD program in Chemical, Geological and Environmental Sciences

Cycle XXXVII

Curriculum: Geological Sciences

Micro and Nanoscale Study of Calcium and Rare Earth Element Fluorcarbonates: Establishing a Link Between Mineral Structure and Genesis

Conconi Roberto

Registration number: 813836

Supervisor: Prof. Giancarlo Capitani

Tutor: Prof.ssa Maria Luce Frezzotti

Coordinator: Prof. Marco Giovanni Malusà

ACADEMIC YEAR 2024

Abstract

This thesis focuses on the mineralogical and crystallographic study of (Ca-REE) fluorcarbonates, particularly on bastnäsite-synchysite polysomatic series. These minerals are the primary ores for rare earth elements (REE), which are crucial for modern technologies such as electric vehicles, wind turbines and solar panels. The global demand for REE is rapidly increasing, especially in the European Union, where REE are classified as critical raw materials due to high supply risk and economic importance. The growing demand for REE highlights the need for exploring alternative and more sustainable extraction methods, including the recovery of REE from secondary sources, such as mining waste, due to environmental concerns associated with traditional extraction processes, which produce radioactive waste and generate high CO_2 emissions.

Despite the importance of REE, unanswered questions remain regarding their behaviour in natural systems, particularly the mechanisms governing REE transport and deposition, which are still poorly understood. In this regard, polysomatic series like the (Ca-REE) fluorcarbonates provide a unique opportunity to study these processes, as their intergrowth patterns can reflect changes in the conditions of crystallization, particularly fluid composition and temperature. This thesis employs a multi-methodological approach, integrating various techniques such as Raman spectroscopy, scanning electron microscopy (SEM) and transmission electron microscopy (TEM) coupled with energy dispersive spectroscopy (EDS), electron backscattered diffraction (EBSD), single crystals X-ray diffraction (SCXRD) and precession-assisted three-dimensional electron diffraction (3DED) to explore the micro- and nanostructure of (Ca-REE) fluorcarbonates.

Initially, the potentialities of Raman spectroscopy and EBSD in the microscopic characterization of (Ca-REE) fluorcarbonates were evaluated to provide a "road map" for further investigations using TEM. EBSD was effective to establish the sample orientation, to setup the oriented cuts and to ascertain the effective syntactic relationship among all the detected (Ca-REE) fluorcarbonates, but it failed to distinguish between different polysomes. Micro-Raman spectroscopy, performed on samples with different orientations, pre-determined by EBSD and characterized by SEM-EDS, allowed the distinction of polysomes based on the differences in intensity and position of the symmetric stretching vibration (v_1) of the carbonate group (CO_3^{2-}), in the region around 1080-1099 cm^{-1}. However, as evidenced by TEM-EDS, what appears as a homogeneous polysome in backscattered electrons (BSE) images, may actually be a disordered intergrowth of compositional faults, with bulk composition matching that of a real polysome only by coincidence. Therefore, while the Raman signal is sensitive to different Ca/(Ca+REE) ratios, it is not sensitive to the ordered distribution of Ca-poor and Ca-rich lamellae within the analyzed volume, complicating the unambiguous identification of polysomes. Additionally, the observed microstructure suggests a primary growth mechanism in which fluorcarbonates crystallize from a fluid close to thermodynamic equilibrium, with conditions that quickly and repeatedly crossed the parisite–bastnäsite stability boundary, rather than a stepwise approach toward thermodynamic equilibrium.

Then, a variety of (Ca-REE) fluorcarbonates with different morphologies and compositions were studied: i) synchysite-(Ce) forming hexagonal prisms and rosette-like aggregates; ii) bastnäsite-(Ce) forming blocky aggregates; iii) bastnäsite-(Nd) forming desert rose-like intergrowths and iv) combinations of synchysite-(Ce) and bastnäsite-(Nd) forming more complex micro and nanostructures. These minerals are thought to form from hydrothermal fluids in a temperature range between 350 and 100 °C. After an investigation spanning from the microscale to the atomic scale, a possible scenario for their formation was proposed. It is assumed that the different (Ca-REE) fluorcarbonates crystallized sequentially, under decreasing temperature and increasing fluid fractionation, with synchysite-(Ce) forming first, followed by bastnäsite-(Ce) and finally bastnäsite-(Nd). The different morphologies, in this case, besides being influenced by the dominant REE in the fluid, were also affected by varying temperatures and cooling rates. The study highlights that nature may efficiently separate REE from one another, like Y from La, Ce and Nd; Ce from Nd and La. Additionally, Th, a radioactive and toxic element, seems to enter the structure of (Ca-REE) fluorcarbonates during the final stages of crystallization. The understanding of these natural processes may suggest routes for improving current metallurgical separation processes.

Finally, a focused study on synchysite-(Ce) was performed to determine its structure and microstructure, with the objectives of: (i) comparing the structural and microstructural data of synchysite-(Ce) from Cuasso al Monte with the limited available literature; (ii) comparing SCXRD and 3DED structural data, with 3DED being applied to this mineral group for the first time; and (iii) gathering insights into crystal growth and REE fractionation. The findings revealed a complex microstructure with numerous defects and inhomogeneities, including polytypic disorder, chemical zoning, hematite inclusions, and fluid inclusions, suggesting a possible growth mechanism through screw dislocations, with later stages marked by a fluid enriched in Y and Th.

Overall, this study provides insights into how different polysomes form and evolve, indicating clues regarding fluid chemistry during crystallization, partitioning of REE and crystallization pathways. Indeed, intergrowths reflect the dynamic conditions of REE mineral formation, where different REE phases precipitate under changing environmental conditions. Moreover, the work sheds light on the role of polysomatism and polytypism in controlling REE mobility in hydrothermal systems, with implications for ore genesis.

Index

Chapter 1
Introduction

1.1 Outline of the thesis

This section provides an overview of the thesis structure.

Chapter 1 – Introduces the thesis topic and explains the project rationale. It also presents the state of the art regarding REE, their transport and deposition in natural hydrothermal systems, and (Ca-REE) fluorcarbonates, including their structure and significance.

Chapter 2 – Provides a detailed description of the methodologies applied in this thesis, including the various analytical techniques used and their operating conditions.

Chapter 3 – Presents the results of the study of (Ca-REE) fluorcarbonates from Mount Malosa (Malawi). The materials were analysed using a combination of SEM-EDS, TEM-EDS, Raman spectroscopy, and EBSD. Notably, EBSD was applied to (Ca-REE) fluorcarbonates for the first time. This approach aims to assess the potential of Raman spectroscopy and EBSD in the microscopic characterization of the material and to provide a roadmap for further, focused investigations, such as the determination of new polysomes using TEM.

Chapter 4 – Presents the results of the study of (Ca-REE) fluorcarbonates from Cuasso al Monte (Western Southern Alps, Italy). Various (Ca-REE) fluorcarbonates with different morphologies and REE contents were observed, leading to the hypothesis of a possible crystallization pathway for their formation.

Chapter 5 – Provides an in-depth study of synchysite-(Ce) focusing on its structure, investigated by SCXRD and 3DED, as well as its microstructure as revealed by Raman spectroscopy, SEM- and TEM-EDS. The characterization revealed a complex microstructure with defects and inhomogeneities.

Chapter 6 – Concludes the thesis by summarizing the key findings and implications of the research.

1.2 Purpose of the thesis

The development towards green technologies in order to establish the basis for a low-carbon future is leading to the increase of the demand of critical raw materials (CRM) (Vidal et al., 2013). Indeed, green and renewable technologies such as wind turbines, electric vehicles and solar panels require a large quantity of CRM, including rare earth elements (REE), platinum group metals (PGMs), Li and Co, among others.

In the European Union (EU), a list of CRM is drawn up every three years, with the latest version published in 2023, comprising 34 materials or groups of elements (European Commission, Study on the Critical Raw Materials for the EU 2023 – Final Report). In order to be considered a CRM an element must have both a high supply risk and high economic importance. The supply risk is largely influenced by the geopolitical scenarios and market conditions. The REE group are those with the highest supply risk. Indeed, the majority of REE are produced by non-EU countries. An example is China, which not only is the main producer of REE (86% of the world total demand), but it is also the biggest supplier for the EU (85% and 100% for light-REE and heavy-REE, respectively).

For these reasons and because it is estimated that the demand of REE will constantly grow in the next decades, innovative methods for extracting REE, particularly from secondary sources, are necessary (Peiravi, 2021). REE are generally exploited from high grade and high tonnage ore bodies like magmatic-hydrothermal or placer deposits (primary sources); or from recycling and extractive waste (secondary source). Primary sources despite having a high content of REE have a series of problematics, such as the presence of radioactive elements often associated to the ore minerals, the huge amount of CO_2 emission for the extraction processes and the use of acidic solution for the recovery, separation and purification of REE. Moreover, because of the increasing demand of REE the mining product itself would not be able to satisfy the future demand. For this reason, there is the necessity to extract REE from secondary sources and implement a more sustainable mining (Herrington, 2021; Zhou et al., 2017). Among the secondary sources, recycling is not still an option, at least in the short and middle terms. At present, the current recycling rate of REE is less than 1%. This is mainly because of the technological difficulties in separating different REE, due to their similar chemical behaviour. Thus, an alternative could be the recovery of REE from the extractive waste of mining activities. However, the potential of extractive waste as a resource have been highlighted only recently and further studies are necessary to assess their feasibility (Dino et al., 2020).

There are over 200 mineral species containing REE, but only a few contain enough REE to have the potential for forming economic ore deposits (Kanazawa and Kamitani, 2006). The primary ore minerals for REE are: REE-carbonates, -fluorcarbonates and -phosphates like bastnäsite, parisite, synchysite monazite and xenotime. However, despite the economic importance of REE and their bearing minerals, a lot of unanswered questions about the mechanisms that govern the REE transport and deposition in natural systems, as well as the crystallization of REE-bearing phase survive. These challenges arise from the difficulty of replicating the complex natural conditions in the laboratory and the inherent challenge of separating different REE. In this regard, it is universally recognized, as well as often forgotten, that fundamental research is the nourishment of applied research. Indeed, mineralogical and crystallographic studies on REE-bearing minerals may shed light on their nature and genesis, eventually suggesting more successful prospection routes, enhanced metallurgical processes and recycling strategies. For these reasons (Ca-REE) fluorcarbonates (hereafter CRFC) have been identified as the ideal mineral group on which conducting mineralogical and crystallographic studies. The interesting characteristic of CRFC, is that they form a polysomatic series, where bastnäsite and synchysite are the end members, and different intermediate polysomes, such as parisite and röntgenite, have been identified over the years. The study of polysomatism is particularly significant, as the intergrowths of different polysomes may indicate changes in crystallization conditions or fluid composition (Gysi and Williams-Jones, 2015).

In this thesis, various CRFC samples from different localities and geological settings were studied using multiple techniques. The goal was to link their micro- and nanostructures to the large-scale geological processes responsible for their formation. Indeed, micro- and nanoscale observations proved fundamental in fully characterizing these minerals and provided important insights into the possible crystallization mechanisms of CRFC. These findings aim to

contribute valuable knowledge to the understanding of the complex processes behind the crystallization of these minerals.

1.3 The Rare Earth Elements

The term rare earth elements refers to a group of seventeen elements in the periodic table. This group includes fifteen lanthanides: lanthanum (^{57}La), cerium (^{58}Ce), praseodymium (^{59}Pr), neodymium (^{60}Nd), promethium (^{61}Pm), samarium (^{62}Sm), europium (^{63}Eu), gadolinium (^{64}Gd), terbium (^{65}Tb), dysprosium (^{66}Dy), holmium (^{67}Ho), erbium (^{68}Er), thulium (^{69}Tm), ytterbium (^{70}Yb) and lutetium (^{71}Lu); as well as yttrium (^{39}Y) and scandium (^{21}Sc), which are considered REE due to their similar geochemical behaviours to the lanthanides.

The REE are generally divided into two distinct groups based on their size and mass: light-REE, which range from La to Sm; and heavy-REE, which range from Eu to Lu, plus Y. Instead, Sc, even if considered a REE, does not belong to any of the aforementioned classes. All REE exhibit similar geochemical behaviours, and this similarity arises from their electronic structure. Indeed, as one progresses across the series, electrons are added to the 4*f* orbital, while the outer electron shells, which are involved in chemical reactions, remain unchanged. Moreover, as protons are added to the nucleus, the resulting stronger nuclear attraction leads to a reduction in ionic radius, a phenomenon known as "lanthanides contraction" (Henderson, 1984). This reduction in size affects the coordination number, which in turn influences mineral structure and substitutional capabilities. Fractionation can occur when minerals preferentially incorporate either light-REE or heavy-REE.

Despite their name, most REE are not particularly rare. For example, Ce, the most abundant REE (~66 ppm, average upper crust abundance), is more common than both Cu and Pb. However, the challenge lies in locating high-grade and high-tonnage ore bodies because REE do not form pure metals and are always found together in deposits.

REE deposits can be found in various geological settings, with the most common being those of mixed magmatic-hydrothermal or purely hydrothermal origins. These include carbonatites, alkaline igneous rocks, and other hydrothermal deposits, where REE are typically found in late-stage hydrothermal veins or as replacement mineralization (Ngwenya, 1994; Williams-Jones et al, 2000; Horie et al., 2010; Wang et al., 2020). Bayan Obo in China, currently the world's largest REE deposit, is an example of such a deposit (Wang et al., 2020). These deposits are often preferred over primary magmatic deposits because they contain minerals like REE-carbonates, -fluorcarbonates, and -phosphates, which are easier to process. Additionally, primary magmatic deposits are less common. A notable example is Mountain Pass (Mariano and Mariano, 2012), once the leading global source of REE, where REE are often into rock-forming minerals such as apatite, allanite, zircon, plagioclase and fluorite, which are more complex to process compared to REE-carbonates. Additionally, sedimentary deposits like placers, laterites, and ion-adsorption clays are important, particularly the latter due to their high heavy-REE content and the ease of mining and processing.

1.4 Transport and precipitation mechanism of REE in hydrothermal fluids

More than 200 mineral species contain REE, but REE are the primary components in only a few. The most significant of these are REE-carbonates and -fluorcarbonates.

Despite the importance of these minerals, the mechanisms responsible for their crystallization are poorly understood. When it comes to the formation of any metal deposit, two key processes need to be comprehended: the form in which the metal is transported (its speciation) and the solubility of the minerals into which it will precipitate. The availability of ligands (anionic species) necessary for forming solution complexes or causing precipitation is determined by the chemistry of the fluid, which is influenced by various factors such as the fluid source, temperature, pressure, pH, mixing with other fluids, or interactions with surrounding rocks. Many of these factors are interrelated.

Determining the behaviour, such as the speciation, of REE in hydrothermal fluids has proven challenging. For this reason, early studies were done on low temperature aqueous fluids (i.e. Wood, 1990). These studies assessed the ionic strength of various REE-ligand combinations, such as REE-chloride, -fluoride, -carbonate and -sulphate complexes in these fluids. The results generally align with the Pearson's Rule (Pearson, 1963), which predicts that the stability of REE complexes with monovalent ligands increases in the order: $F^- > OH^- > NO_3^- > Cl^-$. Instead, for complexes with divalent ligands, the stability order is: $CO_3^{2-} > SO_4^{2-} > P_2O_5^{2-}$. In an effort to explain REE speciation and behaviour in hydrothermal fluids responsible for REE mineral deposition, results from studies on low-temperature aqueous fluids were extrapolated to temperatures up to 300°C. The extrapolation revealed patterns similar to those observed at low temperatures and became widely used in the literature (e.g., Ngwenya, 1994; Salvi and Williams-Jones, 1996; Forster, 2001). The interpretation of these results led many researchers to hypothesize that REE are typically transported as fluoride complexes, with mineral deposition occurring when these complexes are destabilized following interaction with Ca-rich fluids or Ca-bearing rocks.

Over the past 20 years, high-temperature and high-pressure experiments have been conducted at temperatures up to ~500°C (e.g., Migdisov et al., 2002; Migdisov and Williams-Jones, 2007; Migdisov et al., 2008). Although many of these results aligned with those predicted by low-temperature extrapolation, some significant differences emerged. Among these, high temperature experiments highlighted that the extrapolated data significantly overestimated the stability of REE fluoride complexes, with the discrepancy increasing with both temperature and atomic number (Migdisov and Williams-Jones, 2007; Williams-Jones et al., 2012; Migdisov and Williams-Jones, 2014). Conversely, REE chloride species displayed similar behaviour to REE fluorides, but their stability was much lower. Indeed, it has now been established that the stability ranges of REE fluoride complexes closely align with those of REE fluoride solids, indicating that the transport of REE via these complexes is limited by the low solubility of the corresponding solid fluorides. Consequently, REE are likely transported in hydrothermal fluids primarily as chloride complexes rather than fluoride complexes (e.g., Migdisov and Williams-Jones, 2014; Migdisov et al., 2016). However, the existence of fluoride-bearing minerals still necessitates some soluble fluoride complexes, which in some

systems is proposed to exist as undissociated hydrofluoric acid (HF). This HF can dissociate when fluid conditions, such as pH or temperature, change. Although data on the solubility of REE-carbonates and -fluorcarbonates, as well as the strength of REE-carbonate complexes, are limited, carbonate ions are suggested to play a key role as depositional ligands, given the prevalence of REE-fluorcarbonate minerals like bastnäsite.

Another crucial point in REE mobility is the impact of ligand availability. A frequently cited mechanism for inducing chemical changes in a solution is the increase in pH through the dissolution of carbonate rocks (Ngwenya, 1994). This not only alters the pH but also introduces dissolved carbonate ions, which are essential for the precipitation of REE-carbonates and -fluorcarbonates. Indeed, Williams-Jones and Wood (1992) noted that the formation of different CRFC cannot be driven solely by changes in fluoride activity, but also requires variations in Ca^{2+} and CO_3^{2-} activities. Gysi and Williams-Jones (2015) further explored these interactions by studying the thermochemical characteristics of natural bastnäsite-(Ce) and parisite-(Ce) across a temperature range of 50 to 750°C. Their findings were employed to create a detailed fluid-mineral stability diagrams for bastnäsite, parisite, fluocerite, and calcite. These diagrams highlight the significant influence of temperature, pH, and the activity of F^-, Cl^-, Ca, and REE on the stability zones of these minerals.

1.5 The (Ca-REE) fluorcarbonates

From a crystallographic and a mineralogical perspective, the CRFC belonging to the bastnäsite-synchysite group form a polysomatic series (Veblen, 1991). The terms of this series have a layered structure in which $REECO_3F$ and $CaCO_3$ layers alternate with different stacking arrangements along the **c**-axis, producing intermediate polysomes between the two end members, which are bastnäsite [$REE(CO_3)F$)] and synchysite [$CaREE(CO_3)_2F$]. Thus, the intermediate members of this series can be expressed as bastnäsite (*B*) and synchysite (*S*) modules with the polysomatic stoichiometry given as (B_mS_n) and their chemical composition calculated as $[REE(CO_3)F]_m{\cdot}[CaREE(CO_3)_2F]_n$. Intermediate named terms are parisite [$CaREE_2(CO_3)_3F_2$], or (*BS*), and röntgenite [$Ca_2REE_3(CO_3)_5F_3$], or (BS_2). Additional ordered B_mS_n stacking sequences have been described by high-resolution transmission electron microscopy (HRTEM) studies (van Landuyt and Amelinckx, 1975; Wu et al., 1998; Meng et al., 2001a, 2001b, 2002; Ciobanu et al., 2017; Capitani, 2019, 2020). Table 1.1 reports all the B_mS_n phases observed so far. A peculiar characteristic of the bastnäsite-synchysite series is that pure phases are rare. Indeed, they commonly form microscale syntactic (crystallography oriented) intergrowths (Donnay and Donnay, 1953) of different polysomes and/or polytypes.

The term “syntaxy” was introduced to describe an oriented intergrowth of two mineral species with the same chemical composition (Ungemach, 1935). Thus, it was considered a special case of epitaxy. However, the definition proposed by Ungemach (1935) seemed quite limiting to Donnay and Donnay (1953). For this reason, they proposed to broaden the definition by abandoning the condition of identical chemical compositions and applied it to CRFC. The fact that the occurrence of polycrystals in CRFC is the rule rather than the exception is an expression of the inability of the $CaCO_3$ – $REECO_3F$ system to form solid solutions (Donnay and Donnay, 1953). Thus, one phase precipitates until the conditions in the solution have changed sufficiently for the next compound to separate out, which then crystallizes on the original

crystal. Since two or more phases alternate, a discontinuous and periodic change in the fluid composition must be postulated. Therefore, it appears that syntactic intergrowths are the equivalent of zoning in crystal-chemical systems that cannot form solid solutions.

Due to this recurrent microstructure, structural analysis by single crystal X-ray diffraction (SCXRD) were possible only for a few, pure, basic polysomes such as bastnäsite (Ni et al., 1993), parisite (Ni et al., 2000) and synchysite (Wang et al., 1994). Apart from these fortunate cases, for most of the occurrences with intergrowths at the nanoscale, reliable structural analysis can be performed only via TEM.

The crystal structure of bastnäsite has an hexagonal symmetry with space group *P-62c* (Ni et al., 1993), while parisite and synchysite are monoclinic with space group *C2/c* or *Cc* and *C2/c*, respectively (Ni et al., 2000; Wang et al., 1994). The breaking of the hexagonal symmetry and the reduction to a monoclinic cell is due to the insertion of Ca layers, which leads to a shift in the CO_3 layers with respect to the position that they have in the bastnäsite structure (Ni et al., 1993, 2000; Capitani, 2020).

1.6 Polysomatism and polytypism in (Ca-REE) fluorcarbonates

Polysomatism can be described as intergrowth structures (Veblen, 1992). Thompson (1978) defined a polysome as *"a crystal that can be regarded as made of chemically distinct layer modules"* implying that a polysomatic series requires *"at least two components for its complete description"*. Moreover, all members of a polysomatic series are stoichiometrically collinear, this means that their chemical composition is a linear combination of the stoichiometries of the two building blocks. In CRFC the two components (building blocks) required for the description of the polysomatic series are bastnäsite (*B*-slab) and synchysite (*S*-slab). A schematic illustration is provided in Figure 1.1.

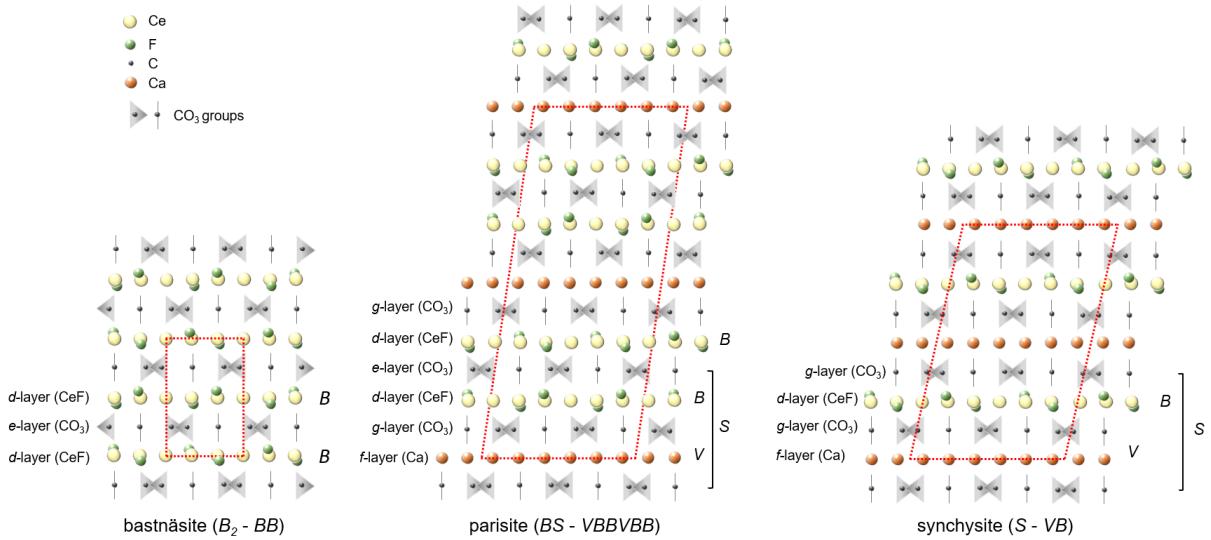

Figure 1.1. Drawings of the basic CRFC structures showing the different building blocks stacked along the c-axis (vertical). Different coding systems: *degf*, *BS* and *VB* are reported.

Table 1.1. List of the known B_mS_n phases with their chemical formula, ideal Ca/REE ratio, stack thickness and the relative *VB* and *BS* notation.

Name	Formula	Ideal Ca/(Ca+REE)	*VB* notation	*BS* notation	Theoretical Stack thickness (Å)	References
synchysite	$CaREE(CO_3)_2F$	0.500	*VB*	*S*	9.13	Donnay and Donnay, 1953; Van Landuyt and Amelinckx, 1975; Wang et al., 1994; Capitani, 2020; **this study**
	$Ca_4REE_5(CO_3)_9F_5$	0.444	V_4B_5	BS_4	41.4	Van Landuyt and Amelinckx, 1975
röntgenite	$Ca_2REE_3(CO_3)_5F_3$	0.400	*VBVBB*	BS_2	23.14	Donnay and Donnay, 1953; Van Landuyt and Amelinckx, 1975; Zeug et al., 2021
	$Ca_4REE_7(CO_3)_{11}F_7$	0.364	V_4B_7	B_3S_4	51.16	Van Landuyt and Amelinckx, 1975
parisite	$CaREE_2(CO_3)_3F_2$	0.333	*VBBVBB*	B_2S_2	14.01(x2)	Donnay and Donnay, 1953; Ni et al., 1993; Ni et al., 2000; Ciobanu et al., 2017; Capitani, 2019; Zeug et al., 2021; **this study**
	$Ca_4REE_9(CO_3)_{13}F_9$	0.308	V_4B_9	B_5S_4	60.92	Wu et al., 1994
	$Ca_3REE_7(CO_3)_{10}F_7$	0.300	V_6B_{14}	B_8S_6	93.82	Wu et al., 1998
	$Ca_2REE_5(CO_3)_7F_5$	0.286	V_2B_5	B_3S_2	32.9	Van Landuyt and Amelinckx, 1975; **this study**
	$Ca_3REE_8(CO_3)_{11}F_8$	0.273	V_6B_{16}	$B_{10}S_6$	103.58	Wu et al., 1998
	$Ca_4REE_{11}(CO_3)_{15}F_{11}$	0.266	V_4B_{11}	B_7S_4	70.68	Wu et al., 1998
	$Ca_5REE_{14}(CO_3)_{19}F_{14}$	0.263	$V_{10}B_{28}$	$B_{18}S_{10}$	179.14	Wu et al., 1994
	$CaREE_3(CO_3)_4F_3$	0.250	VB_3	B_2S	18.89	Meng et al., 2002; Ciobanu et al., 2017; Zeug et al., 2021; **this study**
	$Ca_2REE_7(CO_3)_9F_6$	0.222	V_2B_7	B_5S_2	42.66	Wu et al., 1994
	$Ca_8REE_{41}(CO_3)_{49}F_{41}$	0.163	V_8B_{41}	$B_{33}S_8$	234.08	**This study**
bastnäsite	$REECO_3F$	0	*BB*	B_2	4.88(x2)	Donnay and Donnay, 1953; Ni et al., 1993; Ciobanu et al., 2017; **this study**

The majority of the CRFC are short-range ordered polysomes. In principle, by stacking different end-members slabs, it is possible to generate an infinite number of combinations. It became, therefore necessary to determine whether an order sequence is significant or derives from a random combination. Van Landuyt and Amelinckx (1975), in their studies of CRFC and specifically on the B_2S polysome, defined that a polysome is considered to be significant when the ordered sequence is repeated at least ten times in three different crystal fragments. However, this definition is somewhat arbitrary. To address this, Veblen and Buseck (1979) defined a statistical criterion to define when an ordered sequence can be considered significant. If a structure is composed of A and B slabs, the probability of an ordered sequence of A and B slabs occurring by random stacking can be calculated using the following equation:

$$p = \frac{(n_A! n_B!)}{(n_A + n_B)!} \qquad (1.1)$$

where n_A and n_B represent the number of A and B slabs in the sequence. If the probability p is less than 0.001, the stacking sequence can be considered significant.

It has been observed that some stacking sequences occur more frequently than others, even in different polysomatic families. For example, in CRFC, the most common polysomes are synchysite (*VB*), parisite (*VBB*) and röntgenite (*VBVBB*) (see ahead for the explanation of the *VB* notation). The same sequences can be found in biopyriboles (Veblen and Buseck, 1979), where the building blocks are pyroxene (*P*) and micas (*M*) and the most common polysomes are amphibole (*MP*), jimthompsonite (*MMP*) and chesterite (*MPMMP*). Other examples include the humite group and the pyroxenoids. The humite group (Thompson, 1978) is formed by the combination of olivine (*O*) and norbergite (*N*) modules and the main polysomes are chondrodite (*NO*), humite (*NOO*) and clinohumite (*NOOO*). The same sequences are present in pyroxenoids (Koto et al., 1976; Narita et al., 1977; Thompson, 1978), where pyroxene is the building block *P*, and wollastonite is the building block *W*, whereas rhodonite, pyroxmangite and ferrosilite are composed by different stacking of *P* and *W* modules: *PW*, *PPW* and *PPPW*, respectively. The fact that some polysomes occur more frequently than others suggests that, under certain conditions, they are more stable than other sequences and random disordered sequences. Indeed, as pointed out by Veblen and Buseck (1979), the majority of short-range polysomes are metastable and the complexity of some structures suggest that they result from specific reactions or growth mechanisms, rather than being the lowest free energy arrangement.

Polytypism can be regarded as a restricted case of polysomatism (Baronnet, 1992). Polytypes have the same chemical composition, but slightly different structure (e.g. VBVBVB…, VBΛBVB…, where V and Λ are the same layer but with different orientation). In the case of CRFC, polytypism involves also different sequences of the same number and types of slabs along the stacking direction. For example, the most common parisite polytype is *VBBVBB*, but at least fourteen different polytypes have been described, such as the *VBVBBB* polytype describe by Capitani (2019). The existence of polytypism in CRFC arises due to the insertion of Ca-slabs into the bastnäsite structure, resulting in different orientation linkages between the two slabs. For this reason, in bastnäsite, which nominally does not contain Ca, polytypic disorder cannot be present. The crystal structure of parisite consists of two bastnäsite modules connected by a $CaCO_3$ (vaterite) module (Fig. 1.1). As described by Ni et al. (2000) and

Capitani (2019), to allow the stacking of the bastnäsite and vaterite building blocks, the anionic layers of the bastnäsite module above the Ca-layers are shifted by approximately 2.37 Å along the [-1-1 0] direction. The subsequent bastnäsite layer is shifted another 2.37 Å along the [-110] direction, which is oriented about 60° from the previous shift. Therefore, the stacking vectors between the anionic layers in consecutive bastnäsite segments are connected by ± 60° rotations. Thus, the existence of shift directions related by n x 60° (where n is odd) is what leads to the polytypism observed in parisite (Capitani, 2019). Additionally, the cumulative shifts on the (001) plane within the unit cell amounts to approximately 4.11 Å along the **a**-axis, leading to the monoclinic symmetry of parisite. The same principle is valid for synchysite (Capitani, 2020). As for polysomes, some polytypes are more common than others and the coexistence of different polysomes in the same crystals (polycrystals) and the possible reaction and/or transformation between polytypes are controversial and still under discussion [for a full review about the topic refer to Baronnet (1992) and references therein].

The observation of polysomatic and polytypic disorder in CRFC can be performed using both HRTEM images or selected area electron diffraction (SAED) patterns along orientations perpendicular to the **c***-axis, that is the stacking direction of the building blocks. There are mainly two suitable orientations: the [100], [130] and [1-30] (and their related Friedel's opposite) that can be grouped as <100> type; and the [110], [010] and [1-10] (and their related Friedel's opposite) that can be grouped as <110> type. These two orientation types alternate every 30° around **c*** (Capitani, 2020). However, the optimum orientation for the observation of polytypic disorder is the [110] direction, because in SEAD pattern, polytypic disorder can be easily recognized since it only affects the *11l* and *22l* rows, which appear streaked. Instead, polysomatic disorder also affects the *hhl* rows with $h = 3n$ (Fig. 1.2).

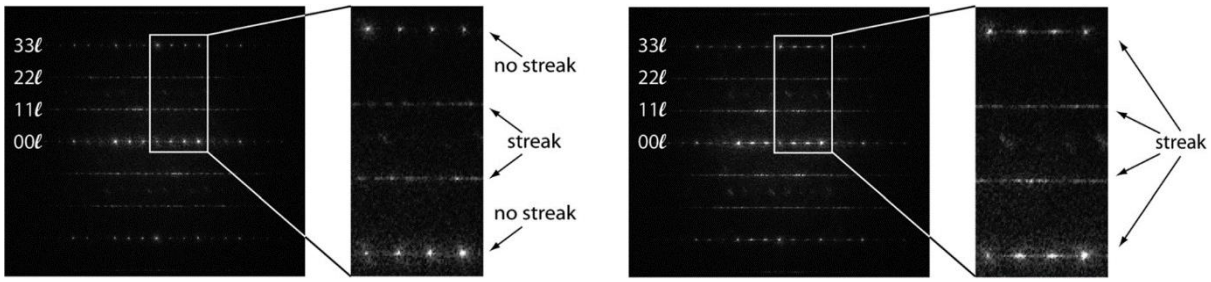

Figure 1.2. Fast Fourier Transform of parisite along [1-10] showing polytypic disorder (left) and both polytypic and polysomatic disorder (right). Polytypic disorder affects only the *11l* and *22l* rows, while polysomatic disorder affects also the *hhl* rows with $h = 3n$ (images taken from Capitani (2019)).

In recent years, atomic scale images performed by scanning transmission electron microscopy (STEM) with a high angle annular dark field (HAADF) detector have gained a lot of interest due to the extreme resolution that can be achieved. Ciobanu et al. (2017) applied this technique to the study of CRFC, aiming to observe the stacking disorder of these minerals. However, as stated by the authors themselves and by Capitani (2020), this technique performs well for the structures where heavy atoms are the essential components, but fails to visualize the lighter atoms. Thus, it is not suitable for visualizing polytypic disorder in CRFC, since the CO_3 atoms and their orientation are not visible. For this reason, the ultimate technique for fully characterizing order/disorder in CRFC is HRTEM.

Different nomenclatures have been created for the interpretation of TEM images. The first was introduced by Donnay and Donnay (1953), describing the bastnäsite-synchysite members in terms of *d*-layers (REE-F layers), *f*-layers (Ca layers), *e*-layers (CO_3 groups between REE-F layers) and *g*-layers (CO_3 groups between a REE-F layer and a Ca layer). A second notation by van Landuyt and Amelinckx (1975), the B_mS_n notation, describes the bastnäsite-synchysite series in terms of *B* (bastnäsite – *de*) and *S* (synchysite – *dgfg*) layers. Currently this is the most used notation because of its simplicity and conciseness. However, it is not able to distinguish between different stacking arrangements of the same polysomes, and as pointed out by Capitani (2019) the *B* and *S* modules cannot be easily separated in HR images. Later, an exhaustive notation was introduced by Yang et al. (1998). In this notation the four different orientation of the basic slabs (CaO_8 and CeO_6F_3) can be distinguished by different letters: u, n, ū, n̄ and b, d, p, q. Nevertheless, despite being exhaustive, this notation lacks of conciseness. A more recent notation, suitable for the interpretation of HR-images, describe the CRFC polysomes in terms of *V* and *B* layers, where *V* stands for $CaCO_3$ layers (vaterite like layers) and *B* for $CeCO_3F$ layers (bastnäsite layers). Indeed, in HRTEM images taken along [110], at the optimum defocus, the *V* and *B* layers can be easily recognized. *V*-layers appear as a grey band (Ca or *f*-layers) within two bright dotted lines (CO_3 or *g*-layers), while the *B*-layers appear as two dark bands (REEF or *d*-layers) separated by a bright dotted line (CO_3 or *e*-layers). In this last case *V* slabs cannot be adjacent because this would imply Ca-Ca bonding as in vaterite, which is not stable under geological conditions. Indeed, no polysomes richer in Ca than synchysite have been found and Ni et al. (2000) suggested that synchysite should be the Ca richest end members of the bastnäsite-synchysite series.

In HRTEM images polysomatic disorder is easily detectable, since the presence of stacking faults (*i.e.* insertion of extra slabs) disrupt the periodic structure of an ordered polysome (Fig 1.3A, B). This is also true for polytypic disorder. In CRFC, polytypic disorder can be categorized into two types: i) different arrangements of the same number and type of slabs, and ii) different orientations of the slabs within the same sequence (Fig. 1.3C). Both types are evident in HRTEM images. In the first case, the building blocks are positioned differently, as shown in Fig. 1.3C, where an ordered sequence of *VBBVBB* parisite includes a *VBVBBB* parisite sequence. In the second case, the disorder can be identified by examining the bright dotted lines representing CO_3 layers. The different stacking arrangements result in three possible geometries of the half-cell: a rectangular cell (0) and two oblique cells with different inclinations (+ and -).

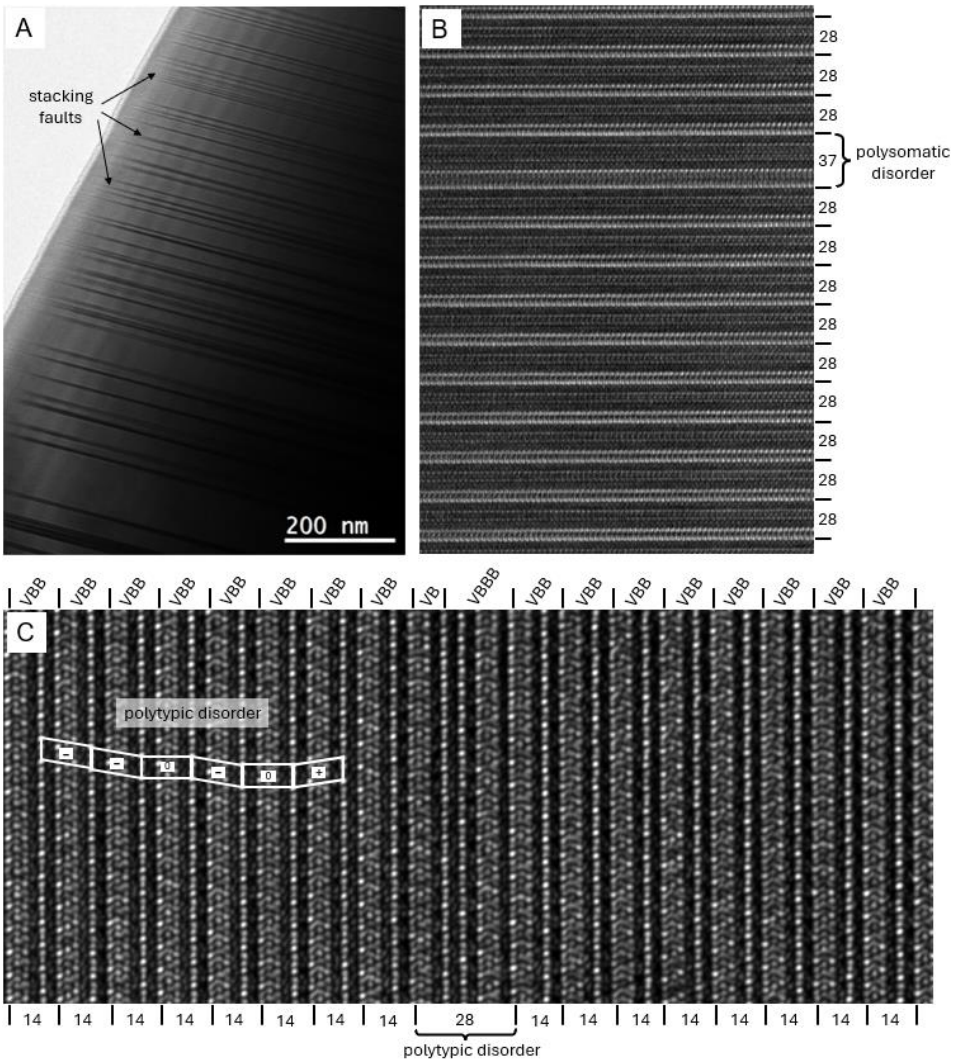

Figure 1.3. A) Bright field TEM image showing the presence of stacking faults (darker lines) within an ordered polysome. B) HRTEM image, showing an ordered parisite with a repeating distance of 28 Å with polysomatic fault caused by the insertion of an extra slab, leading to a lamella with a thickness of 37 Å. C) HRTEM image showing the two cases of polytypism in CRFC: i) order sequence of *VBBVBB* parisite with the presence of a single sequence of *VBVBBB* parisite polytype, and ii) different orientation of $CaCO_3$-$CeCO_3F$ slabs leading to three different geometries of the half-cell.

Chapter 2
Methodologies

2.1 Introduction

In this chapter all the methodologies and analytical techniques used in the study of CRFC in this work are explained in detail (Table 2.1). Samples description will be provided in the following chapters, as different samples with varying characteristics have been studied.

Part of this chapter has been published with modification and is under review as:

- *Conconi, R., Ventruti, G., Nieto, F., Capitani, G., 2023b. TEM-EDS microanalysis: Comparison among the standardless, Cliff & Lorimer and absorption correction quantification methods. Ultramicroscopy 254, 113845. https://doi.org/10.1016/j.ultramic.2023.113845*;
- *Conconi, R., Abad Ortega, M. M., Nieto, F., Buono, P., Capitani, G., 2024. TEM-EDS microanalysis: Comparison between different electron sources, accelerating voltages and detection systems. Ultramicroscopy* (under review)
- *Sanità, E., Conconi, R., Lorenzon, S., Di Rosa, M., Capitani, G., Mugnaioli, E., 2024. Application of an improved TEM-EDS protocol based on charge balance for accurate chemical analysis of sub-micrometric phyllosilicates in low-grade metamorphic rocks. Clays and Clay Minerals* 72, e31, *https://doi.org/10.1017/cmn.2024.32.*

2.2 Samples preparation

Before instrumental analysis with Raman spectroscopy and SEM the samples were embedded in epoxy resin and then polished using alumina with a nominal grain diameter of 0.3 μm as the last polishing step. The samples were carbon coated with a 20 nm C-film before SEM-EDS analysis. The C-film was not present during Raman analysis. The samples designated for EBSD investigations were further etch-polished with a SaphirVibro vibratory polishing device using 0.06 μm colloidal silica and then coated with 5 nm C-film.

Samples for TEM observations were prepared using three different techniques: ion milling, ultramicrotomy and focused ion beam (FIB) milling, depending on the dimensions and morphology of samples.

For ion milling, a 30 μm thick, double-polished section glued with cyanoacrylate adhesive to a glass slide was obtained. Copper rings, 3 mm in diameter, were stuck with epoxy resin on the selected sample areas, detached from the glass along with the attached minerals by acetone dissolution of the cyanoacrylate adhesive, and ion-milled down to electron transparency by a Gatan PIPS II Cool instrument at the Platform of Microscopy of the University of Milano-Bicocca (PmiB). During the milling process different configurations were used: initially, the ion guns were set at an incident angle of 10° with a voltage between 3 and 5 keV. As soon as a hole formed, the incidence angle of the guns was reduced to 5° and the voltage to 1.5 keV to clean the sample and remove the amorphous layer generated during the previous milling steps.

For the ultramicrotome preparation method, samples were first embedded in epoxy resin through a specific procedure. The samples were dipped in propylene oxide and infiltrated with varying proportions of propylene oxide and epoxy resin (2:1, 1:1, 1:2, and pure resin). The

samples were then transferred into moulds pre-filled with epoxy resin and placed in an oven at 60 °C to harden. Finally, the samples were sliced into approximately 70 nm thick slices using a Leica Ultracut E ultramicrotome at PmiB. The slices were then deposited on copper grids.

For focused ion beam preparation, lamellae were prepared using two different FIB-SEM instrument, both equipped with a Ga ion source: a ZEISS 550 Crossbeam at the Centre for Instruments Sharing of the University of Pisa (CISUP) and a TESCAN dual beam Gaia3 at the Institute for the Chemistry of OrganoMetallic Compounds (ICCOM) of the Italian National Research Council (CNR) at Sesto Fiorentino (Florence).

2.3 Raman spectroscopy

The Raman spectra were acquired at the Department of Earth Science "Ardito Desio" of the University of Milan with a LabRAM HR Evolution spectrometer, at room temperature. The instrument is equipped with an Olympus BX series optical microscope, a diffraction grating of 1800 grooves per millimetre, and a Si-based, Peltier-cooled Charge Coupled Device (CCD). Spectra were excited with the 633 nm emission of a He-Ne laser, and obtained using both a long focal length 50x, and 100x objectives and an acquisition time of 30 s per three accumulations. The fitting of Raman spectra was done after background correction assuming Lorentzian band shapes with the Fityc software. The system was calibrated using the 520.7 cm^{-1} line of a silicon wafer. When it was necessary to control the orientation of the incident and diffracted laser signal, a ½λ wave plate was used to polarize the light (see Chapter 3).

2.4 SEM-EDS-EBSD

SEM-EDS observations were carried out at the PmiB with a field emission gun (FEG) SEM Zeiss Gemini 500, operating at 15 keV and equipped with a Bruker Xflash EDS detector. The following conditions were applied during the analysis: a working distance of 8.18 mm, a 30 µm aperture, a beam current on the sample (measured by a Faraday cup) of approximately 300 pA, and an average counts per seconds varying between 3000 and 6000 cps. The standard method and φ(ρz) correction were used for quantitative analysis (Pouchou and Pichoir, 1991; Newbury et al., 2015, 2019). The following natural minerals, synthetic compounds and pure metals were used as standard: CeO_2 (Ce), LaF_3 (La, F), $NdSi_2$ (Nd), Sm (Sm), Y (Y), $PrSi_2$ (Pr), Gd (Gd), ThF_4 (Th), hematite (Fe), chlorite (Si, Al and Fe), and synchysite (Ca). EBSD investigations were conducted with a high-resolution Bruker e^-Flash detector mounted on the same FEG-SEM Zeiss Gemini 500. The following conditions were applied during the analysis: a sample inclination of 70°, a working distance of ~20 mm, an accelerating voltage of 20 kV and a 60 µm aperture.

2.5 SCXRD

SCXRD data were collected at the Department of Earth Sciences "Ardito Desio" of the University of Milan using a XtaLAB Synergy Rigaku instrument, equipped with a Mo microsource and hybrid photon counting X-ray detector. Data collection consisted in omega

scans, with steps of 0.5°, at variable phi and kappa angles, ensuring a reciprocal space coverage with average redundancy of a factor 5, based on monoclinic Laue symmetry. Data reduction was done with the Crysalis-red software developed by Rigaku.

2.6 TEM-EDS-3DED

Four different TEM instruments were used during the study of CRFC:

i) a JEOL JEM 2100P at the PmiB with conventional LaB_6 source, operated at 200 kV. The instrument is equipped with a Gatan Rio9 CMOS camera and an Oxford silicon drift detector (SDD) UltimMax EDS detector with an 80 mm^2 sensor. The Digital Micrograph software (Gatan) was used for image acquisition and processing. The HRTEM filter developed by Mitchell (2007) was employed to reduce the inelastic scattering in HR images. The EDS analyses were quantified with Aztec (Oxford) software using the standardless method, the Cliff-Lorimer approximation and the absorption correction method, detailed information about the mentioned methods and the operative conditions are given in paragraph 2.7.

ii) a FEI TITAN G2 operated at 300 kV and iii) a ThermoFisher Scientific TALOS F200X operated at 200 kV at the Centre for Scientific Instrumentation (CIC) of the University of Granada (Spain). Both instruments are equipped with a field emission gun (FEG) Schottky source and a ThermoFisher SDD Super-X EDS with a windowless design, providing a total detection area of 120 mm^2 (30 mm^2 per detector). The FEI TITAN G2 is also equipped with a HAADF detector for STEM observations and a C_s-corrector for ultra-high resolution images.

iv) a JEOL JEM-F200 operated at 200 kV at CISUP. The instrument is equipped with a Schottky FEG source, a windowless SDD EDS detector with an effective area of 100 mm^2, an ultra-fast and ultra-sensitive ASI CheeTah hybrid single-electron detector (512x512 pizel, 24 bit) with zero time read out and a NANOMEGAS topspin digital controller for beam precession. For the acquisition of 3DED data (Mugnaioli et al., 2018; Gemmi et al., 2019), FIB lamellae were mounted on a tomographic sample holder able to tilt up to ±65°. The sample was rotated within a maximum angle range of 120°, by constant steps of 1°. After each tilt step, a precession-assisted diffraction pattern was acquired with exposure time of 0.2 s. Nanobeam electron diffraction (NED) was performed in STEM mode, using the largest probe size (10) and the smallest C2 condenser aperture (10 μm). A parallel beam of about 30 nm was obtained relaxing the C3 lens by the Free Lens Control panel. Precession semi-angle was kept at 1°. Sample tracking was performed in HAADF STEM.

Table 2.1. All the analytical techniques and the operating conditions used for the characterization of samples, in each chapter, are here reported.

Instruments	Chapter 3	Chapter 4	Chapter 5
SEM-EDS	- Voltage: 20 kV - Working distance: 8.18 mm - Aperture: 30 μm - Beam current: ~600 pA - Quantification method: standardless-ZAF correction	- Voltage: 15 kV - Working distance: 8.18 mm - Aperture: 30 μm - Beam current: ~300 pA - Quantification method: standard- φ(ρz) correction	- Voltage: 15 kV - Working distance: 8.18 mm - Aperture: 30 μm - Beam current: ~300 pA - Quantification method: standard- φ(ρz) correction
EBSD	- Voltage: 20 kV - Working distance: ~20 mm		

	- Detector distance ~16.5 mm - Aperture: 60 µm - Sample tilting: 70°		
Raman spectroscopy	- Objective: 100x - Diffraction grating: 600 and 1800 grooves/mm - Acquisition : 3 x 30 s - Laser : He-Ne 633 nm - Bands shape: Lorentzian - ½λ wave plate	- Objective: 50x long focal length - Diffraction grating: 600 and 1800 grooves/mm - Acquisition : 3 x 30 s - Laser : He-Ne 633 nm - Bands shape: Lorentzian	- Objective: 50x long focal length - Diffraction grating: 600 and 1800 grooves/mm - Acquisition : 3 x 30 s - Laser : He-Ne 633 nm - Bands shape: Lorentzian
TEM-EDS	- Instrument: JEOL JEM 2100P – 200 kV and FEI TITAN G2 – 300 kV - Quantification method: Standardless corrected for absorption	- Instrument: JEOL JEM 2100P – 200 kV and FEI TITAN G2 – 300 kV - Quantification method: Standardless corrected for absorption and Cliff-Lorimer	- Instrument: JEOL JEM 2100P – 200 kV and JEOL JEM-F200 – 200 kV - Quantification method: Standardless corrected for absorption
3DED			- Instrument: JEOL JEM F200 – 200 kV - Sample rotation: 120° - Rotation steps: 1° - Precession semi angle: 1°
SCXRD			- Instrument : Rigaku XtaLAB Synergy - Microsource : Mo - Data collection: omega scan with 0.5° steps
Preparation for TEM	Ion milling	Ultramicrotome	Focussed ion beam

2.7 TEM-EDS microanalysis

The TEM is a well-established technique for the study of minerals from the microscale down to the atomic scale. Indeed, other than structural and microstructural information, chemical compositions at a comparable scale can be obtained (Wenk, 1976; Buseck, 1992; Nieto et al., 2013). The EDS is the most widespread analytical method installed in TEMs because it is easy to use, fast and of low acquisition cost. Every element can be reliably identified by EDS with the exception of a few pathological peak overlaps and light elements such as H, He, and Li. Following elemental identification, the amount of each constituent element can be determined and expressed as a mass or atom per cent.

In electron microprobe analysis of bulk samples, either with a EDS or a WDS (wave dispersive X-ray spectroscopy) system, the raw chemical analysis requires some corrections, generally referred to as ZAF correction (Heinrich and Yakowitz, 1975), where the acronym “ZAF” encapsulates a correction procedure for the effects of atomic number (Z), absorption (A), and secondary fluorescence (F) that are calculated separately by appropriate physical models. In TEM-EDS microanalysis, the A and F corrections are generally omitted because the sample is so thin (tens of nm or less), and therefore the interaction volume so small, that they are negligible. This is an assumption called the thin foil criterion (Williams and Carter, 1996).

However, as it will be demonstrated, this is not always the case, especially for thick and dense samples.

Whereas WDS microprobe analysis of bulk samples requires in-situ calibration with standards of known composition (Castaing, 1951), EDS analysis can also work without such calibration, making use of the standardless method, where the X-ray emission of the targeted element is calculated from first principles or remote standards (Newbury et al., 1995; 1998; 2013; 2019). In these cases, the raw analytical total must be normalised to unity to compensate for the lack of an electron dose correction, which is assumed by many users to be a source of comfort. The latter, along with the simplicity of operation with "one-button" analysis and the apparent close relation with the conventional standards procedure, are at the basis of the popularity of standardless analysis.

The standardless method can be used either for bulk samples in SEM or for thin foils and nanoparticles in TEM. Although in both cases it reveals very sensitive to the choice of the calculation parameters and the analyses can be affected by large errors. Whenever the investigated material has a simple and well constrained composition, as in most synthetic materials, or a qualitative analysis is just what is required, the standardless method may be preferred, i.e. the time spent for standardisation is not justified. However, minerals are commonly more complex than synthetic materials such as semiconductors or metallurgical samples, many elements may be present at the same time, the structure symmetry is lower on average (i.e., the X-ray emission and absorption within the specimen may be orientation dependent), and different minerals may have very different structures (i.e., the matrix effects may be significantly different from mineral to mineral). For all these reasons, in Earth Sciences, EDS analyses obtained through comparison with standards of known composition are preferred. In order to make valid the thin foil criterion, the analyst is usually forced to work in very thin areas of the sample, with the drawbacks of a low count rate and high electron dose per atom, causing quite high statistical errors and elemental diffusion (up to sample amorphization), respectively. To mitigate these problems and whenever one has to deal with thick and/or dense samples, TEM-EDS analyses can be obtained from relatively thick areas, providing a correction for absorption.

The necessity to obtain accurate TEM-EDS analysis for polysomes identification led to a comparison of the methods commonly used in TEM-EDS analysis quantification: the standardless method (Williams et al., 1991), the Cliff-Lorimer approximation (Cliff and Lorimer, 1975) and the absorption correction method based on electroneutrality (van Cappellen and Doukhan, 1994). This comparison aims to determine which method performs better and is more reliable with modern SDD detectors.

2.7.1 The Cliff-Lorimer approximation

The rationale for the quantification of X-ray analysis in analytical transmission electron microscopy (AEM) dates back to the monumental work of Castaing (1951), who described a procedure for the quantification of electron-activated X-ray emission from bulk samples that still forms the basis of the quantification routines of today electron microprobe (EMPA). According to Castaing (1951), the ratio of the concentration of an element (*i*) in the unknown

(C_i) and in a standard of known composition ($C_{(i)}$) is equal to the ratio of the related measured intensities ($I_i/I_{(i)}$) through a "sensitivity factor" K:

$$\frac{C_i}{C_{(i)}} = [K]\frac{I_i}{I_{(i)}} \tag{2.1}$$

The sensitivity factor K (k-factor) takes into account the difference between the generated and measured X-ray intensities for both the standard and the unknown, and is affected by the atomic number of the analysed element (Z), the absorption of the X-rays within the specimen (A) and the secondary fluorescence of X-ray within the specimen (F).

The fact that in AEM we deal with electron transparent thin foils instead of bulk specimens has some advantages. The correction procedure can be greatly simplified because, to a first approximation, the A and F corrections can be ignored and only the Z correction is necessary. Compared to a WDS system, the only one available at the time of Castaing (1951), where one element is measured at a time, the more recent EDS systems allow the acquisition of the whole spectrum.

Based on these advantages, Cliff and Lorimer (1975) developed a quantification method in which there was no need to incorporate intensity data from a standard, but simply ratio of the intensities gathered from two elements (A and B) simultaneously:

$$\frac{C_A}{C_B} = k_{A/B}\frac{I_A}{I_B} \tag{2.2}$$

In this case, the $k_{A/B}$ factor, often referred to as *Cliff-Lorimer factor*, is related to the atomic number correction factor (Z) only. To obtain the absolute value of C_A, a second equation is required, which for a binary compound is derived simply assuming that $A + B$ constitute the 100% of the specimen:

$$C_A + C_B = 100\% \tag{2.3}$$

For ternary or higher order systems:

$$C_A + C_B + C_C + \cdots = 100\% \tag{2.4}$$

Of course, k-factors for different elements pairs are related:

$$k_{A/B} = \frac{k_{A/C}}{k_{B/C}} \tag{2.5}$$

The concentration of the elements could be expressed in atomic % or weight%, or any appropriate units, as long as you are consistent.

2.7.2 The standardless method

TEM-EDS k-factors may be derived experimentally through standards of known composition, or calculated. The former requires well-characterised, electron-transparent and stable standards, it is slow and more laborious, but normally gives more reliable results. The latter is quick and represents the basis of the standardless quantification analysis.

The standardless analysis simplifies the measurement process by requiring the analyst to measure only the EDS spectrum of the unknown, whereas all the other operations (i.e. peak

integration, background subtraction, etc.) are executed as for conventional analyses with element standards. At least two different methods to standardless analysis are possible: first principles and remote standard method (Newbury, 1995; 1998; 2019). In the first case, pure theoretical calculation based on physical parameters are used. The electron-excited X-ray emission from the element *A* in the specimen is given by Williams and Goldstein (1991):

$$I_A = N\left(\frac{Q\omega a}{W}\right)_A C_A \Delta\rho t \int_0^t \varphi_A(\rho t) e^{-\chi\rho t}(1+\delta_A) d(\rho t) \tag{2.6}$$

where the terms before the integral represent the X-ray emission from the element *A* in an isolated thin film of thickness Δ and mass thickness ρt, *N* is the Avogadro number, *Q* the ionisation cross section, ω the fluorescence yield for the characteristic X-rays, *W* the atomic weight and C_A the weight fraction of the element A, *a* the relative transition probability of the same series of X-ray (the chances that a K_α or a K_β could be produced), the term $\varphi_A(\rho t)$ is the depth distribution of X-ray production and $e^{-\chi\rho t}$ accounts for the X-ray absorption in the specimen (where $\chi = \mu/\rho\, cosec\alpha$ is the mass-absorption coefficient for a X-ray take-off angle α), the term $(1 + \delta_A)$ accounts for the secondary fluorescence (the X-ray from *A* may also be fluoresced by other characteristic X-rays).

The Cliff-Lorimer approximation assumes that we can measure two characteristic X-ray intensities simultaneously and therefore we can take the ratio of two equations like equation 2.6. Moreover, in thin foils, the *F* and *A* corrections are negligible, i.e. the integral terms in equation 2.6 can be assumed equal to unity, obtaining:

$$\frac{I_A}{I_B} = \frac{C_A(Q\omega a)_A W_B}{C_B(Q\omega a)_B W_A} = \frac{C_A}{C_B}\frac{W_B}{W_A} \tag{2.7}$$

the above equation can be compared with equation (2.2) and rearranged:

$$k_{A/B} = \frac{(Q\omega a)_B W_A}{(Q\omega a)_A W_B} \tag{2.8}$$

from the above equation one realises that *k*-factors are mostly influenced by experimental factors such as: i) the accelerating voltage, since it affects the ionisation cross section (*Q*); ii) the Z number of the measured element, since it influences the fluorescence yield (ω) and the atomic weight (*W*) and iii) the relative transition probability (*a*) of the same series of X-ray.

Equation (2.8) needs to be further corrected for the detector efficiency ($\varepsilon_A/\varepsilon_B$), i.e. the absorption the X-rays generated by element *A* and *B* undergo passing through the detector components, that we know is higher for light elements (longer X-rays wavelengths) than for heavy elements (short X-ray wavelength). For all the detector component materials appropriate mass absorption coefficients are required.

On the other hand, the remote standard method for standardless analysis combines the measurement of pure elements or stoichiometric binary compound standards with physical models to create a database of intensities. These measurements must be carried out on a particular electron probe EDS system in which the measurement conditions such as the beam energy, the incidence angle, the electron dose, the take of angle and the EDS efficiency are very well known and the latter calibrated on a synchrotron beam line. The intensities so collected need to be corrected for the local EDS efficiency. Then, when the user requires a standard at a

different beam energy or that is not present in the library it is possible to obtain the missing value through a series of mathematical calculations (Newbury, 1995; 1998). The remote standard method is the most used method for standardless analysis since returns more accurate analysis than the first principle method (Newbury, 2013; 2019). Of course, for reliable calculated *k*-factors, accurate values for Q, ω, a and ε are required. Among these, the most challenging is Q, for which different opinions exist about the way to obtain the best values in the 100-400 kV range relevant for AEM (Powell et al., 1976; Williams et al., 1984). The combination of uncertainties in Q and in the detector parameters is the reason why calculated *k*-factors are usually not better than ±10-20% (Williams and Carter, 1996).

2.7.3 The Absorption correction

In dense and/or thick specimens, the thin foil criterion may not be valid. This means that the measured intensity for an element A is less than the generated intensity and the retrieved concentration C_A is no longer directly proportional to I_A. An absorption correction factor (A) is therefore required to account for the reduced measured intensity. Assuming that the depth distribution of X-ray production ($\varphi_A(\rho t)$) remains relatively unchanged and approximates unity even for thick samples, equation 2.6 and subsequent equations yield the following result (Williams and Carter, 1996):

$$A = \left[\frac{\left(\frac{\mu}{\rho}\right)_A}{\left(\frac{\mu}{\rho}\right)_B}\right]\left\{\frac{1-e^{-\left[\left(\frac{\mu}{\rho}\right)_B \rho t \, cosec\, \alpha\right]}}{1-e^{-\left[\left(\frac{\mu}{\rho}\right)_A \rho t \, cosec\, \alpha\right]}}\right\} \tag{2.9}$$

Therefore, in order to calculate correct *k*-factors, also the mass-absorption coefficients (μ) in the specimen for every measured element X-ray are required, as well as the sample density ρ and thickness t.

The major variable in the absorption correction is the path length $t' = t \, cosec \, \alpha$, where α is the take-off angle (Fig. 2.1). There are several methods to determine the sample thickness at the measuring point, summarised in Williams and Carter (1996), but none of them is of practical use when dealing with the quantification of a large number of analyses. Other methods have been developed that avoid the problem of measuring the thickness, known as extrapolation techniques (Horita et al., 1987; van Cappellen, 1990; Eibl, 1993), but with these methods one must know the beam current, which may be not as straightforward as it may sound.

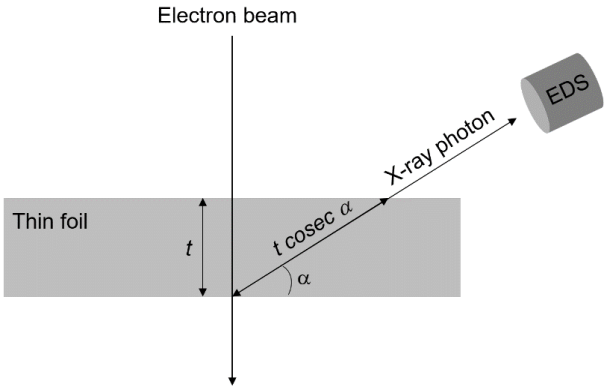

Figure 2.1. X-ray photon absorption path within the specimen as function of the thin foil thickness and detector take-off angle α.

It is worth to mention also the existence of the so called ζ-factor method, which present several advantages over the Cliff-Lorimer and other methods such as the possibility of the in-situ thickness determination from the built-in absorption correction if pure element thin film standards are used (Watanabe et al., 1996; Watanabe and Williams, 2006). However, despite the advantages, that are well described by Watanabe and Williams (2006), the main limitation of the ζ-factor method remains the necessity of the beam current measurement.

To overcome the problem of knowing the thickness and the beam current, an alternative method based on the *electron neutrality criterion* has been developed by Van Cappellen and Doukhan (1994) in which direct measurement of neither thickness nor beam current is required. Even the density of the sample and the take-off angle are not required, unless one needs to know the real thickness of the analysed area for some other reasons. This method has been adopted in this work and is briefly described below.

Classical software for X-ray microanalysis usually incorporate a routine based on equation 2.9, i.e. a quadratic approximation for the absorption correction. In this equation, μ_A and μ_B are concentration-dependent mass-absorption coefficients. In practice, concentrations are evaluated via successive iterations where μ_A and μ_B updates are used to calculate new correction factors until the whole procedure converges to what is believed to be the real composition of the target. As matter of fact, if one processes a specific spectrum with varying thicknesses and an approximate density ρ, the computed concentrations will align perfectly on a parabolic curve when plotted versus arbitrary thickness inputs (Fig. 2.2A). Therefore, with three chosen (fictive) thicknesses, it is possible to mathematically determine the parabola, i.e. predicting how the concentrations vary with thickness.

It should be realised that minerals, as well as ceramics and oxides, are ionic compounds, which means that the sum of all anions and that of the cations times their respective valence states should be equal. Of course, only one composition on the parabola will meet this condition, in principle only that at the actual thickness, which should be the correct one. Therefore, to determine the actual thickness, it is necessary to calculate the variation of the positive charge and that of the negative charge as a function of thickness and determine where the two curves, still parabolic but with opposite slope, intersect (Fig. 2.2B).

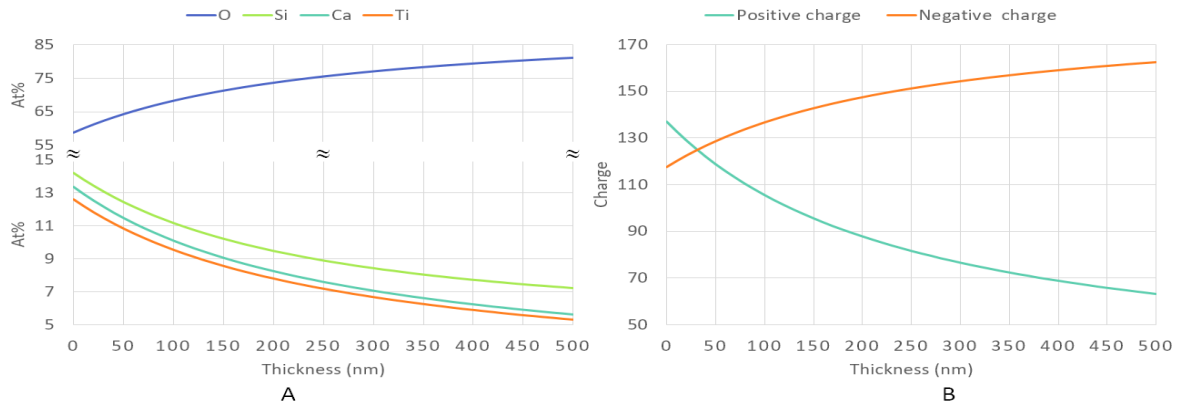

Figure 2.2. Quantification of a titanite ($CaTiSiO_5$) spectrum with the Aztec Oxford software as function of thickness for an assumed density ρ = 3.55 g/cm^3: (A) Atoms per cent and (B) positive and negative charges. The point where the two curves cross represents the actual foil thickness (30 nm).

However, if the employed density is not the actual density, the retrieved thickness is not the actual thickness, but the composition is still correct. It should be noted that quadratic functions generally employed in TEM-EDS software are based on first order approximations of the intensity attenuation factor and give a good evaluation of the specimen thickness in a range occurring well before the parabolic maxima or minima are reached. Consequently, data processing should not be attempted if the thickness greatly surpasses half the extremity values for the parabolas. In these cases, EDS software should be equipped with absorption correction equations incorporating higher-order terms.

2.7.4 Instrument and samples

The analyses were acquired with the JEOL JEM 2100P at the PmiB in STEM mode (scanning–transmission) under the following operating conditions: condenser lens diaphragm (150 μm); camera length (120 cm) and spot size (3 nm). The typical probe current density was in the order of 8.5 pA/cm^2 (estimated through the fluorescent screen) and the photon count rate in the order of 800-8000 cps (depending on sample composition and thickness). The analyses were acquired with an Oxford SSD UltimMax EDS detector with an 80 mm^2 sensor and a windowless design. The analyses were taken at 0-tilt orientation with the aim to warrant the same geometry for all standards and test samples, which in almost all cases corresponded to an orientation far from a zone axis, except from phyllosilicates, which were prepared by ion milling from cleavage flakes glued on Cu rings, implying an orientation at 0-tilt close to [001].

k-factors were derived for thirteen elements using fourteen different minerals and two synthetic compounds, all well characterised by EMPA (Table 2.2). EDS spectra were acquired using a selected area of 50*50 nm and an acquisition time of 50 s for all elements. In addition, for Na and K, in order to evaluate any elemental diffusion that commonly affects these elements, an acquisition time of 10 s was also used.

Table 2.2 Minerals and synthetic (*) compounds used as reference standards in the EDS calibration.

#	Mineral/Compound	Composition	TEM mount	Calibrated Element
1	Anorthite	$(Ca_{0.95}Na_{0.05})_{1.00}(Fe_{0.02}Al_{1.96})_{1.98}Si_{2.03}O_8$	grid	Al, Ca, O
2	Anorthoclase	$(Ca_{0.04}Na_{0.80}K_{0.13}Fe_{0.02})_{0.99}Al_{1.00}(Al_{0.05}Si_{2.95})O_8$	grid	Na, Al, O
3	Apatite	$Ca_{4.98}P_{2.97}Na_{0.04}Al_{0.01}Si_{0.03}O_{12}F$	grid	P
4	Augite	$(Ti_{0.02}Na_{0.09}Ca_{0.61}Al_{0.16}Fe^{3+}_{0.10})_{0.98}(Mg_{0.89}Fe^{2+}_{0.10})_{0.99}(Al_{0.17}Si_{1.83})_{2.00}O_6$	grid	Mg, Al, Ca, Fe, O
5	Biotite	$(Na_{0.04}K_{0.90})_{0.94}(Ti_{0.16}Mg_{1.26}Fe_{1.18}Al_{0.25})_{2.85}(Al_{1.21}Si_{2.79})_{4.00}O_{10}$	ion milled	Mg, Al, K, Fe, O
6	Scapolite	$K_{0.18}Na_{1.47}Ca_{2.13}Fe_{0.02}Al_{4.32}Si_{7.28}O_{24}$	grid	Na, Al, Ca
7	Spessartine	$(Mn_{2.48}Fe^{2+}_{0.38}Ca_{0.15}Mg_{0.04})_{3.05}(Ti_{0.02}Fe^{3+}_{0.21}Al_{1.71})_{1.94}Si_{3.01}O_{12}$	grid	Al, Mn, O
8	Hemimorphite	$Zn_4Si_2O_7(OH)_2H_2O$	grid	Zn, O
9	Microcline	$(K_{0.90}Na_{0.12})_{1.02}Al_{1.00}Si_{2.99}O_8$	grid	Al, K, O
10	Muscovite	$(Na_{0.11}K_{0.84})_{0.95}(Ti_{0.01}Mg_{0.02}Fe_{0.08}Al_{2.84})_{2.95}Si_{3.08}O_{10}$	ion milled	Al, K, O
11	Rhodonite	$(Fe_{0.21}Mg_{0.01}Ca_{0.09}Mn_{0.72})_{1.03}Si_{0.98}O_3$	grid	Mn, Fe, O
12	Titanite	$Ca_{1.04}Ti_{0.98}(Al_{0.07}Si_{0.95})_{1.02}O_5$	ion milled	Ca, Ti
13	Osumilite	$(Na_{0.13}K_{0.86})_{0.99}(Ca_{0.01}Ti_{0.02}Mg_{1.47}Fe_{0.90}Al_{2.67})_{5.07}(Si_{10.17}Al_{1.83})_{12.00}O_{30}$	grid	Mg, Al, K, Fe, O
14	Chromite	$(Mg_{0.74}Fe_{0.35})_{1.09}(Cr_{1.55}Al_{0.38})_{1.93}O_4$	grid	Cr
15	$CaSO_4$*	$CaSO_4$	grid	S
16	$MnSO_4$*	$MnSO_4$	grid	S

2.7.5 Experimental determination of *k*-factors

The experimental determination of *k*-factors requires, for all the elements of interest, TEM reference standards of known composition (i.e. Mellini and Menichini, 1985; Wood et al., 1984; Sheridan, 1989) that must fulfil some requirements. The sample must be stable under the electron beam, possibly a single phase, and capable of being thinned to electron transparency. The composition must be homogenous and well characterised and not subject to chemical changes during the milling process or the analysis. Then, equation 2.2 is used to retrieve the $k_{A/B}$ values from the measured intensities.

Two different sets of *k*-factors where experimentally derived: i) one set intended to be used with the Cliff-Lorimer approximation without absorption correction, derived from point analyses taken in thinnest parts of the specimen; and ii) a second set to be used with the absorption correction method and derived from point analyses taken at various foil thicknesses in the specimen and extrapolated to 0-thickness (Fig. 2.3). The latter implies that oxygen is analysed and a $k_{O/Si}$ determined. The first set of *k*-factors and the second set are reported in Table 2.3 and 2.4, respectively. Figure 2.4 represents the variation of *k*-factors as function of the analysed element, i.e. as function of the X-ray energy line used for the quantification.

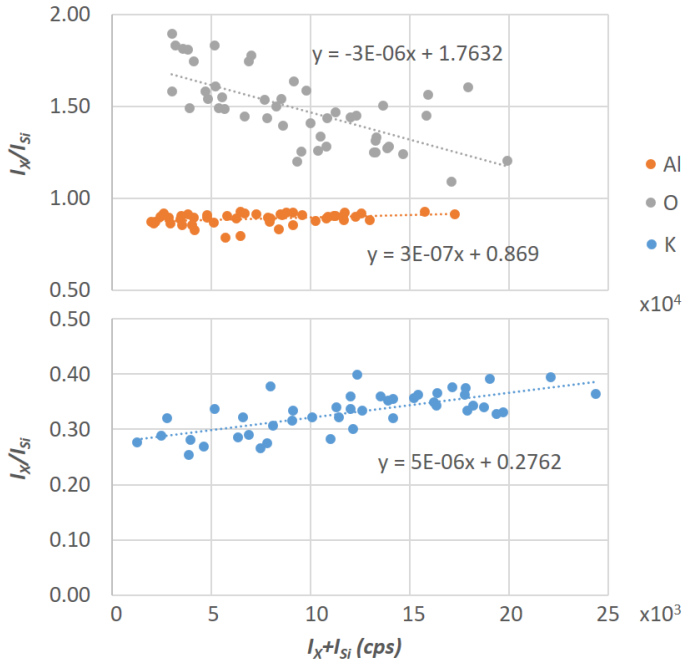

Figure 2.3. Example of extrapolation of (I_x/I_{Si}) intensity ratios in muscovite for the determination of k-factors for the elements Al, O and K.

The *k*-factors increase almost regularly on both sides of Si (reference element, $k = 1$), with few exceptions: Cr, which is higher than expected, and K, which shows high variability from mineral to mineral. The $k_{Cr/Si}$ has been determined indirectly through equation 2.10 from the $k_{Cr/Fe}$ of chromite (*chr*), where the $Cr_{K\alpha}$ radiation is strongly absorbed by Fe, and the $k_{Fe/Si}$ in silicates (*sil*), where the $Fe_{K\alpha}$ is not so strongly absorbed, because of the relatively lower average density of silicates:

$$k_{\frac{Cr}{Si}} = k_{\frac{Cr}{Fe}} \cdot k_{\frac{Fe}{Si}} = \left(\frac{C_{Cr}}{C_{Fe}}\frac{I_{Fe}}{I_{Cr}}\right)_{chr}\left(\frac{C_{Fe}}{C_{Si}}\frac{I_{Si}}{I_{Fe}}\right)_{sil} \quad (2.10)$$

Assuming that the concentrations in the standards are correct, the overestimation of the $k_{Cr/Si}$ factor may be due to the underestimation of I_{Cr} in chromite. This observation uncloses possible uncorrected matrix effects that may affect EDS analysis when dealing with very different mineral groups.

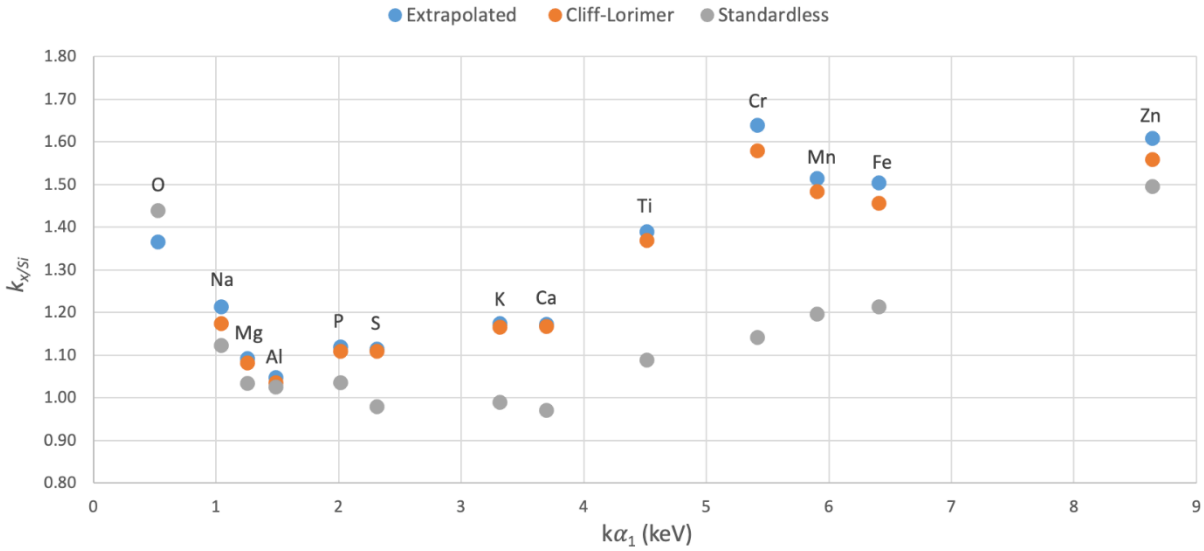

Figure 2.4. Plot of the $k_{X/Si}$ factors from spectra acquired in the thinnest part of the sample (Cliff-Lorimer) and from thicker samples extrapolated to 0 thickness, as function of Z.

Table 2.3. *k*-factors determined using the Cliff-Lorimer approach analysing only the thinnest parts of specimens (in brackets: average of the standard deviations obtained for each mineral-derived *k*-factor).

	Na	Mg	Al	P	S	K	Ca	Ti	Cr	Mn	Fe	Zn
Anorthite			1.03				1.18					
Anorthoclase	1.16		1.1									
Apatite				1.11								
Augite		1.09	0.99				1.14				1.52	
Biotite		1.06	1.02			1.05*					1.41	
Scapolite	1.19		1.01				1.17					
Spessartine			1.05							1.47		
Hemimorphite												1.56
Microcline			1.08			1.18						
Muscovite			1			1.16						
Rhodonite										1.5	1.44	
Osumilite		1.1	1.05			1.16					1.46	
Chromite									1.58			
$CaSO_4$					1.09							
$MnSO_4$					1.13							
Titanite							1.18	1.37				
Average	1.18 (0.05)	1.08 (0.04)	1.04 (0.04)	1.11 (0.04)	1.11 (0.03)	1.17 (0.04)	1.17 (0.04)	1.37 (0.04)	1.58 (0.04)	1.49 (0.04)	1.46 (0.05)	1.56 (0.06)

*Outliers not considered in the average.

Table 2.4. *k*-factors determined extrapolating to 0 thickness analyses taken also on thick areas of specimens.

	Na	Mg	Al	P	S	K	Ca	Ti	Cr	Mn	Fe	Zn	O
Anorthite			1.05				1.20						1.27
Anorthoclase	1.22		1.22*										1.24
Apatite				1.12									
Augite		1.08	0.99				1.15				1.54		1.42
Biotite		1.06	1.06			1.06*					1.54		1.17
Scapolite	1.21		1.02				1.13						
Spessartine			1.07							1.51			1.44
Hemimorphite												1.61	1.44
Microcline			1.12			1.20							1.38
Muscovite			1.02			1.38*							1.15
Rhodonite										1.52	1.46		1.52
Osumilite		1.14	1.05			1.15					1.48		1.43
Chromite									1.64				
$CaSO_4$					1.08								
$MnSO_4$					1.15								
Titanite							1.21	1.39					1.57
Average	1.22	1.09	1.05	1.12	1.12	1.18	1.17	1.39	1.64	1.52	1.51	1.61	1.37

*Outliers not considered in the average.

The high variability of the $k_{k/Si}$ values may be due to the high volatility of K, monovalent and with high ionic radius, under the high energy electron beam. This leads to an overestimation of the factor as it seems the case for muscovite (Table 2.4) but does not justify the low value determined for biotite (Table 2.3 and 2.4). Other reasons must be addressed for the latter. One of these may be related to the orientation-dependent probability of X-ray generation, sometimes indicated as *channelling effect*, which is pronounced when the analysing beam is parallel or close to a zone axis (Buseck, 1992).

The extrapolated 0-thickness values (Table 2.4) are consistent with the Cliff-Lorimer factors (Fig. 2.4), recording, in general, slightly higher values, as expected. Major deviations affect heavy elements, Mn, Fe and Zn, since the dense media in which these elements are included may show auto-absorption effects even in thin foils. For Na, which also shows a small deviation, absorption may be significant even in thin foils because of the low energy of the $Na_{K\alpha}$ radiation. Moreover, for this element, diffusion may be significant in thin foils more than in thick areas, because of the higher electron dose per atom.

Within the same element, the high $k_{Al/Si}$ determined for anorthoclase (1.22) stands out, higher than for all the other minerals (0.99-1.12). Due to the closeness in energy between the $Al_{K\alpha}$ and $Si_{K\alpha}$ (1.740 and 1.487 keV, respectively), a value closer to 1 would be expected. A possible explanation of this inconsistency calls into play chemical zonation in the standard, which is almost unavoidable in plagioclase, and that was actually detected, but evidently not side-stepped!

Finally, the $k_{O/Si}$ shows quite scattered values in comparison to those of other elements. This can be easily understood given the low energy of the $O_{K\alpha}$ radiation (0.525 keV), which is easily absorbed to varying degrees depending on the mineral structure's density. Due to this, two different data sets were derived for different situations: one based on denser phases (augite,

spessartine, osumilite, hemimorphite, rhodonite and titanite), with $k_{O/Si}$ factors ranging from 1.42 to 1.57, and one based on lighter phases (anorthite, anorthoclase, biotite, microcline and muscovite), with $k_{O/Si}$ values ranging from (1.15 and 1.38). For some unexplained reasons, osumilite (specific gravity 2.58-2.68) behaves as a denser phase. Moreover, since H is not detected by EDS (nor WDS) systems, it is common practice to recalculate mineral compositions based on a reduced number of negative charges: 22 for micas (as in muscovite, $KAl_2AlSi_3O_{10}(OH)_2$), 28 for chlorite (as in clinochlore, $(Mg,Fe^{+2})_5Al(Si_3Al)O_{10}(OH)_8$), 46 for amphibole (as in tremolite, $Ca_2Mg_5Si_8O_{22}(OH)_2$), and so on. Although this method does not alter the measured cations proportions, when used with the TEM-EDS absorption correction method it may lead to physically unrealistic negative values of thickness calculated through the electron neutrality criterion. To overcome this problem, it is good practice to reduce the valence of O to account for the contribution of H. For instance, the O valence in mica is reduced to –1.83 (reduced basis of negative charge/n. of oxygens = –22/12), in chlorite to –1.56 (–28/18), in amphibole to –1.92 (–46/24), and so on. Of course, after correcting for absorption, the mineral formula must be recalculated on an integral basis of negative charges (i.e. –24 for micas, –36 for chlorite, –48 for amphibole, and so on).

2.7.6 Applications to some reference samples

The average *k*-factors obtained as described above (last line in Table 2.3 and 2.4) were tested against minerals of known composition, viz. johannsenite, antigorite, biotite, cordierite, fayalite and spinel, in order to compare the standardless quantification method (SLM), the Cliff-Lorimer approximation (CLA) and the absorption correction method (ACM). In Table 2.5 we report TEM-EDS results for these reference samples along with their bulk chemical composition obtained with EMPA (before crushing or ion-milling). For the determination of the thickness with the ACM, densities of 3.52, 3.09, 2.60, 2.52, 4.39 and 3.87 g/cm^3 were assumed for johannsenite, biotite, cordierite, antigorite, fayalite and spinel, respectively.
As expected, the CLA and the ACM return more accurate results than SLM. For CLA and ACM, deviations from the reference samples are within 7-8% for major elements, with few exceptions, and commonly around 4-5%; they are several times higher for the STL method. The exceptions concern Al in antigorite, Fe in johannsenite and K in biotite. The Al content in antigorite, however, is generally low and the deviation may arise from a poor counting statistics affecting both, EMPA and TEM-EDS. Moreover, the crystal analysed with TEM-EDS comes from the same suite of crystals analysed by EMPA, but it was not directly analysed by EMPA, i.e. a deviation in composition is not surprising, especially if one considers that the Mg/Si ratio may be affected by polysomatic disorder. Johannsenite is markedly zoned, the zoning concerns relative abundances of Mn, Fe and Mg in the M1 site (Capitani and Mellini, 2000a, b). Since a large deviation affects also Mg and, to a lesser extent Mn, and considering that, as for antigorite, the crystal analysed by EMPA is not the same analysed by TEM-EDS, the observed TEM-EDS composition may be real. The large deviation affecting the K content in biotite, where it is underestimated, may be due to diffusion under the highly focused electron beam. In principle, if the analysis of the unknown is performed on the same matrix used for the standardization and under the same experimental conditions, diffusion should affect in the same manner both standard and unknown, cancelling each other. In this case, the same experimental conditions

were applied, but the $k_{K/Si}$ was derived from data from feldspar and osumilite, because of the odd data obtained from phyllosilicates, probably affected by channelling (see above). Therefore, the analysis of interlayer cations in phyllosilicates may pose serious quantification problems because of concurring effects such as diffusion and channelling.

The number of atoms per formula unit (a.p.f.u) for fayalite (heavy mineral) and cordierite (light mineral) is constant in the case of ACM despite different thicknesses of the analysed volume (Fig. 2.5), as it should be. On the contrary, CLA results show different trends for heavy and light minerals. In fayalite, the a.p.f.u. of Fe and Si diverge with increasing thickness, showing a positive slope for Fe and a negative slope for Si, meaning that Fe is overestimated and Si underestimated with increasing thickness because the $Fe_{K\alpha}$ is less absorbed than the $Si_{K\alpha}$. The divergence is observable for sample thicknesses as low as 50 nm. This behaviour is only slightly noticed in cordierite for Mg and Fe, i.e. the most contrasting element in terms of emission photon energy in the mineral, and only for thicknesses higher than 80-100 nm, whereas Al and Si, with close emission photon energy, evolve in parallel. These observations suggest that absorption correction is effective only for heavy minerals and/or at high sample thicknesses. In cordierite, however, a different phenomenon was observed, which is reflected by the trembling trend of a.p.f.u. as function of thickness and which is due to chemical zoning. A possible exchange vector of the type $Si^{4+}+(Mg,Fe)^{2+}=2Al^{3+}$ is suggested based on the perfect anti-correlation relationship involving these elements (Fig. 2.6).

Table 2.5. TEM-EDS analyses (a.p.f.u) quantified with SLM, CLA and ACM for reference samples johannsenite, antigorite, biotite, cordierite, fayalite and spinel and the deviation in % from the reference value (averaged number of analysis in brackets).

	Johannsenite (12)	14-104 nm						Antigorite (18)	32-196 nm					
	Reference*	STL		CLA		ACM		Reference§	STL		CLA		ACM	
Mg	0.04	0.01	75%	0.01	75%	0.01	75%	2.63	1.72	35%	2.49	5%	2.53	4%
Al	0.02	b.d.l.	-	b.d.l.	-	b.d.l.	-	0.07	0.08	14%	0.12	71%	0.12	71%
Si	1.98	1.86	6%	1.97	1%	1.99	1%	1.97	1.49	24%	2.08	6%	2.06	5%
Ca	1.00	0.80	20%	1.02	2%	1.00	0%	0.01	b.d.l.	-	b.d.l.	-	b.d.l.	-
Mn	0.87	0.62	29%	0.81	7%	0.81	7%	-	-	-	-	-	-	-
Fe	0.10	0.17	70%	0.22	120%	0.22	120%	0.10	0.07	30%	0.12	20%	0.11	10%
	Biotite (18)	8-285 nm						Cordierite (18)	48-164 nm					
	Reference#	STL		CLA		ACM		Reference&	STL		CLA		ACM	
Na	0.05	0.07	40%	0.09	80%	0.06	20%	0.07	0.01	86%	0.01	86%	0.01	86%
Mg	1.25	0.98	22%	1.22	2%	1.30	4%	1.52	1.32	13%	1.56	3%	1.60	5%
Al	1.30	1.03	21%	1.23	5%	1.30	0%	3.91	3.55	9%	4.09	5%	4.11	5%
Si	2.84	2.35	17%	2.82	1%	2.74	4%	4.99	4.27	14%	4.85	3%	4.84	3%
K	0.87	0.50	43%	0.68	22%	0.76	13%	-	-	-	-	-	-	-
Ca	0.01	b.d.l.	-	b.d.l.	-	b.d.l.	-	-	-	-	-	-	-	-
Ti	0.22	0.17	23%	0.25	14%	0.24	9%	-	-	-	-	-	-	-
Mn	0.03	0.02	33%	0.03	0%	0.04	33%	0.01	0.00	-	0.00	-	0.00	-
Fe	1.36	0.96	29%	1.36	0%	1.38	1%	0.59	0.42	29%	0.57	3%	0.56	5%
	Fayalite (17)	61-214 nm						Spinel (20)	34-380 nm					
	Reference§	STL		CLA		ACM		Reference§	STL		CLA		ACM	
Mg	0.03	0.03	0%	0.03	0%	0.03	0%	0.71	0.57	20%	0.64	10%	0.67	6%
Al	-	-	-	-	-	-	-	1.95	1.77	9%	1.94	1%	1.95	0%

Si	0.99	0.98	1%	0.94	5%	0.95	4%	-	-	-	-	-	-	-
Mn	0.09	0.09	0%	0.10	11%	0.10	11%	0.01	0.01	0%	0.01	0%	0.01	0%
Fe	1.90	1.70	11%	1.97	4%	1.93	2%	0.36	0.34	6%	0.44	22%	0.39	8%
Zn	-	-	-	-	-	-	-	0.01	0.01	0%	0.01	0%	0.01	0%

*Capitani et al., 2000c; [$]Capitani and Mellini, 2006; [#]Fregola et al., 2009; [&]Capitani et al., 2002; [§]from the mineralogical collection of the Department of Earth and Environmental Sciences (DISAT) of the University of Milano-Bicocca.

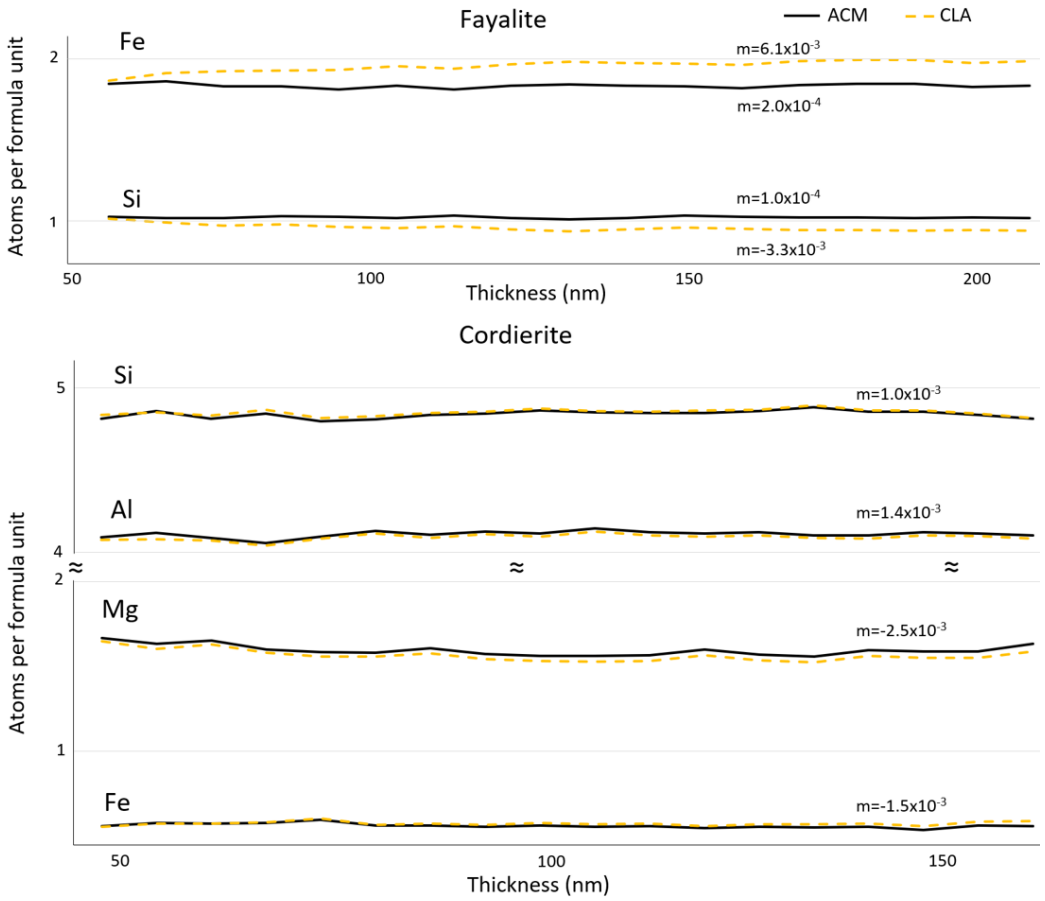

Figure 2.5. Comparison of the a.p.f.u. determined with ACM and CLA as function of the thickness of the analysed volume for fayalite and cordierite. In the plots, m represents the slope of the fitted linear trends; for cordierite only one value is given since the ACM and CLA trends almost overlap.

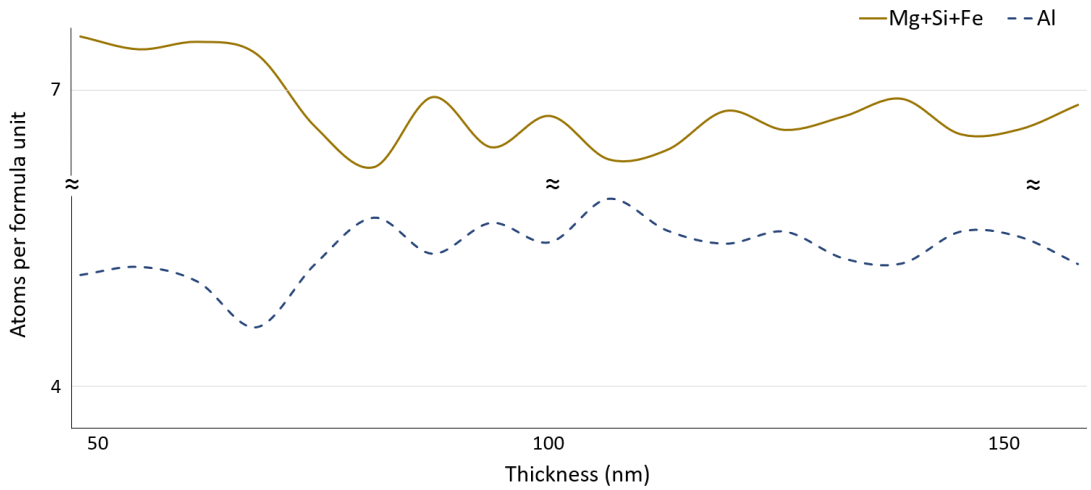

Figure 2.6. a.p.f.u. of Al and Mg+Si+Fe measured in cordierite with the ACM as function of the thickness of the analysed volume, showing perfect anti-correlation.

2.7.7 Comparison between different electron sources, accelerating voltages and detection systems

The performance of the CLA and ACM methods were compared across three TEM instruments, which differ in source type (field emission vs. thermionic), accelerating voltage (200 vs. 300 kV) and EDS system type (4 in-column SDD vs. single SDD), with all other variables held constant (standards, samples, operating conditions, etc.). The instruments compared were the JEOL JEM 2100P, the FEI TITAN G2 and the ThermoFisher Scientific TALOS F200X (for specific details refer to section 2.6, Table 2.1)

Overall, the trend of the *k*-factors (Fig. 2.7) is similar across the three microscopes, showing an almost regular increase on both sides of Si. Specifically, *k*-factors derived using the CLA present similar values in all microscopes, with only a few exceptions such as higher values for P and S in the TITAN, and a lower value for Na in the TALOS. Conversely, the ACM *k*-factors show differences between different microscopes. The values of the JEOL and TITAN ACM-factors are comparable, whereas in the TALOS, elements on the right side of Si have higher values and those on the left side have lower values.

Another feature of the *k*-factor vs. Z plot is that the differences between the CLA- and ACM-factors are wider in the TALOS than in the TITAN and JEOL. At first sight, this observation indicates major absorption-related problems in the TALOS, especially for high energy X-ray photons (higher than the $Si_{K\alpha}$), than for the other TEMs and may depend, at least in part, on the same reason as above. However, if a lower sensitivity for high energy photons were the only reason, one should expect systematically higher values of both factor types rather than a large difference between them. A possible explanation of the observed difference may rely on the electron beam interaction volume, higher at 200 kV because of the larger cross section than at 300 kV (Fig. 2.8). The larger interaction volume, in turn, determines a larger volume involved in the absorption of X-rays within the sample, hence larger ACM-factors. In the JEOL, although the interaction volume is, in principle, the same as in the TALOS, the single SDD

detector determines a smaller sample volume involved in the absorption of the X-rays, hence smaller ACM factors.

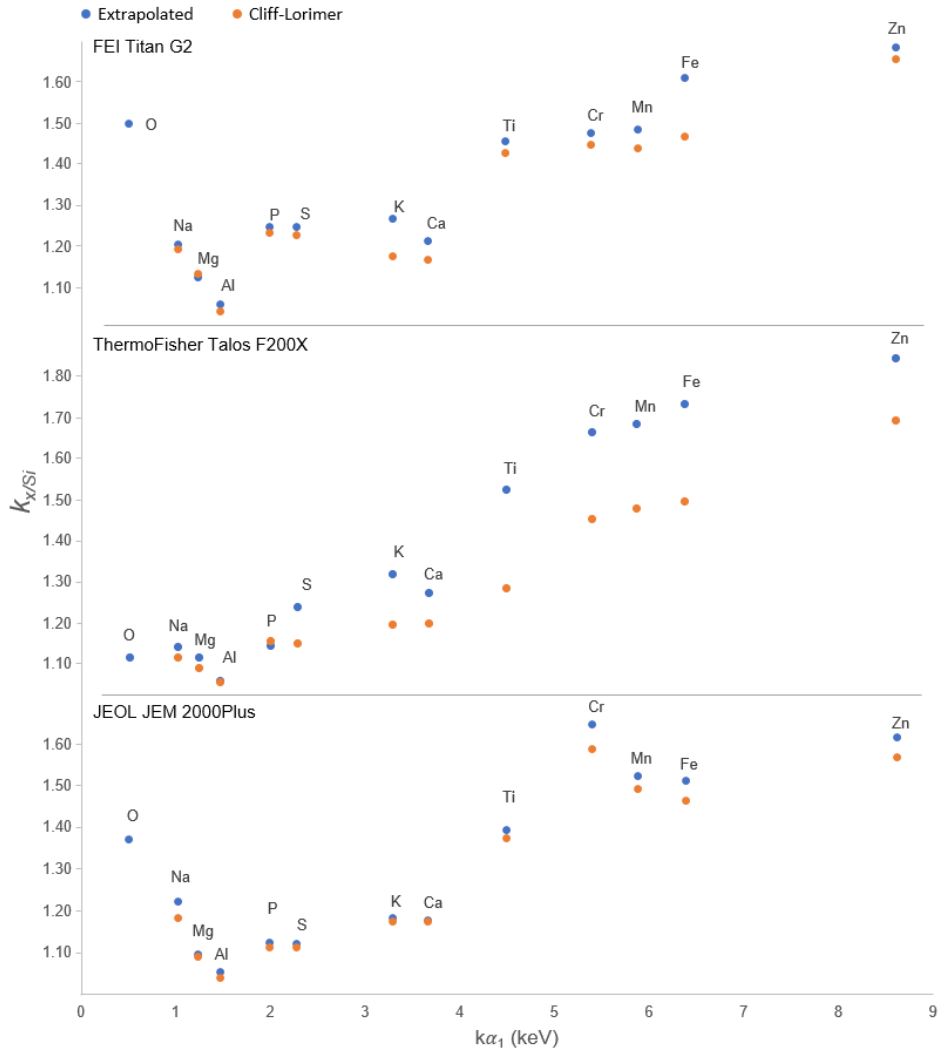

Figure 2.7. Plot of the extrapolated at 0-thickness (blue dots) and Cliff-Lorimer (orange dots) $k_{X/Si}$ factors for the TITAN, TALOS and JEOL instruments.

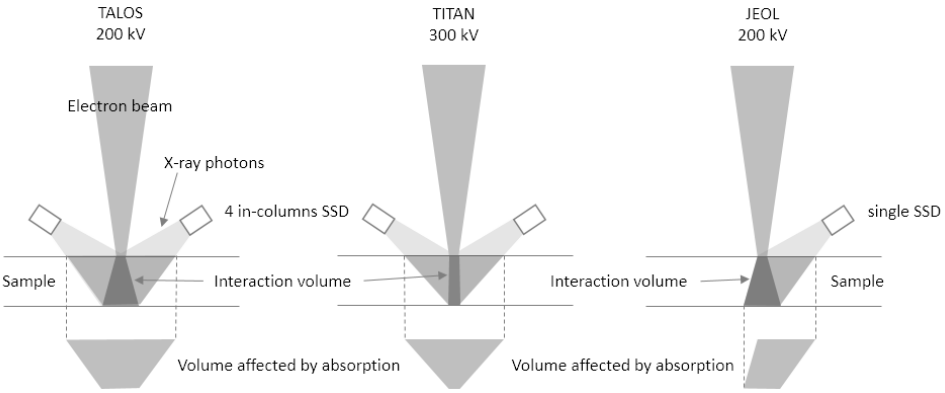

Figure 2.8. Schematic representation of the interaction volume and of the volume of sample involved in the absorption of X-rays for the three different systems tested in the study.

When comparing the results obtained on the reference materials (Figs 2.9 and 2.10) (refer to section 2.7.6 for the composition of the reference materials), generally, the ACM returns slightly better results than the CLA. Overall, the results show that deviations from the reference samples are below 10% (and generally much smaller) for major elements. Instead, for minor elements the deviations from the reference samples are higher (i.e. Mn in johannsenite, K in biotite and Fe in spinel). Nevertheless, except for Mn in johannsenite, the deviations of minor elements are lower than 22%. For instance, in the case of Fe in spinel, 0.36 a.p.f.u. of Fe with a deviation of 22% amounts to 0.08 a.p.f.u., which is still reasonable. As discussed, these larger deviations are due to intrinsic problems of the reference samples, namely chemical zoning in johannsenite, diffusion of K atoms and channelling effects in biotite. The detection limits of the three systems were evaluated by examining minor elements (< 1 wt%) in the reference samples. As expected, the detection limit is lower in the 4 in-column SDD systems than in the classical single SDD system. Minor elements are consistently detected with the 4 in-column SDD systems, whereas this is not always the case for the single SSD detector (e.g., Al in johannsenite, Ca in biotite and Mn in cordierite). Figure 2.11 illustrates the error trends in the three instruments for three different elements: Fe, Mn and Mg, which exhibit different concentrations (analysis refers to Fayalite). Indeed, in Fayalite Fe is a major element with concentration around 50 wt%, Mn is a major element with concentration around 2.7 wt% and Mg is minor element with concentration around 0.4 wt%. Overall, the errors associated with the analysis show a steady trend for the TITAN and TALOS, while the latter decreases when increasing the thickness, in the JEOL instrument. This trend may be related to the photon count rate, much higher in the TALOS and TITAN (3-4 times higher) than in the JEOL, due to a higher sensitive area (4 x 30 mm^2) and proximity to the sample of the 4 in-column SDD systems, than for the single SDD system of the JEOL (80 mm^2). Consequently, in the TALOS and TITAN the peak/background ratio is already satisfactory for thin areas and does not improve significantly for increasing thickness, leading to almost horizontal sigma vs. thickness trends. On the contrary, in the JEOL, the peak/background ratio increases significantly with increasing sample thickness, leading to a negative slope of the sigma vs. thickness trend. Surprisingly, the errors affecting abundant elements (Fe, in this case) are lower for the JEOL than for the other microscopes, become in-between for less abundant major elements (Mn) and, finally, agree with the expectations (are higher) for minor elements (Mg). This behaviour cannot be explained in a simple way, but assuming a better quantification routine – background subtraction and peak area integration – for major elements for the JEOL than for the other microscopes and vice versa. Finally, the TALOS performs better than the TITAN at any element concentration. This may be due to differences in the manufacturing of the two 4 in-column SDD systems or to usage-related issues.

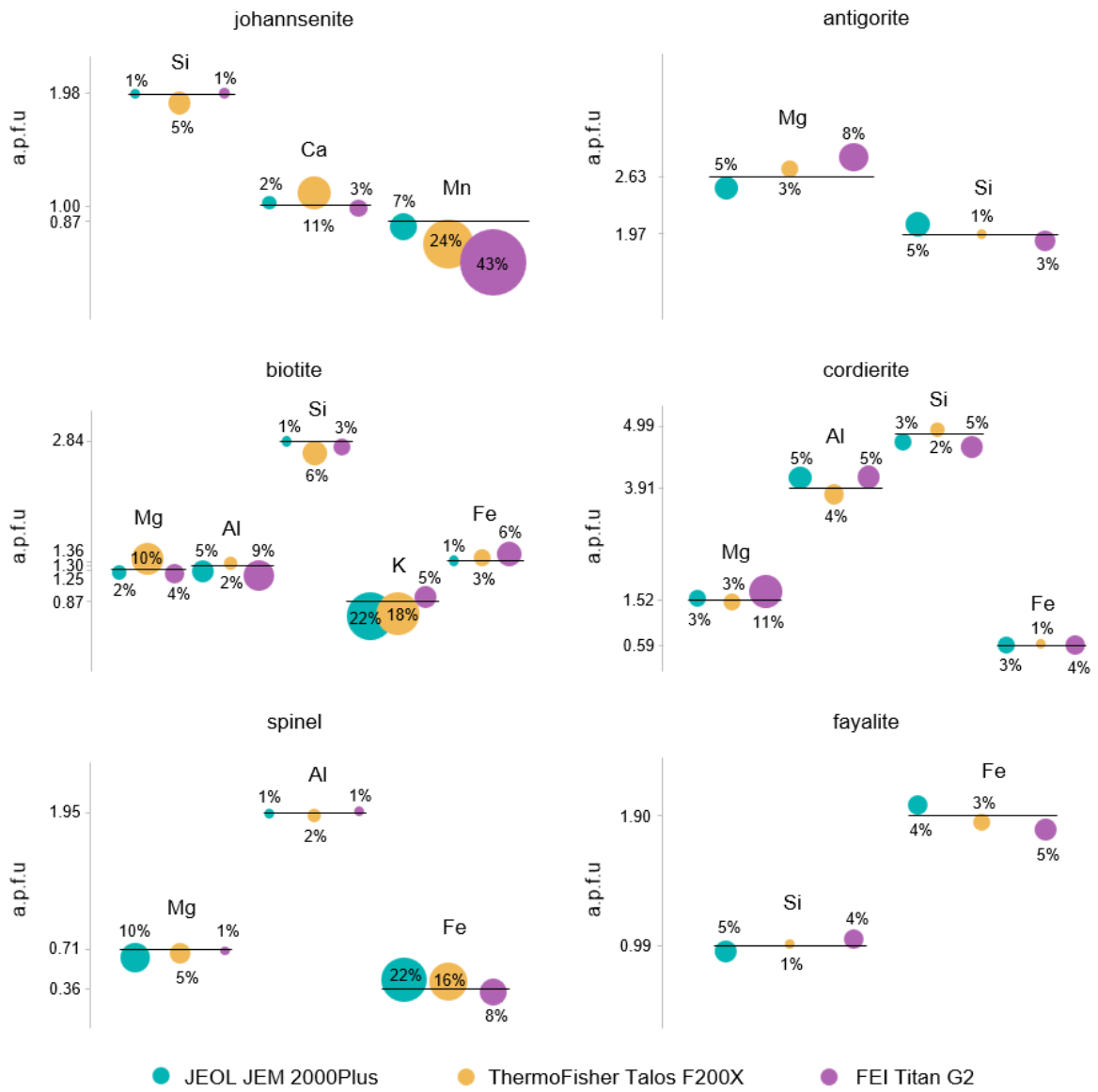

Figure 2.9. Deviations (%) of the analyses obtained with the ACM from the compositions of several reference minerals, the horizontal lines represent the concentration of the elements in the reference material.

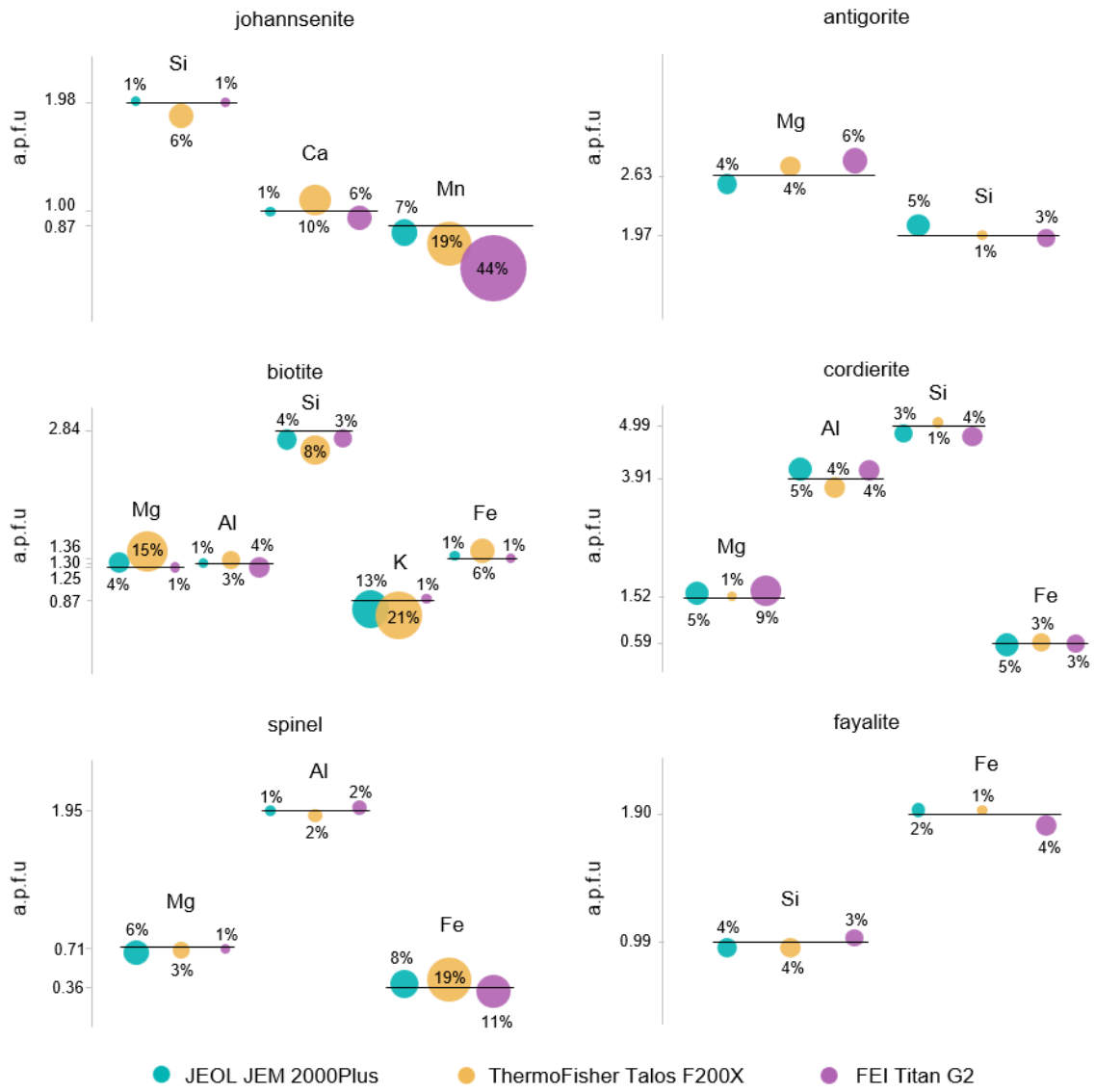

Figure 2.10. Deviations (%) of the analyses obtained with the CLA from the compositions of several reference minerals, the horizontal lines represent the concentration of the elements in the reference material.

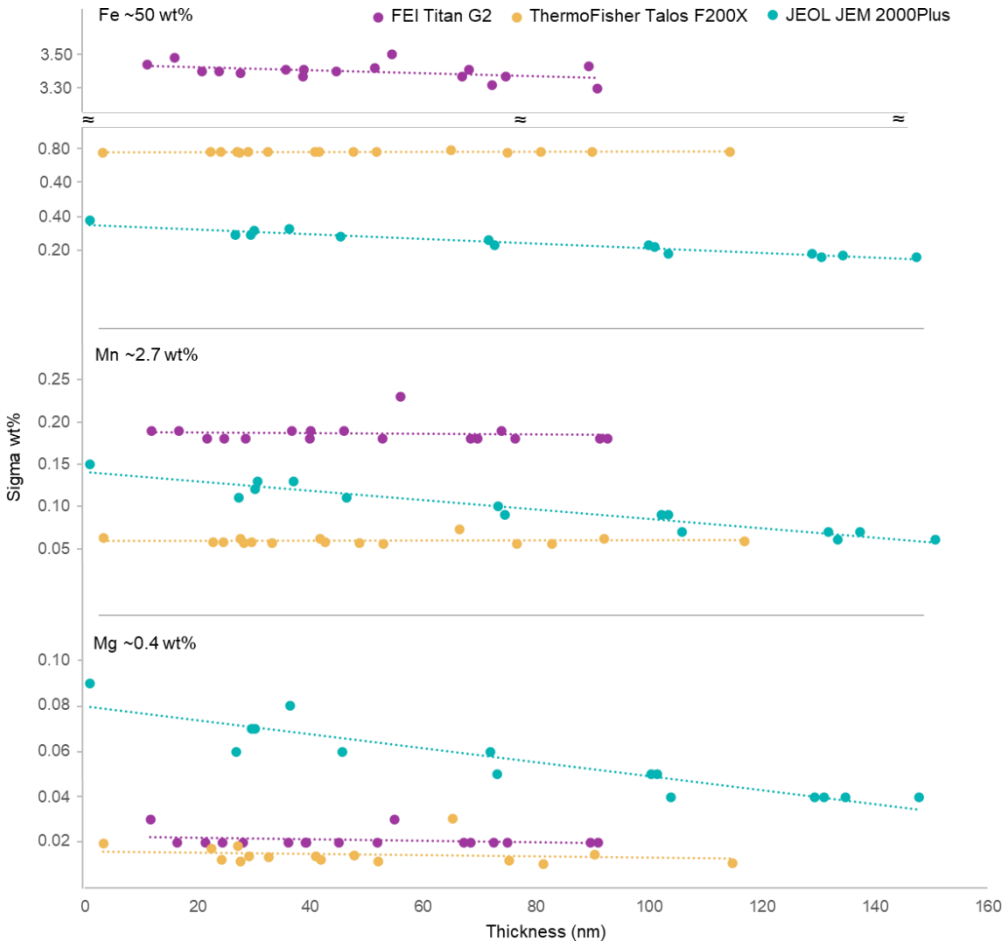

Figure 2.11. Error trends in the TITAN, TALOS and JEOL instruments.

2.7.8 Conclusions

i) The CLA and ACM give superior results compared to the SLM and, as far as the absorption correction can be considered negligible, very similar. However, starting from a mass-thickness of the order of 22 x 10^{-6} g/cm^2 (estimated on fayalite) absorption becomes significant and the ACM gives better results.

ii) The determination of the $k_{O/Si}$ factor is challenging because the low-energy $O_{k\alpha}$ radiation is severely absorbed and to a different extent in different minerals, leading to scattered data. This problem forced us to determine two different $k_{O/Si}$ to be used in different contexts: one for lighter minerals and one for heavier minerals ($\rho > 2.90$ g/cm^3).

iii) Caution must be used when *k*-factors are derived indirectly from minerals with very different structure/chemistry, as has been the case for the $k_{Cr/Si}$, determined indirectly from the $k_{Cr/Fe}$ of chromite and the $k_{Fe/Si}$ from silicates. The retrieved $k_{Cr/Si}$ deviates considerably from the trend depicted by all the other factors, probably because of the strong absorption of the $Cr_{K\alpha}$ by the dense spinel matrix. This observation lets one suppose that for accurate EDS quantification, separate *k*-factors data sets are required, at least for the major and diverse broad classes, such as silicates and metal-oxides.

iv) Some monovalent elements with large ionic radius, such as Na and K, may diffuse under the highly focused electron beam of the TEM, leading to a decrease with time of the related count rate. For these elements, shorter acquisition times (Nieto et al., 1996) and larger spot analyses, both during standardization and measurement, are required in order to get more reliable data. Finally, for very anisotropic mineral groups, such as phyllosilicates, channelling effects must be taken into account, for instance controlling the orientation of the mineral and reproducing the same conditions during standardization and measurement.

v) EDS calibration appears is "strictly instrument specific". Even among TEMs equipped with identical EDS systems, specific calibration is necessary. Numerous published k-factors are available for different accelerating voltages, reference elements and X-ray lines, see Williams and Carter (1996) and references therein. This study demonstrates, if any doubt remained, that universally valid k-factors cannot exist.

vi) The 4-in column SDD systems are more efficient in data collection, enabling more precise k-factors and lower detection limits. However, the comparison between the performance of classic single SDD system (Oxford/JEOL) and modern 4 in-column SDD systems (Thermofisher/TALOS and TITAN) does not unequivocally favour the latter in terms of final accuracy. This suggests that other error sources may influence the outcome, such as the quality of the standards and the complexity and diversity of natural minerals in terms of chemistry, density, matrix effects, etc.

Chapter 3

A multi-methodological identification of (Ca-REE) fluorcarbonates

3.1 Introduction

As already mentioned, in nature, CRFC rarely occur as single crystals. They commonly form microscale syntactic (crystallographically oriented) intergrowths (Donnay and Donnay, 1953) of different polysomes/polytypes, often with stacking faults at the nanoscale. Due to this recurrent microstructures, definitive structural analyses by SCXRD have been achieved relatively recently and only for some basic polysomes, namely bastnäsite-(Ce) (Ni et al., 1993), synchysite-(Ce) (Wang et al., 1994), and parisite-(Ce) (Ni et al., 2000). Apart from these fortunate cases, for most occurrences with intergrowths at the microscale, reliable structural analysis can only be performed via TEM.

Regarding SEM-EDS analysis, a relatively faster characterization technique compared to HRTEM, syntactic intergrowths can be revealed by average atomic number (Z) contrast in BSE images. However, no orientation relationships can be obtained and submicroscopic intergrowths may be hidden and merged into a uniform-grey-tone band. Similarly, microprobe analysis, whose spatial resolution is on the order of a few micrometres, may only provide an average composition when submicroscopic lamellae are present within the analysed volume. In extreme cases this could mimic the composition of a potential polysome. Another relatively fast characterization technique, Raman spectroscopy, has been poorly exploited in these minerals so far. Ce-dominant CRFC have been investigated by Frost and Dickfos (2007), Guastoni et al. (2009) and more recently by Zeug et al. (2021), sometimes providing contrasting results. Raman spectroscopy has a spatial resolution comparable to microprobe analysis, and according to Zeug et al. (2021) it can distinguish among some basic polysomes, but what is the influence of submicroscopic lamellae on the Raman response is not clear. On the other hand, EBSD has, in principle, a much better spatial resolution (tens of nm) than the techniques mentioned above, and may provide orientation relationship information. However, its capability to distinguish among different CRFC has never been tested.

In this chapter, well characterized CRFC from Mount Malosa (Malawi) (Guastoni et al., 2009, 2010; Capitani, 2019) were studied using a combination of SEM-EDS, TEM-EDS, Raman spectroscopy and EBSD, the latter applied for the first time to CRFC. This approach aimed to evaluate the potential of Raman spectroscopy and EBSD in the microscopic characterization of the material and to provide a "road map" for further, focused investigation, such as the determination of new polysomes with TEM. Finally, investigations at the microscopic and submicroscopic scale of CRFC (or any other ore mineral) may be important for understanding ore mineral formation and possibly improving downstream processing and REE recovery.

This chapter has been published with modification as: "*Conconi, R., Fumagalli, P., Capitani, G., 2023a. A multi-methodological study of the bastnäsite-synchysite polysomatic series: Tips and tricks of polysome identification and the origin of syntactic intergrowths. American Mineralogist 108, 1658–1668. https://doi.org/10.2138/am-2022-8678*".

3.2 Samples and sample preparation

The samples studied in this chapter come from Mount Malosa (Malawi) and were previously described by Guastoni et al. (2009, 2010) and Capitani (2019). All CRFC samples show a yellowish-reddish colour and are associated with aegirine (Fig. 3.1). Before instrumental investigations, all samples were embedded in epoxy resin, then cut parallel either to main or generic orientations, first roughly determined by visual inspection of the crystal habit, then following the EBSD results (see ahead): i) sample 9c1 sectioned parallel to the x-y plane (z-axis perpendicular to the section); ii) samples 3 and 9c2 sectioned parallel to the y-z plane (z-axis in the plane of the section); iii) sample 9b and 6 sectioned parallel to a generic orientation (z-axis at high angle and at low angle to the section, respectively). Here, the x, y, and z directions correspond to the crystallographic axes ***a***, ***b***, and ***c***, respectively. Electron transparent TEM mounts were prepared from sample 9c2, i.e. the one with the optimal orientation to study syntactic intergrowths, which alternate along the c-axis (Donnay and Donnay, 1953). To study the effect of mineral orientation on the Raman signal, a ½ λ wave plate was used to polarize the light. Spectra were obtained with two different polarization directions of the incident electric field vector: **E** ⊥ z and **E** || z in samples 3 and 9c2; **E** || y and **E** ~|| x in sample 9c1.

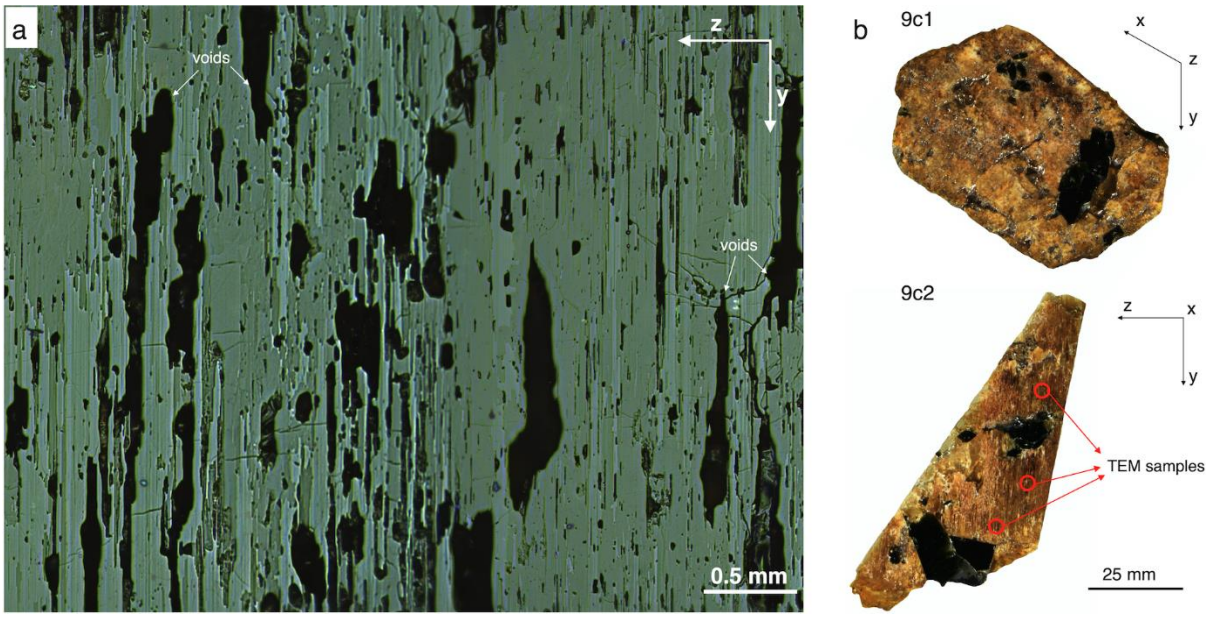

Figure 3.1. a) Reflected light optical micrograph of sample 9c2 showing the typical banding contrast due to syntactic intergrowths. The black areas are voids. B) Stereomicroscopic photos of samples 9c2 and 9c1 with their respective orientations obtained through EBSD. Red circles represent the positions where the 3 mm copper rings were placed to extract TEM samples.

3.3 Results

3.3.1 Microstructure and composition (SEM-EDS results)

Syntactic intergrowths in CRFC were studied by SEM-EDS for a first glimpse of the microstructure and of chemical variability at a microscopic scale. As expected, BSE images show the parallel banding typical of CRFC syntactic intergrowths (Fig. 3.2). EDS spot analyses were acquired within bands showing homogeneous grey tones. The good agreement between

these analyses and those acquired by WDS in a previous study of different crystals from the same samples (Guastoni et al., 2009), testifies that EDS is accurate enough for the identification of microscopic CRFC polysomes, being at the same time much faster than WDS (Table 3.1). EDS analyses show an inverse correlation of the Ca/(Ca+REE) ratio with the BSE intensity (brightness) of the bands. All the measured phases are Ce-dominant and contain La and Nd as other major REE, whereas Sm, Y, Pr and Gd are present as minor components (Table 3.2). An exception is represented by synchysite, where Y is more abundant than La and Nd. Fluorine is underestimated in SEM-EDS analyses due to its tendency to diffuse under the influence of a highly focused electron beam. Overall, the chemical compositions of lamellae range from bastnäsite to synchysite, depending on the sample, and align almost continuously between röntgenite, parisite and the B_2S polysome (Fig. 3.2). In particular, other than compositions close to bastnäsite, parisite, röntgenite and synchysite [ideal Ca/(Ca+REE) ratio of 0, 0.33, 0.40 and 0.50, respectively], lamellae with Ca/(Ca+REE) of 0.23 and 0.27, close to the B_2S polysome (0.25), and lamellae with a Ca/(Ca+REE) of 0.36 (Table 3.2) have been often encountered. Moreover, a few analyses with a Ca/(Ca+REE) ratio of 0.20, theoretically corresponding to polysomes B_3S, 0.14 (B_5S) and 0.29 (B_3S_2), have been collected. At this level, it is not known whether the determined compositions correspond to ordered polysomes or arise from disordered intergrowths at the nanoscale.

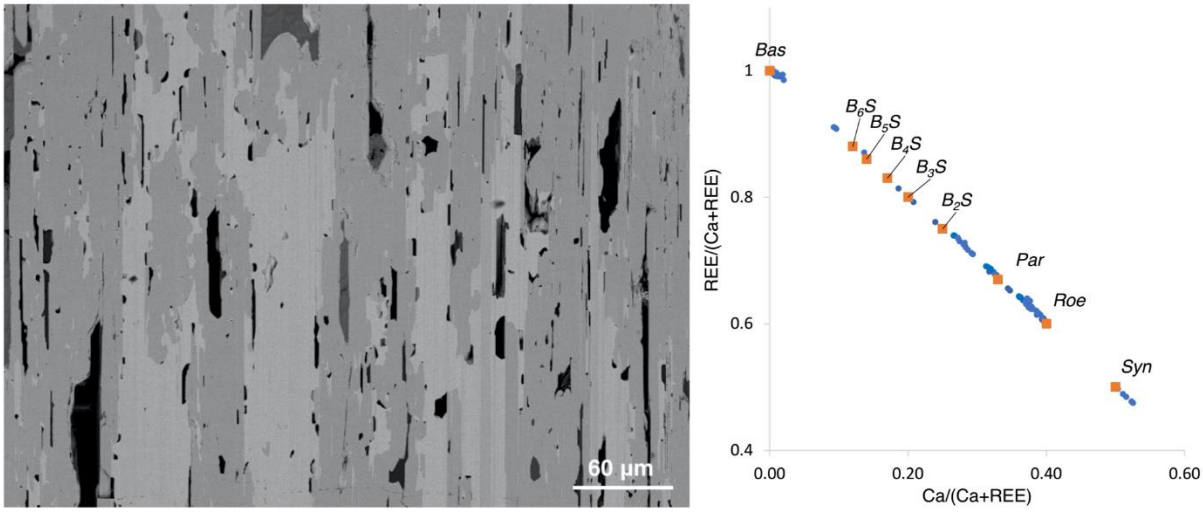

Figure 3.2. Left: SEM-BSE image of sample 9c2 showing the syntactic intergrowths of different CRFC polysomes. The compositional contrast is consistent with the average Z-number of the analysed phases: dark grey corresponds to röntgenite, light grey to bastnäsite and intermediate grey tones to parisite and other intermediate polysomes (black areas are voids). Right: Ca/(Ca+REE) vs. REE/(Ca+REE) plot of EDS analyses (blue dots) along with ideal compositions of existing and theoretical polysomes (orange squares). Most of the analysed lamellae show a composition within the B_2S–röntgenite join. Compositions deviating from the ideal ratios (but also those matching the ideal ratios!) may be due to compositional faults (see TEM section).

Table 3.1 Comparison between EDS and WDS analyses of bastnäsite, parisite and synchysite.

Mineral phases	EDS (this study)	WDS (Guastoni et al., 2009)
Bastnäsite	$(Ce_{0.52}La_{0.27}Nd_{0.13}Pr_{0.04}Sm_{0.01}Gd_{0.01})_{0.98}(CO_3)F_{0.63}$	$(Ce_{0.51}La_{0.32}Nd_{0.09}Y_{0.01}Pr_{0.04}Sm_{0.01})_{0.98}(CO_3)(F_{0.95}OH_{0.07})_{1.02}$
Parisite	$Ca_{0.96}(Ce_{1.04}La_{0.56}Nd_{0.27}Y_{0.01}Pr_{0.09}Sm_{0.02}Gd_{0.01})_{2.00}(CO_3)_3F_{1.33}$	$Ca_{0.92}(Ce_{1.03}La_{0.53}Nd_{0.27}Y_{0.04}Pr_{0.10}Sm_{0.04})_{2.01}(CO_3)_3(F_{1.70}OH_{0.30})_2$

Synchysite	$Ca_{1.04}(Ce_{0.35}La_{0.17}Nd_{0.13}Y_{0.21}Pr_{0.03}Sm_{0.02}Gd_{0.03})_{0.94}(CO_3)_2F_{0.97}$	$Ca_{0.99}(Ce_{0.42}La_{0.22}Nd_{0.13}Y_{0.19}Pr_{0.04}Sm_{0.03}Th_{0.01})_{1.04}(CO_3)_2(F_{0.79}OH_{0.21})_1$

Table 3.2. SEM-EDS analyses of CRFC from Malawi expressed as atoms per formula unit (a.p.f.u.) on the basis of 1, 4, 3, 1, 5 and 2 cations for bastnäsite, *B_2S*, parisite, unknown polysome, röntgenite and synchysite, respectively. Number of average point analysis in brackets.

Polysome	Bastnäsite											
Sample		9b			9c1			9c2			6	
Mean	(11)	Min	Max	(16)	Min	Max	(14)	Min	Max	(13)	Min	Max
F	0.32	0.30	0.35	0.28	0.24	0.29	0.64	0.60	0.71	0.25	0.23	0.28
Ca	0.02	0.00	0.07	0.03	0.00	0.09	0.03	0.00	0.09	0.01	0.00	0.06
Y	0.01	0.00	0.01	0.00	0.00	0.01	0.01	0.00	0.01	0.00	0.00	0.03
La	0.29	0.24	0.41	0.26	0.24	0.29	0.26	0.24	0.29	0.30	0.24	0.32
Ce	0.48	0.46	0.51	0.49	0.46	0.52	0.49	0.46	0.52	0.52	0.50	0.53
Nd	0.13	0.09	0.16	0.15	0.14	0.17	0.14	0.13	0.15	0.12	0.10	0.16
Pr	0.05	0.04	0.06	0.05	0.04	0.05	0.01	0.00	0.01	0.00	0.00	0.01
Sm	0.01	0.00	0.02	0.01	0.00	0.01	0.05	0.04	0.05	0.00	0.00	0.00
Gd	0.00	0.00	0.00	0.00	0.00	0.00	0.01	0.01	0.02	0.04	0.04	0.06
Sr	0.00	0.00	0.01	0.01	0.00	0.02	0.01	0.00	0.01	0.00	0.00	0.00
Sum REE	0.98			0.96			0.96			0.99		
Ca/(Ca+REE)	0.02			0.03			0.03			0.01		
Polysome	*B_2S*											
Sample		9b			9c1			9c2			6	
Mean	(4)	Min	Max	(4)	Min	Max	(3)	Min	Max	(3)	Min	Max
F	1.27	1.20	1.33	0.78	0.75	0.80	1.83	1.79	1.86	0.74	0.71	0.78
Ca	1.05	1.03	1.09	1.06	1.04	1.09	1.11	1.09	1.13	0.92	0.86	0.96
Y	0.03	0.02	0.03	0.02	0.01	0.02	0.00	0.00	0.01	0.06	0.04	0.10
La	0.80	0.79	0.81	0.73	0.72	0.75	0.78	0.73	0.82	0.75	0.61	0.84
Ce	1.50	1.46	1.52	1.44	1.44	1.46	1.49	1.49	1.49	1.48	1.43	1.56
Nd	0.41	0.39	0.42	0.51	0.49	0.53	0.41	0.39	0.43	0.53	0.45	0.65
Pr	0.16	0.15	0.16	0.16	0.14	0.17	0.02	0.02	0.03	0.04	0.00	0.06
Sm	0.03	0.03	0.04	0.04	0.02	0.05	0.13	0.12	0.14	0.07	0.02	0.10
Gd	0.00	0.00	0.00	0.01	0.00	0.02	0.03	0.03	0.03	0.15	0.13	0.19
Sr	0.03	0.03	0.04	0.04	0.03	0.04	0.02	0.02	0.03	0.00	0.00	0.00
Sum REE	2.92			2.90			2.87			3.08		
Ca/(Ca+REE)	0.26			0.27			0.28			0.23		
Polysome	Parisite											
Sample		9b			9c1			9c2			6	
Mean	(5)	Min	Max	(3)	Min	Max	(5)	Min	Max	(4)	Min	Max

F	0.91	0.56	1.05	0.44	0.35	0.50	1.29	1.16	1.36	0.49	0.44	0.60
Ca	0.95	0.92	1.04	1.01	0.96	1.04	0.98	0.96	1.05	1.00	0.95	1.04
Y	0.03	0.02	0.06	0.01	0.01	0.01	0.01	0.00	0.03	0.07	0.06	0.08
La	0.54	0.50	0.57	0.53	0.51	0.56	0.55	0.53	0.57	0.48	0.42	0.55
Ce	1.02	0.93	1.07	1.00	0.98	1.03	1.03	0.99	1.05	0.92	0.83	0.98
Nd	0.30	0.28	0.31	0.32	0.30	0.34	0.28	0.26	0.29	0.32	0.27	0.35
Pr	0.11	0.10	0.11	0.09	0.09	0.10	0.02	0.01	0.02	0.06	0.02	0.10
Sm	0.03	0.02	0.04	0.02	0.01	0.02	0.09	0.09	0.10	0.05	0.01	0.10
Gd	0.00	0.00	0.00	0.00	0.00	0.00	0.02	0.02	0.03	0.09	0.08	0.10
Sr	0.02	0.02	0.03	0.02	0.02	0.03	0.01	0.01	0.02	0.01	0.00	0.04
Sum REE	2.03			1.97			2.01			1.99		
Ca/(Ca+REE)	0.32			0.34			0.33			0.34		

Polysome	Unknown polysome											
Sample		9b			9c1			9c2			6	
Mean	(6)	Min	Max	(8)	Min	Max	(11)	Min	Max	(3)	Min	Max
F	0.24	0.20	0.32	0.16	0.15	0.17	0.39	0.35	0.47	0.14	0.14	0.15
Ca	0.36	0.35	0.37	0.35	0.34	0.36	0.36	0.35	0.37	0.36	0.35	0.37
Y	0.01	0.01	0.02	0.01	0.00	0.02	0.00	0.00	0.01	0.03	0.03	0.03
La	0.17	0.17	0.17	0.17	0.16	0.17	0.17	0.17	0.18	0.15	0.13	0.18
Ce	0.32	0.31	0.33	0.32	0.31	0.33	0.33	0.32	0.33	0.29	0.27	0.30
Nd	0.09	0.09	0.10	0.10	0.10	0.11	0.09	0.08	0.09	0.11	0.08	0.13
Pr	0.03	0.03	0.04	0.03	0.03	0.04	0.00	0.00	0.01	0.01	0.01	0.02
Sm	0.01	0.00	0.01	0.00	0.00	0.01	0.03	0.03	0.03	0.02	0.01	0.02
Gd	0.00	0.00	0.00	0.00	0.00	0.00	0.01	0.01	0.01	0.03	0.03	0.04
Sr	0.01	0.00	0.01	0.01	0.00	0.02	0.01	0.00	0.02	0.00	0.00	0.01
Sum REE	0.63			0.64			0.63			0.64		
Ca/(Ca+REE)	0.36			0.35			0.37			0.36		

Polysome	Röntgenite						Synchysite*			Mixed compositions		
Sample		9c2			6			3		9b	6	9c2
Mean	(15)	Min	Max	(6)	Min	Max	(9)	Min	Max	(2)	(2)	(2)
F	2.08	1.74	2.58	0.71	0.63	0.87	0.79	0.59	0.95	0.42	0.19	0.45
Ca	1.88	1.78	1.96	1.96	1.88	2.05	1.02	0.99	1.04	0.14	0.20	0.29
Y	0.09	0.05	0.12	0.15	0.12	0.17	0.22	0.21	0.23	0.01	0.02	0.00
La	0.82	0.79	0.86	0.74	0.59	0.86	0.17	0.16	0.19	0.23	0.17	0.19
Ce	1.54	1.48	1.59	1.38	1.26	1.48	0.36	0.33	0.41	0.44	0.37	0.37
Nd	0.43	0.40	0.46	0.48	0.36	0.62	0.12	0.11	0.14	0.12	0.16	0.10
Pr	0.01	0.00	0.03	0.06	0.00	0.13	0.03	0.03	0.03	0.03	0.02	0.00
Sm	0.14	0.13	0.16	0.06	0.00	0.12	0.02	0.01	0.03	0.02	0.03	0.03

Gd	0.04	0.02	0.05	0.14	0.11	0.16	0.02	0.01	0.03	0.01	0.05	0.01
Sr	0.04	0.01	0.10	0.02	0.00	0.06	0.01	0.00	0.01	0.01	0.00	0.00
Sum REE	3.08			3.01			0.95			0.86	0.80	0.71
Ca/(Ca+REE)	0.38			0.39			0.52			0.14	0.20	0.29

*Minor Th and Si were also detected

3.3.2 Lamellae orientation (EBSD results)

EBSD analyses were undertaken to: i) establish the initial orientation of the samples; ii) align the sample for oriented cuts in view of both Raman and TEM investigations; iii) test the method's capability to discriminate different polysomes. Not surprisingly, EBSD results allowed to establish the sample orientation, to set up the oriented cuts and to ascertain the effective syntactic relationship among all the detected CRFC phases, but failed to distinguish among different polysomes (Fig. 3.3). The latter can be easily understood if one takes into account that electron diffraction (alike X-ray diffraction) is dominated by heavy atoms, and that CRFC of the *BS* series, although monoclinic, have a hexagonal stacking of heavy atoms (Ca and REE), exactly as bastnäsite, the only effective hexagonal term (Ni et al., 1993, 2000; Wang, 1994). Different polysomes can be actually distinguished through EBSD maps if EDS chemical information is acquired at the same time, and the map elaborated with both contributions (50% EDS and 50% EBSD). In this case, the syntactic intergrowths are correctly indexed, but the method loses interest since EDS has a spatial resolution (few micrometres) two orders of magnitude worse than EBSD (tens of nanometres).

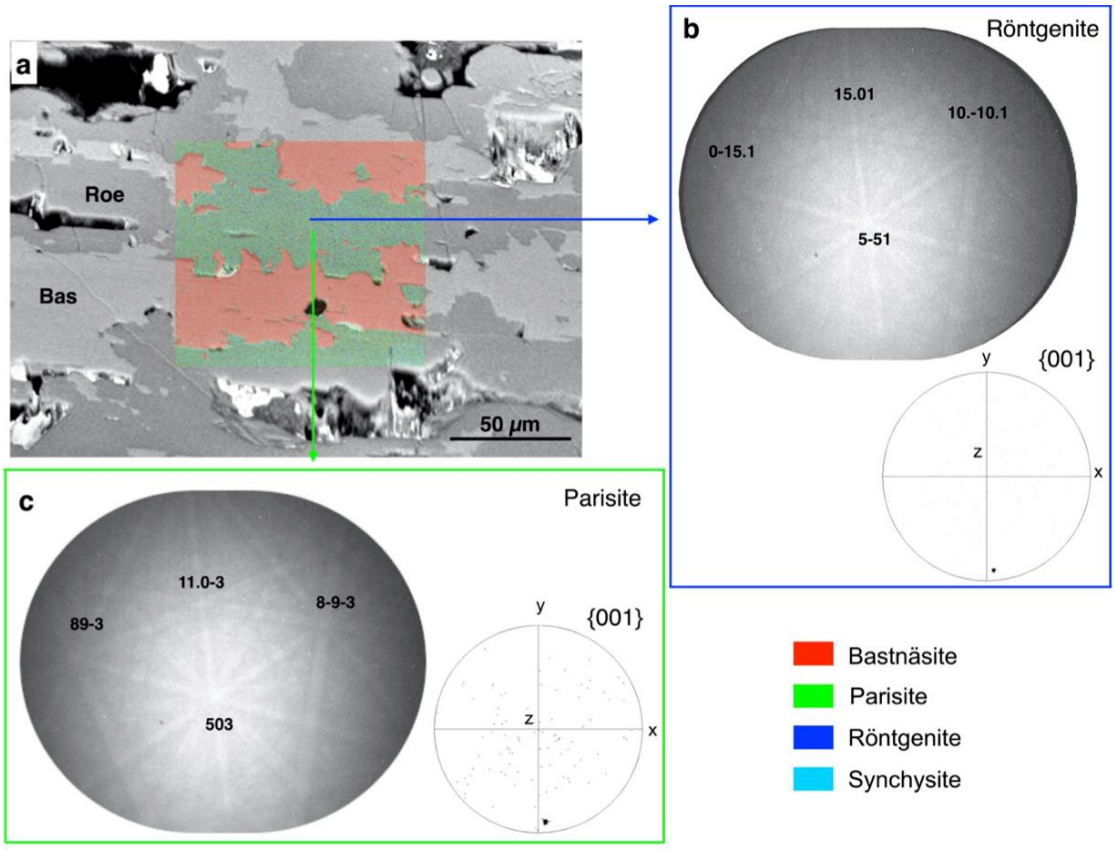

Figure 3.3. a) BSE image with superposed EBSD phase map of sample 9c2. The legend reports the colouring scheme of all phases considered by the program. The EBSD system indexes correctly bastnäsite (Bas, red) but fails to correctly identify röntgenite (Roe, blue), which is mostly misinterpreted as parisite (green). As a matter of fact, the EBSD of röntgenite (b) and parisite (c), are geometrically indistinguishable, leading to ambiguous zone axis indexing (black numbers). However, as reported in the stereographic projections, EBSD gives consistent and useful information about the crystal orientation relationship.

3.3.3 Raman spectroscopy

Raman spectroscopy analyses were taken on lamellae previously characterized by SEM-EDS, in an attempt to correlate the Raman signal with chemical composition, aiming at distinguishing different polysomes. Peak assignment was done according to White (1974), Buzgar and Apopei (2009) and Zeug et al. (2021). The following internal vibrational modes of the carbonate group were identified: i) symmetric stretching [$v_1(CO_3)$]; ii) out-of-plane bending [$v_2(CO_3)$]; iii) antisymmetric stretching [$v_3(CO_3)$]; iv) in-plane bending [$v_4(CO_3)$] (Table 3.3 and Fig. 3.4).

Table 3.3. Summary of the (CO_3) vibrational modes in CRFC and their positions as determined in this study.

Mode	Bastnäsite	Intermediate polysomes	Synchysite
v_1 – symmetric stretching	~1095 cm^{-1}	~1081 cm^{-1} ~1091-1095 cm^{-1} ~1099 cm^{-1}	~1081 cm^{-1} ~1099 cm^{-1}
v_2 – out-of-plane bending		~870 cm^{-1}	
v_3 – antisymmetric stretching		~1440 cm^{-1}	
v_4 – in-plane bending		665–754 cm^{-1}	

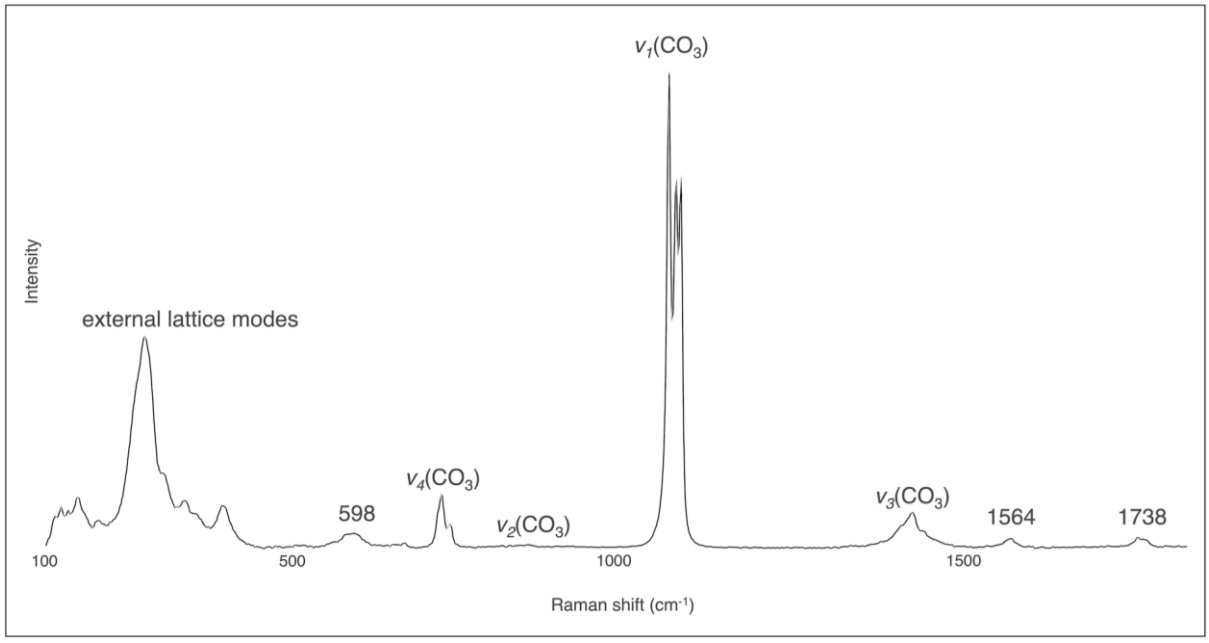

Figure 3.4. Raman spectrum of röntgenite showing the main vibrational modes of CRFC.

Since the intensity of Raman peaks changes in relation to both crystal orientation and laser polarization, four different configurations were investigated, whose details and related Porto's

notations (Damen et al., 1966) are reported in Table 3.4. The highest intensity of the $v_1(CO_3)$ stretching vibration was obtained in sample 9c2 with the $x\left(z_y^z\right)\bar{x}$ configuration. Conversely, the lowest intensity was obtained with the $z\left(y_x^y\right)\bar{z}$ setting (Fig. 3.5). Orientation of the polysomes and laser polarization influence only the intensity of the bands, not their positions.

In agreement with Zeug et al. (2021), we found that the $v_4(CO_3)$ in-plane bending is in the range 665–754 cm^{-1} and seems separated into two sub-regions. The $v_2(CO_3)$ out-of-plane bending is around 870 cm^{-1}. The $v_3(CO_3)$ antisymmetric stretching is around 1440 cm^{-1} and is orientation dependent. The $v_1(CO_3)$ symmetric stretching is around 1100 cm^{-1} and it is split into three bands in intermediate polysomes: at ~1081 cm^{-1}, 1091-1095 cm^{-1} and ~1099 cm^{-1}, whose relative intensities vary with composition (i.e., Ca/REE ratio, see also Fig. 3.14). End members behave somewhat differently: bastnäsite shows only one intense peak at ~1095 cm^{-1} and synchysite two bands at 1081 cm^{-1} and 1099 cm^{-1} (Table 3.3 and Fig. 3.6). As in Zeug et al. (2021) we also detected other bands at 598, 1564 and 1738 cm^{-1}, whose origin was not clarified (Fig. 3.4).

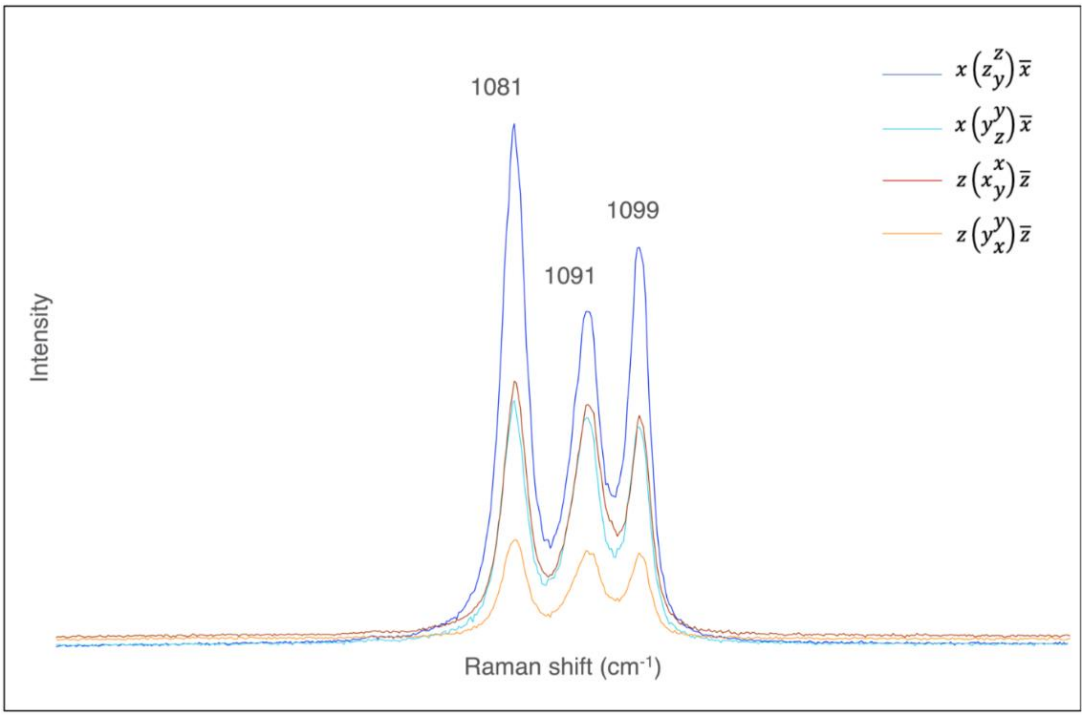

Figure 3.5. $v_1(CO_3)$ intensity variation in röntgenite as a function of the crystal orientation and laser polarization.

Table 3.4. Crystal and laser beam settings and related Porto's notation

Mineral section	Beam direction	E polarization	Porto's notation
y z	*x*	*z*	$x\left(z_y^z\right)\bar{x}$
y z	*x*	*y*	$x\left(y_z^y\right)\bar{x}$
y x	*z*	*y*	$z\left(y_x^y\right)\bar{z}$
y x	*z*	*x*	$z\left(x_y^x\right)\bar{z}$

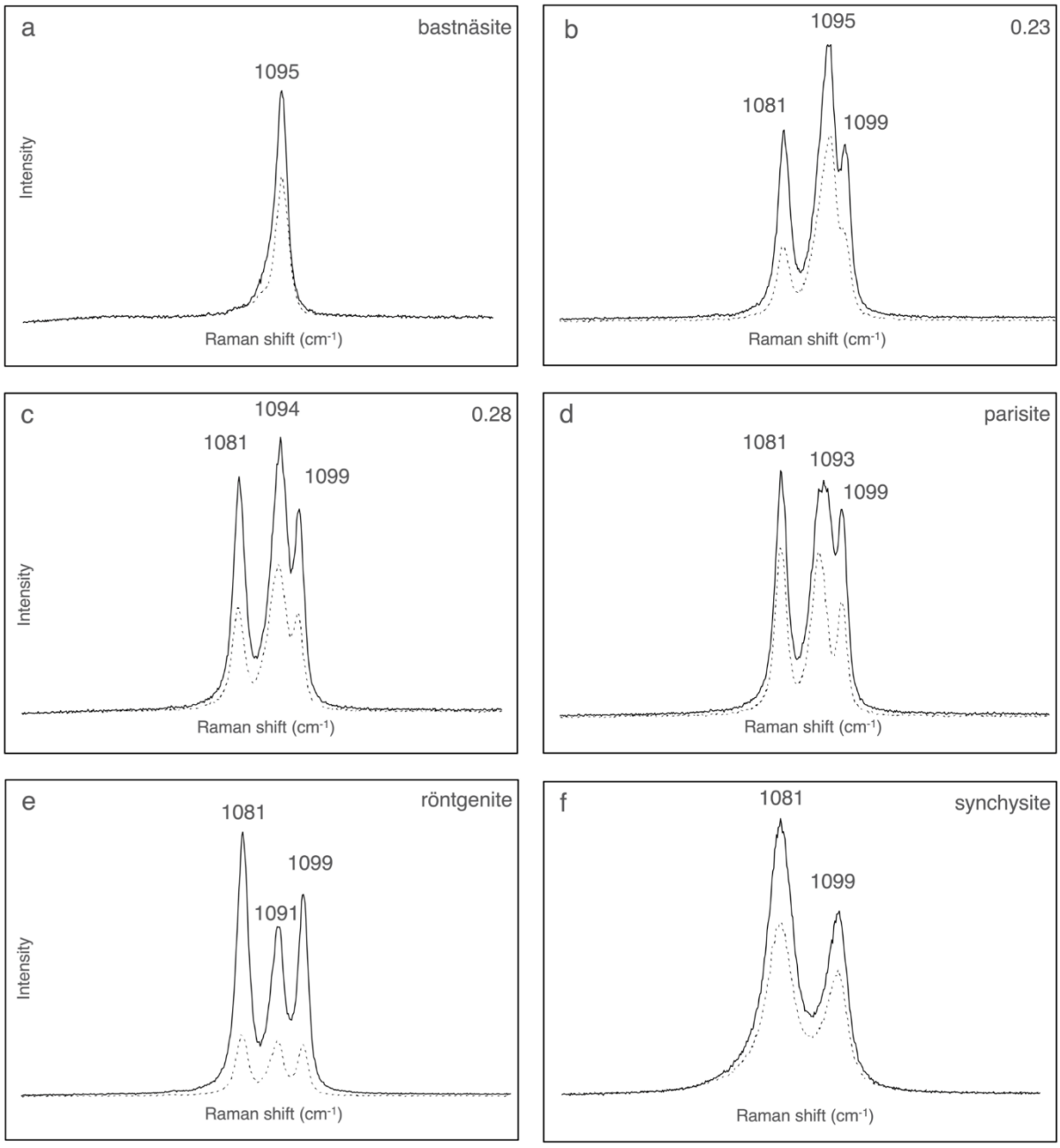

Figure 3.6. (a) to (f) Symmetric stretching vibration [$v_1(CO_3)$] in the different polysomes, from the Ca-poorest phase bastnäsite (a), nominally Ca-free, to the Ca-richest phase synchysite with an ideal Ca/(Ca+REE) = 0.50 (f). (b) and (c) were obtained on lamellae homogeneous in BSE images and with Ca/(Ca+REE)'s of 0.23 and 0.27, respectively, close to the B_2S polysome (0.25). Note the strong orientation dependence of the intensity: $v_1(CO_3)$ is maximal when the laser is polarized parallel to the z axis ($x\left(z_y^z\right)\bar{x}$, solid line) and minimal when the laser is polarized perpendicular to the z axis ($x\left(y_z^y\right)\bar{x}$, dotted line).

3.3.4 Nanostructure (TEM results)

The sample studied by SEM-EDS and Raman spectroscopy with a favourable orientation for the study of syntactic intergrowths (i.e. with the z-axis laying on the observation plane, sample 9c2) was prepared for TEM in order to elucidate the structural state associated with the encountered compositions. Ordered regions in sample 9c2 are rare and limited to less than 1

μm along the stacking direction. Indeed, the most recurrent microstructure is given by a pervasive occurrence of stacking faults (Fig. 3.7a) affecting bastnäsite and parisite, by far the most abundant phases detected in the sample (Fig. 3.7 and 3.8). Limited regions of B_2S and B_5S showing consistent compositions (Table 3.5) were also detected (Fig. 3.9), in agreement with SEM-EDS. Few point analyses with a Ca/(Ca+REE) ratio of 0.29, closed to B_3S_2 were measured by TEM-EDS, and its presence was confirmed by HRTEM images (Fig. 3.10).
Moreover, two long range polysomes with repeat distances of ~32 nm and ~23 nm were observed (Fig. 3.11 and 3.12). In the SAED patterns of these polysomes, the supercell reflections are too weak and superposed to be resolved. However, both patterns show modulated subcell reflections at ~5 Å, suggesting that bastnäsite may be the most abundant building block in these phases. Furthermore, the absence of streaks along *00l*, *11l* and *22l*, indicates the absence of polysomatic and polytypic disorder. This was confirmed by examining the HR images (Fig. 3.12b) of the 23 nm polysome. The images reveal that the ~23 nm long range polysome is primarily composed of bastnäsite, with the presence of eight vaterite layers. This forms an ordered sequence of $VB_7VB_3VB_{12}VB_3VB_8VB_3VB_3VB_2$ (V_8B_{41}), repeating for at least ~200 nm.
Even though SEM-EDS and Raman spectroscopy suggest the abundant presence of röntgenite, clear evidence of this polysome has not been confirmed by TEM. Similarly, the abundant lamellae with a Ca/(Ca+REE) ratio of 0.36 detected by SEM-EDS (Table 3.2) were not observed by TEM. Finally, a new parisite-(Ce) polymorph was detected, distinguished from normal parisite (Ni et al., 2000) and from the other polymorph described by Capitani (2019) by having twice the repeat distance along **c*** (~56 vs. ~28 Å, respectively), suggesting a repetition of four basic *BS* modules (~14 Å) along the stacking direction (Fig. 3.13).

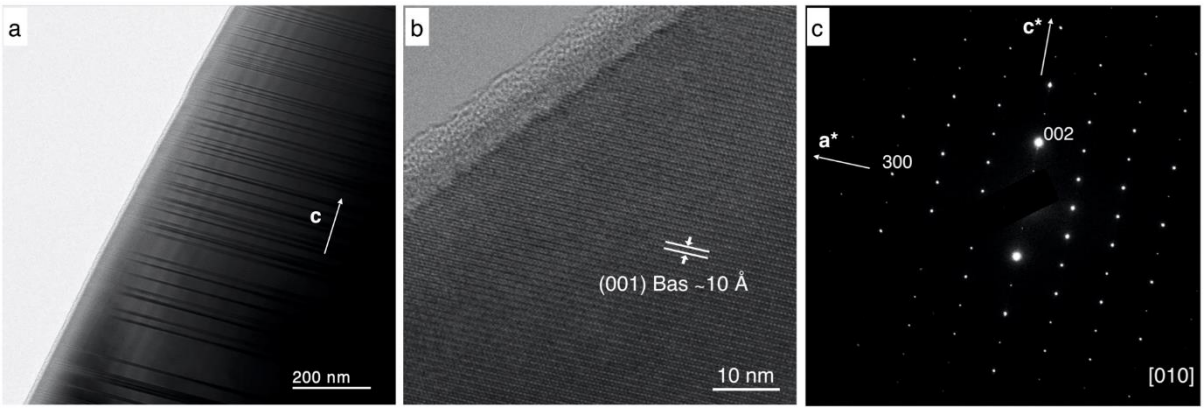

Figure 3.7. a) Recurrent microstructure in CRFC from Malawi (sample 9c2), made of dense stacking faults. b) Ordered region of bastnäsite as seen down [010] and related SAED pattern (c).

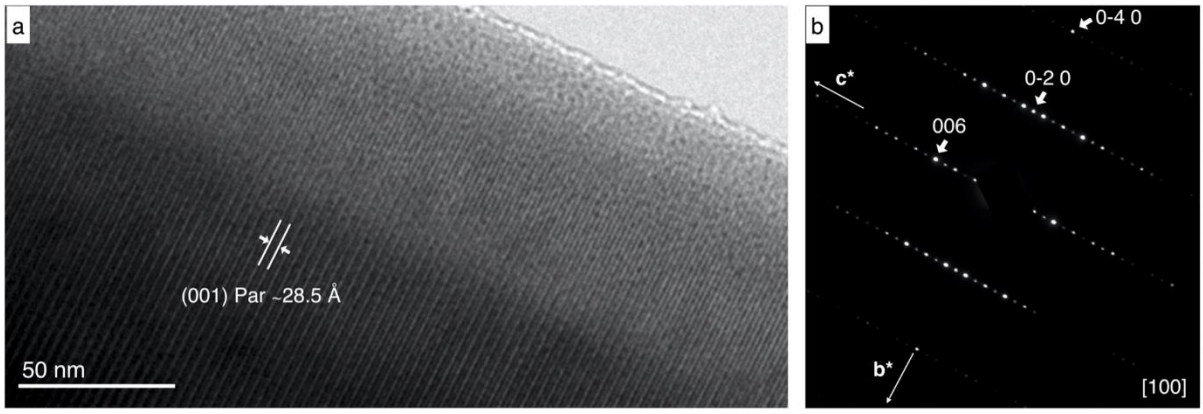

Figure 3.8. a) Ordered region of parisite (free of compositional faults) as seen down [100] and corresponding SAED pattern (b).

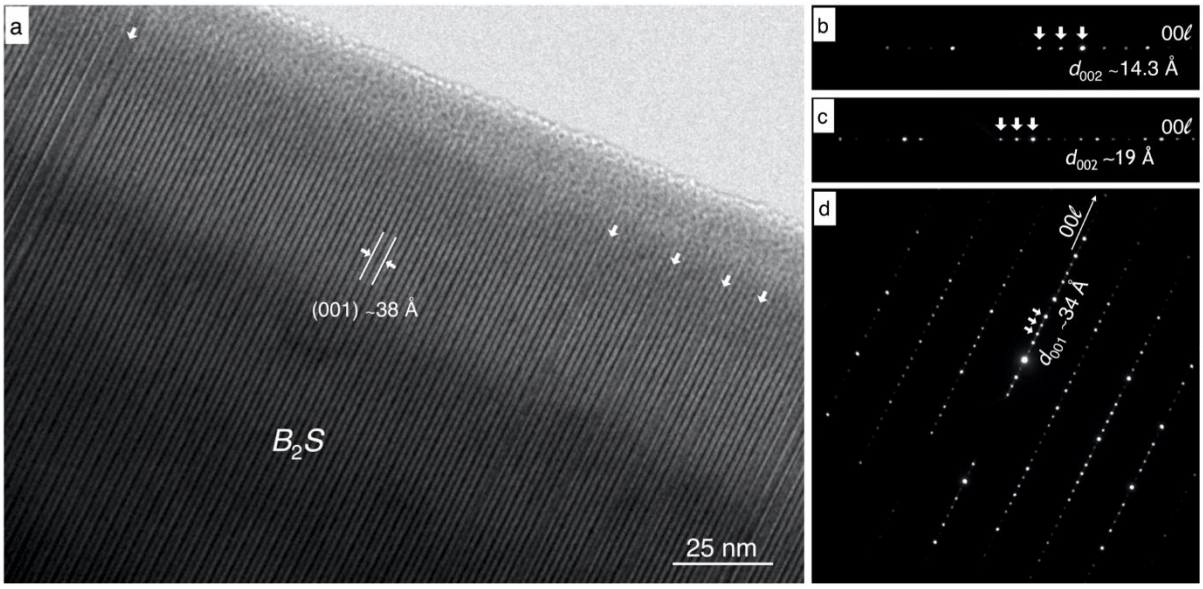

Figure 3.9. a) Lamella ~140 nm thick with a *c*-spacing of ~38 Å, consistent with the B_2S polysome. Some stacking faults delimiting the ordered region are indicated by arrows. b) 00*l* row of parisite as compared to the 00*l* row of the B_2S polysome (c) to emphasize the different periodicity of the 002 half-cell. (d) SAED pattern of a further polysome with 001 periodicity of ~34 Å, consistent with B_5S, whose structure, however, needs to be confirmed.

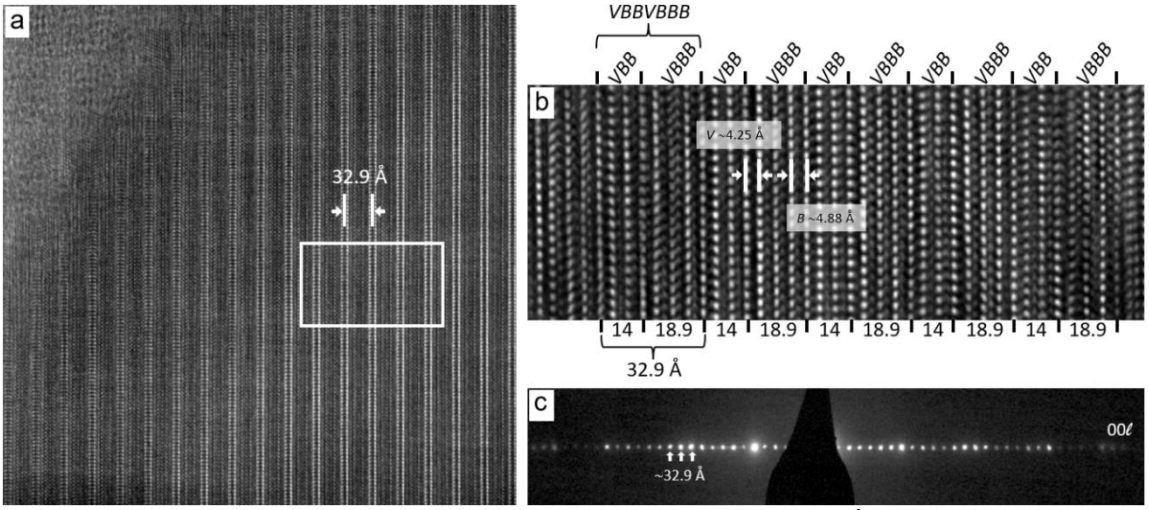

Figure 3.10. a) Ordered region of B_3S_2 polysome with a *c*-spacing of 32.9 Å. The stacking arrangement, observable in the HR image (b), in terms of *VB* notation is: *VBBVBBB*, which is a parisite portion (*VBB*) with a B_2S portion (*VBBB*). (c) SAED pattern representing only the 00*l* row.

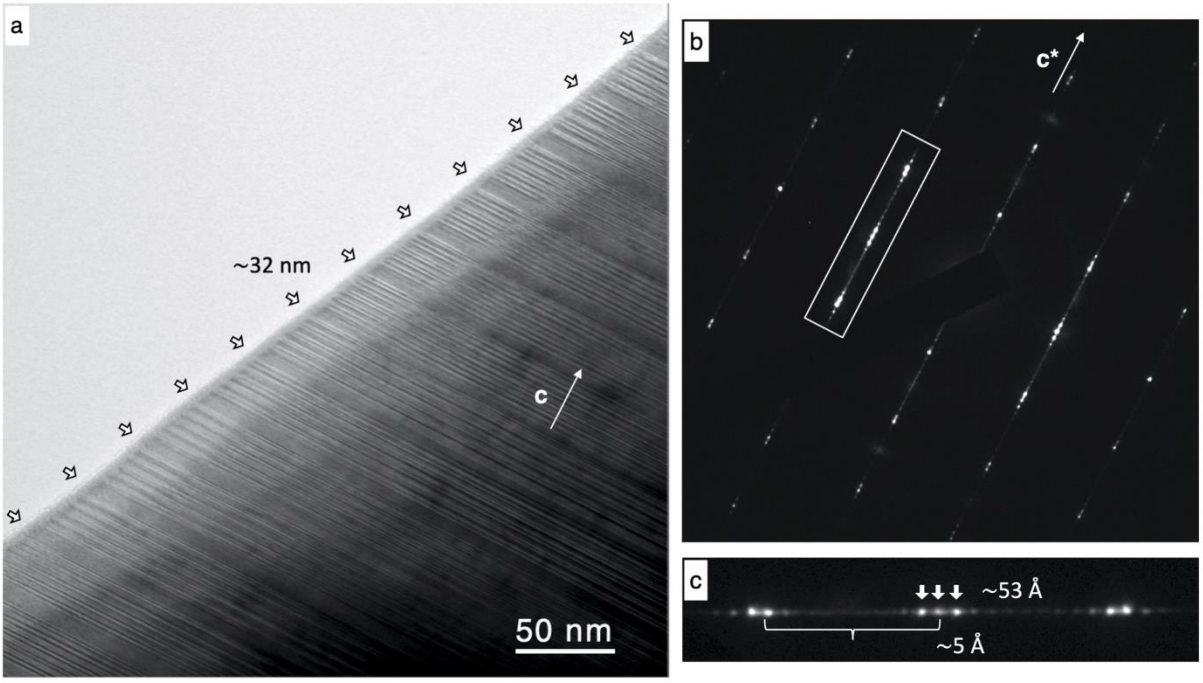

Figure 3.11. a) Long range polysome with a repeat distance of ~32 nm (the periodic region extends beyond the observed field of view, up to ~500 nm in total). b) Related SAED pattern. The supercell reflections cannot be resolved, because they are too weak and superposed. The strongest sub cell reflections showing a periodicity of ~53 Å, whose intensity is further modulated at ~5 Å (brace), suggest a main building block of ~53 Å based on single *B*-layers, which we may tentatively indicate as the thick, darker lamellae in (a) (arrows).

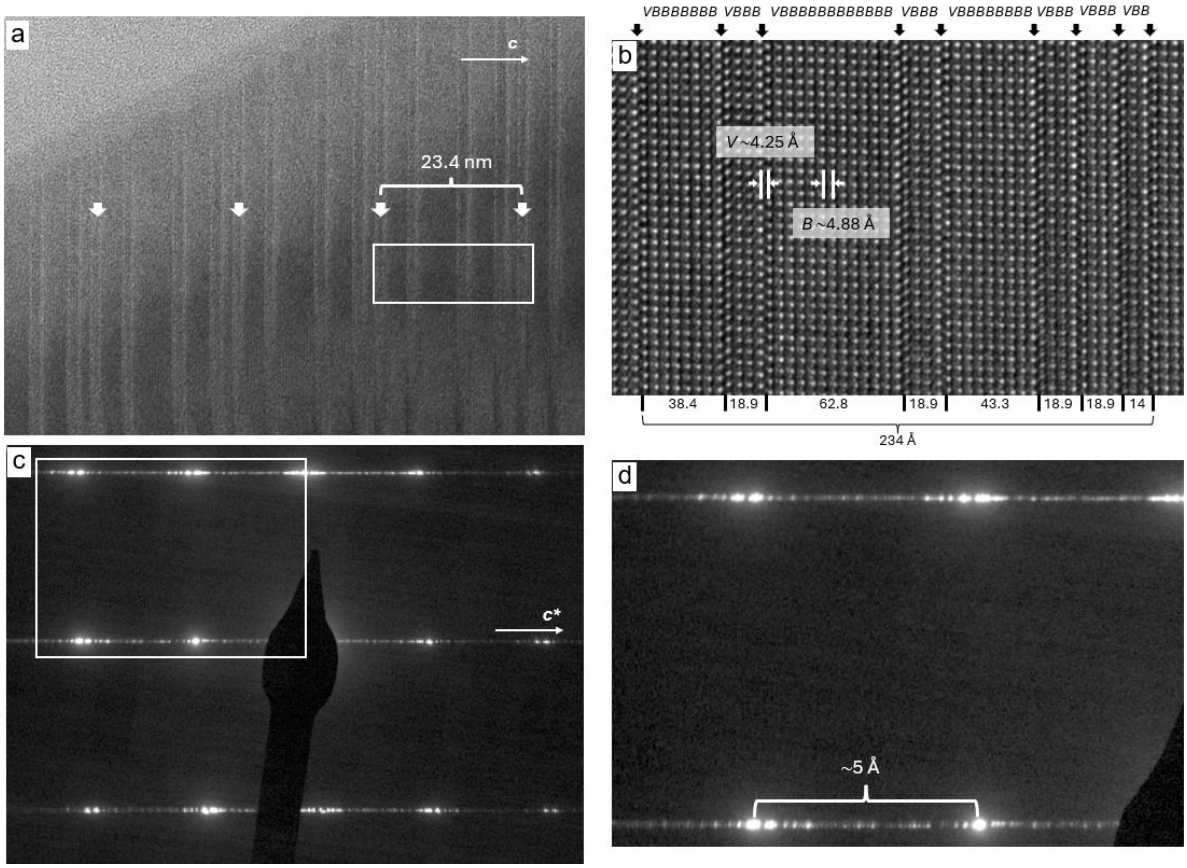

Figure 3.12. a) Long range polysome with a repeat distance of ~23 nm. b) HR image of (a) showing that the stacking sequence consist of 41 bastnäsite layers and 8 vaterite layers. c, d) Related SAED patterns showing a subcell reflection modulated at ~5 Å. The absence of streaks along 00*l* and 11*l* suggests long periodic order, as indicated by the HR image.

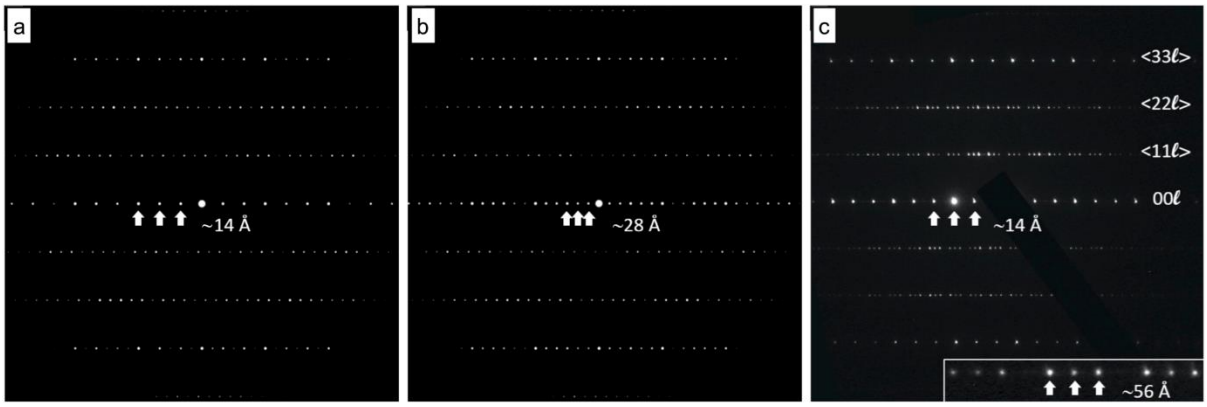

Figure 3.13. SAED patterns of parisite-(Ce) structures along [1$\bar{1}$0]: a) Ni et al. (2000); b) Capitani (2019) (both are simulations obtained with the CrystalMaker X software); c) experimental pattern of the new parisite polymorph detected in this study; inset: zooming of the 11*l* row to highlight the ~56 Å periodicity along **c***, which distinguishes the last from the former two structures (~28 Å), suggesting a new polymorph with a double *c* parameter and a stacking of four *BS* single units (~14 Å).

Even considering that by TEM is not possible to explore the whole area explored by SEM and that we could have missed some compositions, our findings suggest that, at least in part, the intermediate compositions detected by SEM-EDS on apparently homogeneous lamellae may result from sub-microscopic compositional faults (polysomatic faults), not resolved in BSE images, matching only by accident the composition of a theoretical polysome.

Compositional faults in bastnäsite can only be Ca-rich through local insertion of vaterite-like slabs, whereas in parisite they can be either Ca-rich, or Ca-poor, the latter resulting from a bastnäsite-like slabs insertion. In the studied samples, compositional faults in parisite are mostly Ca-poor. These conclusions are supported by nanoscale EDS analysis and HRTEM imaging. The Ca/(Ca+REE) ratio slightly higher than 0 in bastnäsite and lower than 0.33 in parisite (Table 3.5) can be interpreted in this way.

Figure 3.14 reports bright field STEM images and related compositional line scans across a Ca-poor lamella in parisite and Ca-rich lamellae in disordered bastnäsite. In both cases, a clear inverse correlation between Ca and Ce can be observed.

Figure 3.15 shows an HRTEM image of bastnäsite (*c* ~10 Å) with compositional faults consistent with B_2S and B_3S single slabs, with thickness of ~19 and ~24 Å, respectively. The random occurrence of Ca-bearing compositional faults may explain the minor Ca content sometimes detected in bastnäsite and could cause an accidental matching of SEM-EDS analyses with intermediate polysome compositions, leading to misinterpretation.

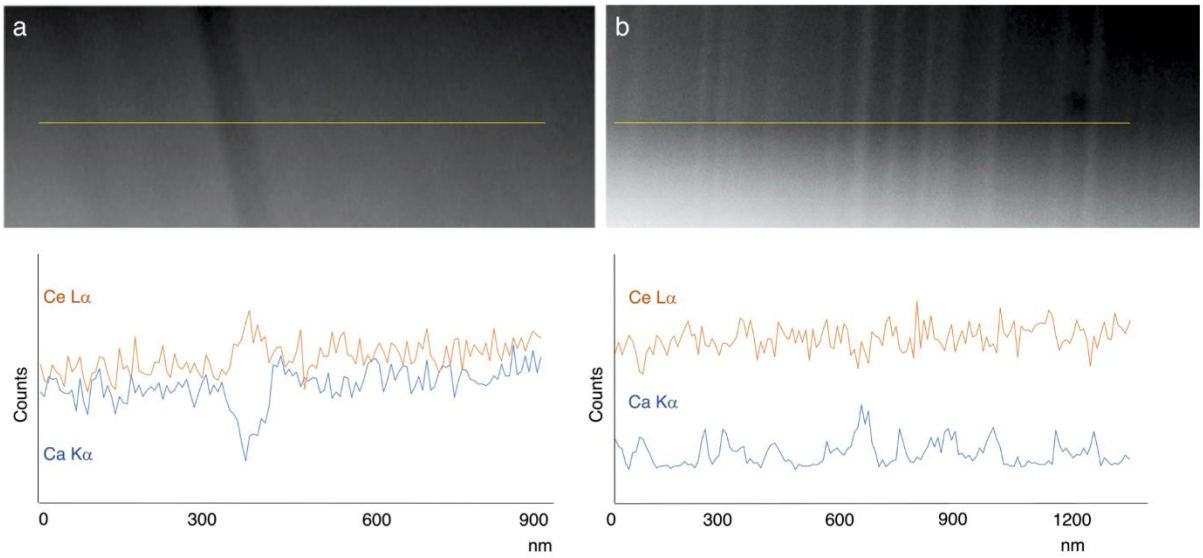

Figure 3.14. BF-STEM images (top) and corresponding compositional line scans (bottom) across a thick lamella within parisite (a) and disordered bastnäsite (b). Note the Ca decrease and the Ce increase at the lamella in parisite and the Ca-Ce inverse correlation in bastnäsite.

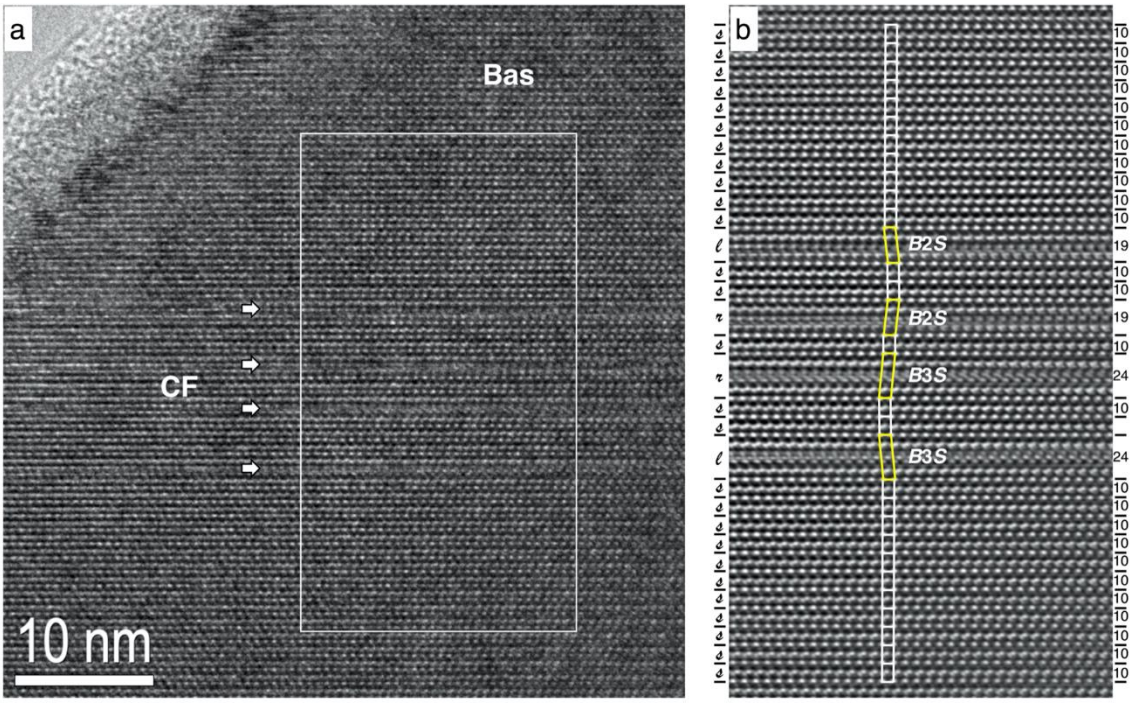

Figure 3.15. a) HRTEM image of bastnäsite down [010] (SAED pattern similar to Fig. 3.7c) including some compositional faults (CF, arrows). B) Fourier filtered image of the rectangular area in (a). The unit-cell-scale analysis reveals that these CF can be explained by the insertion of single B_2S and B_3S slabs with thickness along *c* of ~19 and ~24 Å, respectively. Other than affecting the slab thickness (approximate values in Å on the right), the CF causes a shift on the (001) plane (*s* = straight, *l* = left, *r* = right shift).

Table 3.5. TEM-EDS analysis of CRFC from Malawi. Cations per formula unit on the basis of 1, 4, 3, 1, for bastnäsite, B_2S, parisite and mixed compositions, respectively. Number of average point analyses in brackets.

Polysome	Bastnäsite			B_2S			Parisite			Mixed compositions		
Mean	(16)	Min	Max	(18)	Min	Max	(9)	Min	Max	(2)	(2)	(2)
Ca	0.03	0.00	0.09	1.00	0.87	1.12	0.91	0.89	0.94	0.14	0.21	0.29
Y	0.01	0.00	0.02	0.03	0.01	0.06	0.02	0.02	0.03	0.01	0.01	0.00
La	0.25	0.23	0.28	0.80	0.77	0.84	0.55	0.53	0.57	0.21	0.21	0.19
Ce	0.49	0.43	0.53	1.57	1.46	1.65	1.06	1.05	1.08	0.44	0.40	0.36
Pr	0.04	0.03	0.06	0.12	0.07	0.15	0.09	0.08	0.11	0.04	0.03	0.03
Nd	0.14	0.12	0.16	0.42	0.33	0.50	0.30	0.26	0.32	0.14	0.12	0.11
Sm	0.02	0.00	0.03	0.04	0.00	0.07	0.04	0.02	0.05	0.02	0.02	0.02
Gd	0.01	0.00	0.03	0.02	0.00	0.04	0.02	0.01	0.03	0.01	0.01	0.00
Sum REE	0.97			3.00			2.09			0.86	0.79	0.71
Ca/(Ca+REE)	0.03			0.25			0.30			0.14	0.21	0.29

3.4 Discussion and Conclusions

3.4.1 Polysome detectability trough Raman spectroscopy

According to Raman results, the identification of the basic CRFC is possible through the symmetric $v_1(CO_3)$ stretching vibration at ~1100 cm^{-1} (Fig. 3.6). Bastnäsite and synchysite can be easily distinguished from other polysomes by their strong Raman bands: bastnäsite shows a band at 1095 cm^{-1}, while synchysite displays two bands at 1081 cm^{-1} and 1099 cm^{-1}. Parisite, B_2S and röntgenite all have three bands at ~1081 cm^{-1}, ~1091-1095 cm^{-1} (hereafter 1091 cm^{-1}) and ~1099 cm^{-1}, which vary only in intensity. Following Zeug et al. (2021), the identification of these intermediate polysomes is possible through the 1091 cm^{-1}/1081 cm^{-1} intensity ratio. We found this ratio to decrease linearly with the Ca/(Ca+REE) ratio for samples with **E** // z and with a parabolic shape for samples with **E** ⊥ z (Fig. 3.16).

The number and position of the symmetric $v_1(CO_3)$ stretching vibration Raman bands depend on the valence and ionic radius (Adler and Kerr, 1963) of the groups neighbouring the CO_3^{2-} groups. There are two different types of CO_3^{2-} layers in the CRFC structure: those in contact on both sides with CeF-layers (or *e*-layers), and those in contact with one CeF-layer and one Ca-layer (or *g*-layers) (Donnay and Donnay, 1953). Only (symmetric) *e*-layers are present in bastnäsite (Yang et al., 2008), resulting in one strong band at 1095 cm^{-1}. Conversely, only (asymmetric) *g*-layers are present in synchysite (Wang et al., 1994), resulting in two different bands at 1081 and 1099 cm^{-1}. Both *e*-layers and *g*-layers are present in intermediate polysomes like parisite, B_2S and röntgenite (Ni et al., 1993, 2000), leading to a tripartition of the symmetric $v_1(CO_3)$ stretching vibration.

TEM-EDS analysis suggests that ordered regions in CRFC syntactic intergrowths from Malawi are smaller than expected according to SEM-EDS imaging. Consequently, nanoscale compositional faults in bastnäsite and parisite, not resolved in SEM-BSE images, may affect the Ca/(Ca+REE) ratio, which could match only by accident the composition of a real

polysome. In light of these results, Raman spectroscopy, whose spatial resolution is ~1 μm, needs to be critically re-examined. We believe that while the Raman signal is sensitive to different abundances of *e*- and *g*-layers, which vary with composition and polysome type, it is not sensitive to the order of layers within the analysed volume. Therefore, whereas Raman spectroscopy could be a valid and faster method to probe the Ca/(Ca+REE) content of CRFC, it may not be suitable to distinguish between ordered and disordered intergrowths with similar compositions.

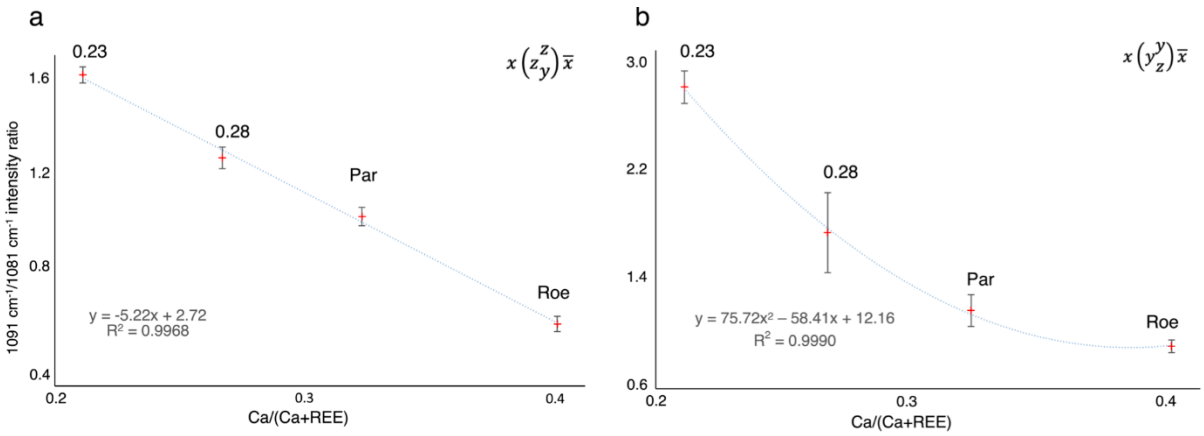

Figure 3.16. 1091 cm^{-1}/1081 cm^{-1} intensity ratio for röntgenite (Roe), parisite (Par) and B_2S for **E** // z (a) and **E** ⊥ z (b).

3.4.2 Polysome detectability through electron-beam related techniques

Although nanoscale disorder can be overlooked, SEM-EDS is the fastest technique for polysomes identification. TEM-EDS, while time-consuming and providing only local information, remains the ultimate technique for polysome identification. Since most high resolution TEMs have a limited tilt range, the sample needs to be pre-oriented before preparation; in this case EBSD can be very useful. EBSD can easily distinguish CRFC among other phases and correctly provides their orientation relationship, but under routine application, fails to distinguish among different polysomes.

At the TEM scale, in addition to basic CRFC, intermediate polysomes not fully described in the literature have been identified. These include, a B_2S polysome, a 32 nm and a 23 nm long range polysomes, and a new parisite polytype with a double *c* parameter compared to normal parisite. Further investigations are required for a full characterization of all these new structures.

3.4.3 Implications for REE ore formation

In principle, under equilibrium crystallization conditions, any fluid composition falling within the bastnäsite-synchysite series can be accommodated by an appropriate proportion of *B* and *S* layers. This situation contrasts with the simultaneous crystallization of two similar phases of different composition, as seen in any system with a miscibility gap, such as the well-known case of alkali feldspar system at high pressure (e.g. Winter, 2001).

The inability of the system $CeFCO_3$–$CaCO_3$ to form solid solutions is considered a factor

explaining the presence of syntactic intergrowths in CRFC (Donnay and Donnay, 1953). One crystal precipitates until the conditions in the solution change sufficiently for the next compound to separate out, which then crystallizes on the original crystal. Since the two species alternate, periodic and discontinuous changes in the conditions of the system must be postulated. Variations in the $a\mathrm{Ca}^{2+}$, $a\mathrm{REE}^{3+}$, $a(\mathrm{CO_3})^{2-}$, $a\mathrm{F}^{-}$, and temperature of the solution may well be the controlling factors during crystal growth (Gysi and Williams-Jones, 2015).

Bastnäsite-(Ce) and synchysite-(Ce) both occur at Mount Malosa (Malawi), but in separate samples, i.e. they are never observed in contact. Moreover, their chemical composition is remarkably different in terms of REE partitioning: synchysite is richer in Y (and poorer in Ce, La and Nd) than bastnäsite and all other intermediate terms (Table 3.1 and 3.2). This could indicate that synchysite formed under different physicochemical conditions than the other polysomes.

The most recurrent microstructure in Mount Malosa CRFC is represented by rhythmic parisite-bastnäsite intergrowths, along with a number of more or less ordered intermediate polysomes. This microstructure is similar to that of the Olympic Dam deposit in Australia (Ciobanu et al., 2022), but a clear trend of compositions varying gradually from a basic polysome to the next through disordered domains has not been observed at Mount Malosa. The observed microstructure suggests a primary growth mechanism in which CRFC crystallize from a fluid close to thermodynamic equilibrium, whose conditions quickly and repeatedly crossed the parisite–bastnäsite stability boundary, rather than a stepwise approach toward thermodynamic equilibrium.

According to Secco et al. (2007), the crystallization of CRFC at Mount Malosa occurred at ~1 kbar and 300–400 °C. These conditions are fully consistent with the mineral–fluid stability diagrams for the Ca–REE–C–O–H–F system provided by Gysi and Williams-Jones (2015). Their diagrams show that the boundary between parisite and bastnäsite, which has a negative slope on the $\log a\mathrm{F}^{-}$ vs. $\log a(\mathrm{CO_3})^{2-}$ diagram, can be easily crossed after small variations in either $a(\mathrm{CO_3})^{2-}$ or $a\mathrm{F}^{-}$. Therefore, these variations are likely the primary reasons for departures from equilibrium conditions. It should be noted, however, how an increase in $a(\mathrm{CO_3})^{2-}$ (or $a\mathrm{F}^{-}$, or both) in the fluid would cause the crystallization of parisite at the expenses of bastnäsite (Fig. 3.17). However, the protracting of this situation, would result in an increase in $a\mathrm{REE}^{3+}$ in the remaining fluid, thus creating conditions favourable for the crystallization of bastnäsite (or other polysomes with lower Ca content than parisite). In other words, the crystallization process itself may induce rhythmic changes in fluid composition at the crystallization front, leading to syntactic intergrowths. Consequently, these intergrowths appear to be an inevitable feature of CRFC.

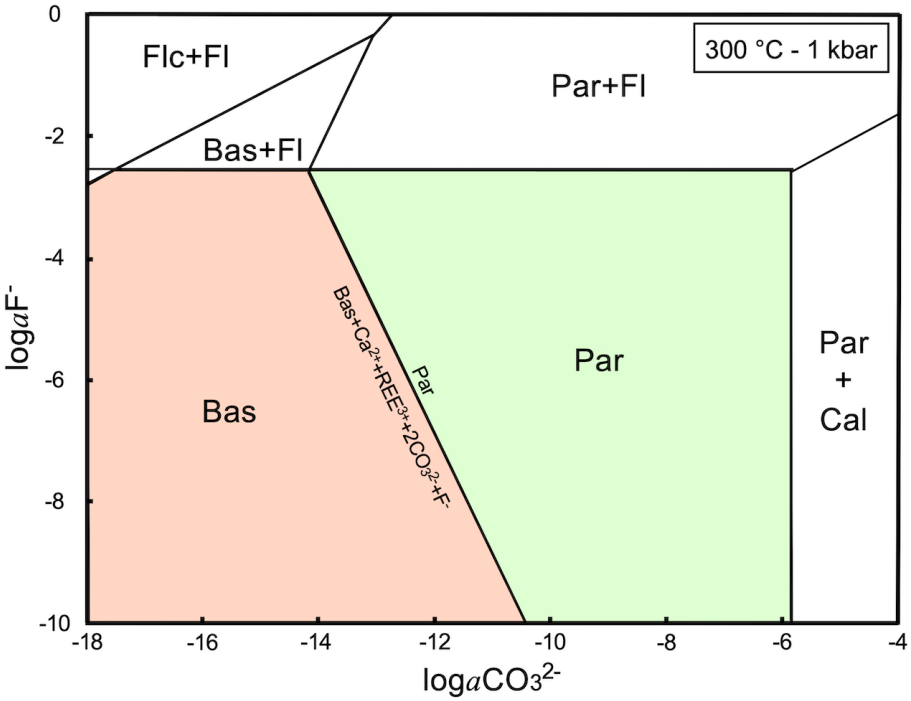

Figure 3.17. Calculated mineral–fluid equilibria at 300 and 1 kbar for the stability of bastnäsite-(Ce) and parisite-(Ce) as a function of aF^{-} and aCO_3^{2-} (modified after Gysi and Williams-Jones, 2015).

Chapter 4

Unveiling the complexity of (Ca-REE) fluorcarbonates from Cuasso al Monte (Italy): A variety of morphologies, microstructures and compositions, with implications on REE mobility

4.1. Introduction

Despite the importance of REE, a lot of unanswered questions about the mechanisms that govern their transport and deposition in natural systems survive. The main reasons are the difficulty of reproducing in laboratory the complex natural conditions in which they occur and that of separating different REE, due to their similar geochemical behaviour. The understanding of such mechanisms may reveal important, not only for the geological exploration and the beneficiation of metallurgical processes, but also for the recycling of REE, which now is under 1%, mainly because actual methods are expensive, energy-consuming and inefficient (Balaram, 2019; Peiravi et al., 2020). Particularly, the study of polysomatism may reveal important since the intergrowths of different polysomes may indicate changes in the crystallization conditions or fluid composition (Gysi and Williams-Jones, 2015). In this context, a variety of CRFC with differing morphologies and compositions, from Cuasso al Monte (Western Southern Alps – Italy), have been studied for the first time: i) synchysite-(Ce) forming hexagonal prisms and rosette-like aggregates; ii) bastnäsite-(Ce) forming blocky aggregates; iii) bastnäsite-(Nd) forming desert rose-like intergrowths and iv) combinations of synchysite-(Ce) and bastnäsite-(Nd) forming more complex micro and nanostructures. These minerals are retained to form from a hydrothermal fluid in a temperature range between 350 and 100 °C. After an investigation spanning from the microscale to the atomic scale, which employed optical stereomicroscopy, SEM and TEM, microanalysis and Raman spectroscopy, a possible scenario for their formation has been depicted. It assumes that the different CRFC crystallized in sequences under decreasing temperature and fluid fractionation, with synchysite-(Ce) being the first to form, followed by bastnäsite-(Ce) and finally bastnäsite-(Nd). The different morphologies, in this case, other than being induced by the dominant REE in the fluid, were also due to varying temperatures and cooling rates.
This study highlights that nature may efficiently separate REE from one another, like Y from La, Ce and Nd; Ce from Nd and La; and Th. Thorium a radioactive and toxic element, seems to enter the structure of CRFC during the final stages of crystallization. The understanding of these natural processes may suggest routes for improving current metallurgical separation processes.

This chapter, with modification, is currently under review as: "*Conconi, R., Gentile, P., Fumagalli, P., Nieto, F., Capitani, G., 2024b. CaREE-fluorcarbonates: A variety of morphologies, compositions and nanostructures with insights into REE partitioning and mobility. Lithos"*

4.2. Geological setting

Cuasso al Monte is located in the Western Southern Alps (Fig. 4.1). This region is renowned for the extraction of "Red Porphyry", a granophyre dimension stone, which is quarried since 1880 (Fagnani, 1946) and very appreciated mainly in the building industries for its reddish/pinkish colour and hardness. The genesis of this rock is associated with the post-Hercynian calc-alkaline magmatism that generated the "Graniti dei Laghi": felsic plutons which intruded the amphibolites and the ortho- and paragneisses of the "Serie dei Laghi" unit (Boriani et al., 1988; Bakos et al., 1990; Pinarelli et al., 1993). The granophyre represents a

subvolcanic complex formed during crustal extension that was triggered by a post-orogenic regime. During this event, a mantle derived magma formed chambers at lower depth and got crustal contaminated (Bakos et al., 1990; Pinarelli et al., 2002).

The Red Porphyry shows a medium grain size and is mainly composed of K-feldspar, quartz, albite and biotite. A notable characteristic of this rock is the abundant presence of miarolitic cavities, which were filled with secondary minerals by the circulation of late hydrothermal fluids (Pezzotta et al., 1999). Hydrothermal activity was responsible for both the crystallization of tens of different mineral species (Pezzotta et al., 1999, 2005; Demartin et al., 2001; Vignola et al., 2012; Capitani et al., 2018), and the alteration of the rock forming minerals (such as the alteration of K-feldspar and the chloritization of biotite). The CRFC studied here come from these miarolitic cavities, which also host feldspar, quartz, fluorite, chamosite, sphalerite, anatase, aeschynite and zircon (Capitani et al., 2018).

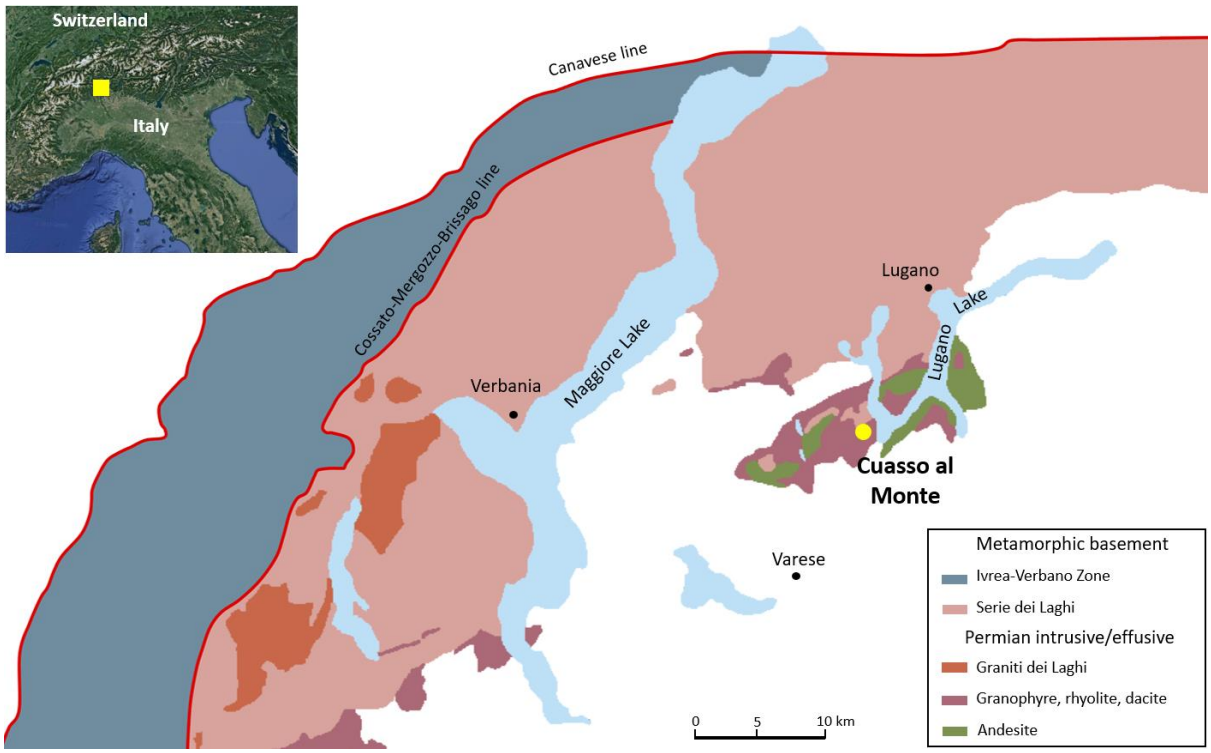

Figure 4.1. Geological sketch map of the Hercynian plutonic and volcanic rocks in the Western Southern Alps. Yellow dots indicate the locality where the CRFC were collected (modified after Capitani et al. 2018).

4.3. Samples description

The CRFC occur in three different morphologies: i) rosette-like aggregates, which are formed by hexagonal lamellae (Fig. 4.2A, B); ii) hexagonal prisms aggregates (Fig. 4.2C, D); and iii) blocky subhedral aggregates (Fig. 4.2E, F). Crystal aggregates are generally less than 400 µm, whereas single prisms are less than 100 µm in diameter. All aggregates show a yellowish to reddish colour, but hexagonal prisms, which may occur either as singlets or aggregates, are frequently zoned, with a light red rim and a dark red core. The CRFC can be found on K-feldspar, chamosite, fluorite and quartz; less frequently included in quartz and fluorite.

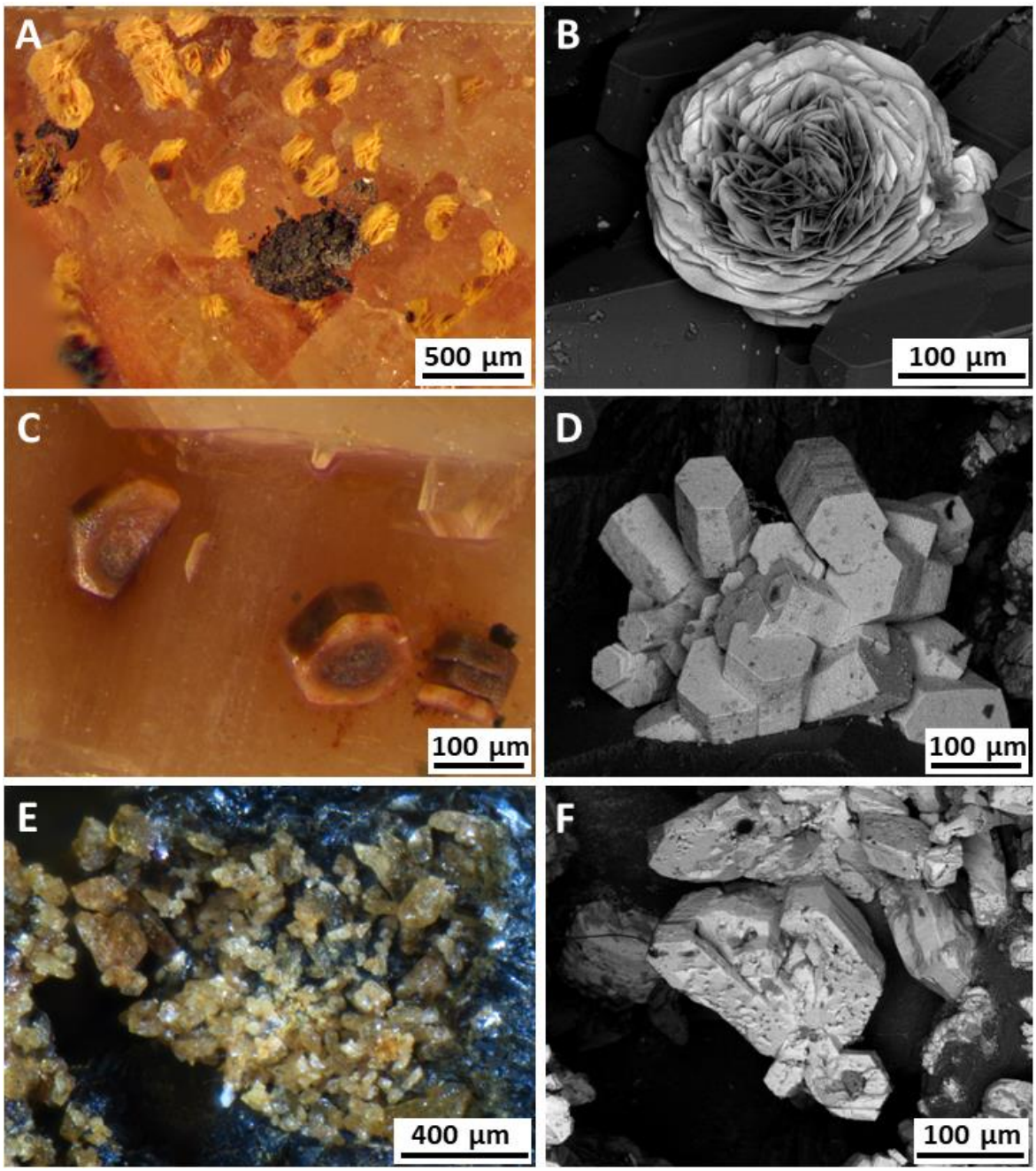

Figure 4.2. Optical micrographs and SEM (SE) images showing (A, B) rosette-like, (C, D) hexagonal prisms and (E, F) blocky subhedral aggregates of CRFC.

4.4. Results

4.4.1 Hexagonal prisms aggregates: synchysite-(Ce)

Raman spectroscopy and SEM-EDS both identify the hexagonal prisms aggregates as synchysite-(Ce). SEM-BSE images show a core-rim zoning, consistently with optical observations (Fig. 4.3). EDS analyses show an average Ca/(Ca+REE) ratio close to 0.50, clearly indicating synchysite-(Ce) (Table 4.1). EDS maps reveal that the zoning concerns the distribution of Ce, La, Nd, Y and Th, with the rim enriched in Y and the outer rim in Th and both depleted in Ce, La and Nd compared to the core (Fig. 4.3). Gd, Pr and Sm do not vary

significantly from core to rim. Micro-inclusions of Fe-oxides and thorite were detected in the rim. Raman spectra show the typical vibrational modes of the carbonate group (CO_3^{2-}): the symmetric stretching [$v_1(CO_3)$], the antisymmetric stretching [$v_3(CO_3)$] and the in-plane bending [$v_4(CO_3)$] vibrations were observed at 1080-1100 cm^{-1}, ~1440 cm^{-1} and 730-770 cm^{-1}, respectively. The symmetric stretching vibration [$v_1(CO_3^{2-})$] shows the characteristic double splitting typical of synchysite (Fig. 4.4) with bands at 1082 and 1098 cm^{-1}, in agreement with Chapter 3 (Conconi et al., 2023a).

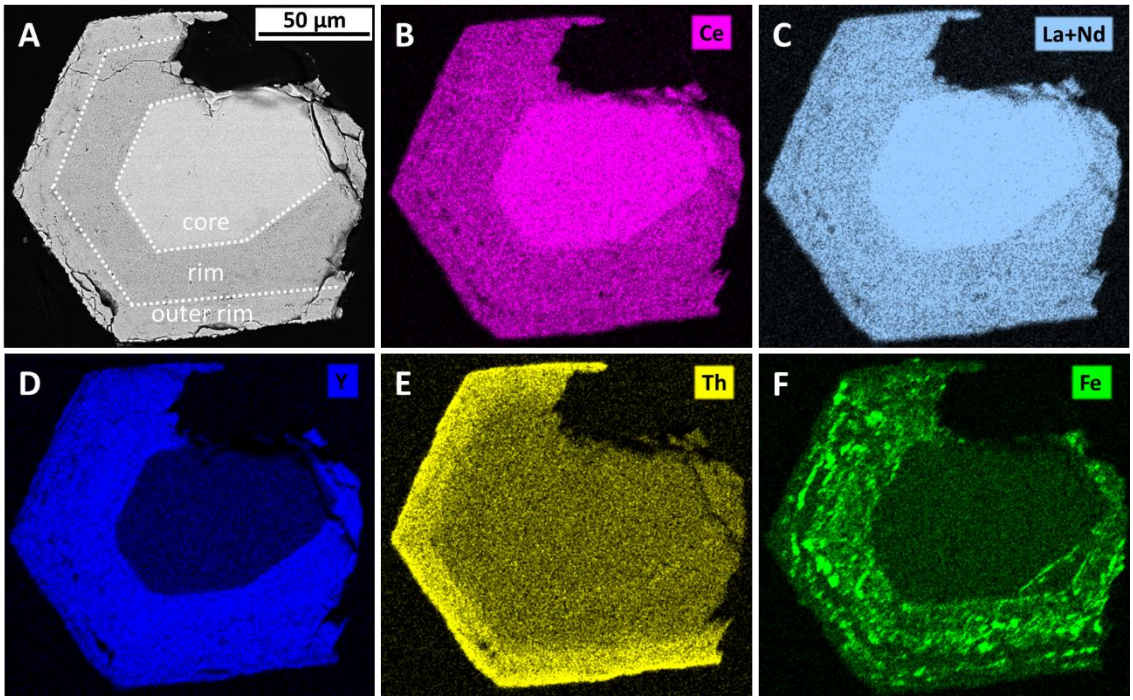

Figure 4.3. A) BSE image showing the zonation of an hexagonal prism of synchysite-(Ce). B, C, D, E and F) EDS maps showing the partitioning of Ce, La, Nd, Y, Th and Fe.

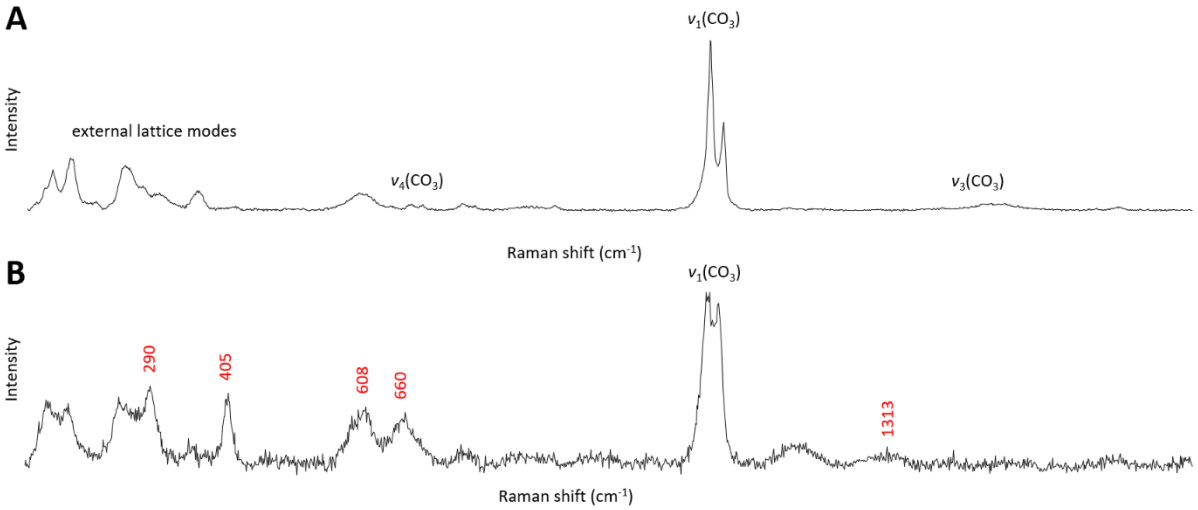

Figure 4.4. Raman spectra collected at the centre (A) and at the rim (B) of the crystal. In both cases the characteristic double splitting of the $v_1(CO_3^{2-})$ symmetric stretching vibration of synchysite is visible. Moreover, the spectrum collected at the rim shows bands assigned to hematite (in red), a higher background and broadening of the $v_1(CO_3^{2-})$ symmetric stretching vibration (c). The latter suggests a loss of crystallinity at the rim due to metamictic damage caused by α-decay of Th (see Chapter 5 for more details).

4.4.2 Subhedral blocky aggregates: bastnäsite-(Ce)

SEM-EDS analyses of subhedral blocky aggregates do not reveal any zoning and/or intergrowths with other phases (Fig. 4.5A). The Ca/(Ca+REE) ratio and the REE sum are 0.01 and 0.98 respectively, with Ce the dominant REE, suggesting bastnäsite-(Ce) (Table 4.1). Other major REE are La and Nd, whereas Sm, Pr, Gd and Y are present as minor components.
The Raman analysis shows the v_1, v_3 and v_4 vibrational modes of the carbonate group and the $v_1(CO_3)$ symmetric stretching vibration centred at 1095 cm^{-1}, as for bastnäsite-(Ce) (see Chapter 3) (Fig. 4.5B), therefore confirming the SEM-EDS results.

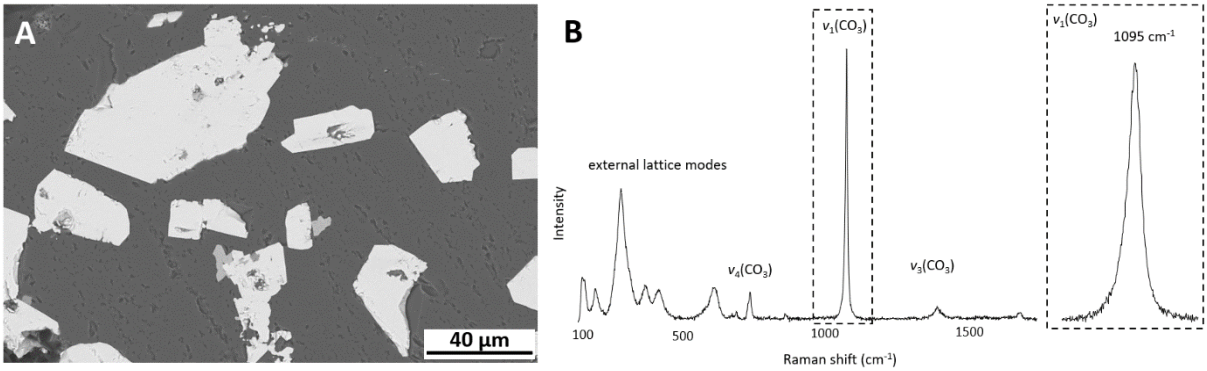

Figure 4.5. (A) BSE image of subhedral blocky bastnäsite-(Ce) (light grey) and (B) related Raman spectrum showing the characteristic single band of the $v_1(CO_3)$ symmetric stretching vibration.

4.4.3 Rosette-like aggregates: synchysite-(Ce) and bastnäsite-(Nd)

Raman spectroscopy and quantitative EDS analysis reveal that rosette-like CRFC actually consist of two different species: synchysite-(Ce) and bastnäsite-(Nd). However, the analysis highlights complex microstructures, which were deeply studied by TEM.

Synchysite-(Ce) forms thick, flat and solid lamellae (Fig. 4.6A, B) and shows different microstructures: i) a minimal porosity concentrated along the rims (Fig. 4.6C), which sometimes are depleted in Ca and Ce and enriched in Si and Al with respect to the core; ii) a chemical zoning with Y-depleted regions in the centre of the lamellae and Th-, Y-enriched tips, somehow resembling the chemical zoning of hexagonal prism synchysite-(Ce) described above (Fig. 4.6D) and iii) a porous rim enriched in Th, Nd, La, Si and Al and depleted in Ce and Ca (Fig. 4.6E, F). Quantitative EDS analysis of synchysite-(Ce) (Table 4.1) shows a Ca/(Ca+REE) ratio of ~0.50, clearly indicating synchysite. Moreover, the samples contain Ce, Y, La and Nd as major REE, whereas Sm, Pr and Gd are present as minor components. As for the synchysite-(Ce) hexagonal prisms, Raman spectra show the characteristic double splitting of the symmetric stretching vibration [$v_1(CO_3^{2-})$], with two bands at 1082 and 1100 cm^{-1}.
TEM-EDS analysis shows that synchysite-(Ce) has a nanostructure where rosette-like "petals" are single crystals (Fig. 4.7A, B) with the shortest dimension parallel to **c***, the stacking direction of CaF-, Ce- and (CO_3)-layers. Each petal can therefore be assimilated to a stubby prism. TEM-EDS analyses (Table 4.1) reveal a Ca/(Ca+REE) ratio and Ca content of 0.50 and 0.99 a.p.f.u, respectively, which is in agreement with the ideal composition of synchysite. SAED patterns and lattice fringes images reveal the presence of polysomatic and polytypic disorder (Fig. 4.7C, D).

Finally, the porous rim bordering synchysite-(Ce) observed by SEM (Fig. 4.6E, F) consists of bastnäsite-(Nd) nanorods, particularly enriched in Th (2.10-4.01 at%) (Fig. 4.7 E, F). These show a surprisingly high Ca content (up to 0.16 a.p.f.u; Table 4.1), which at a first instance may be due to secondary fluorescence of surrounding synchysite, but the possibility that, at least in part, it could be in solid solution with REE cannot be entirely excluded (see ahead).

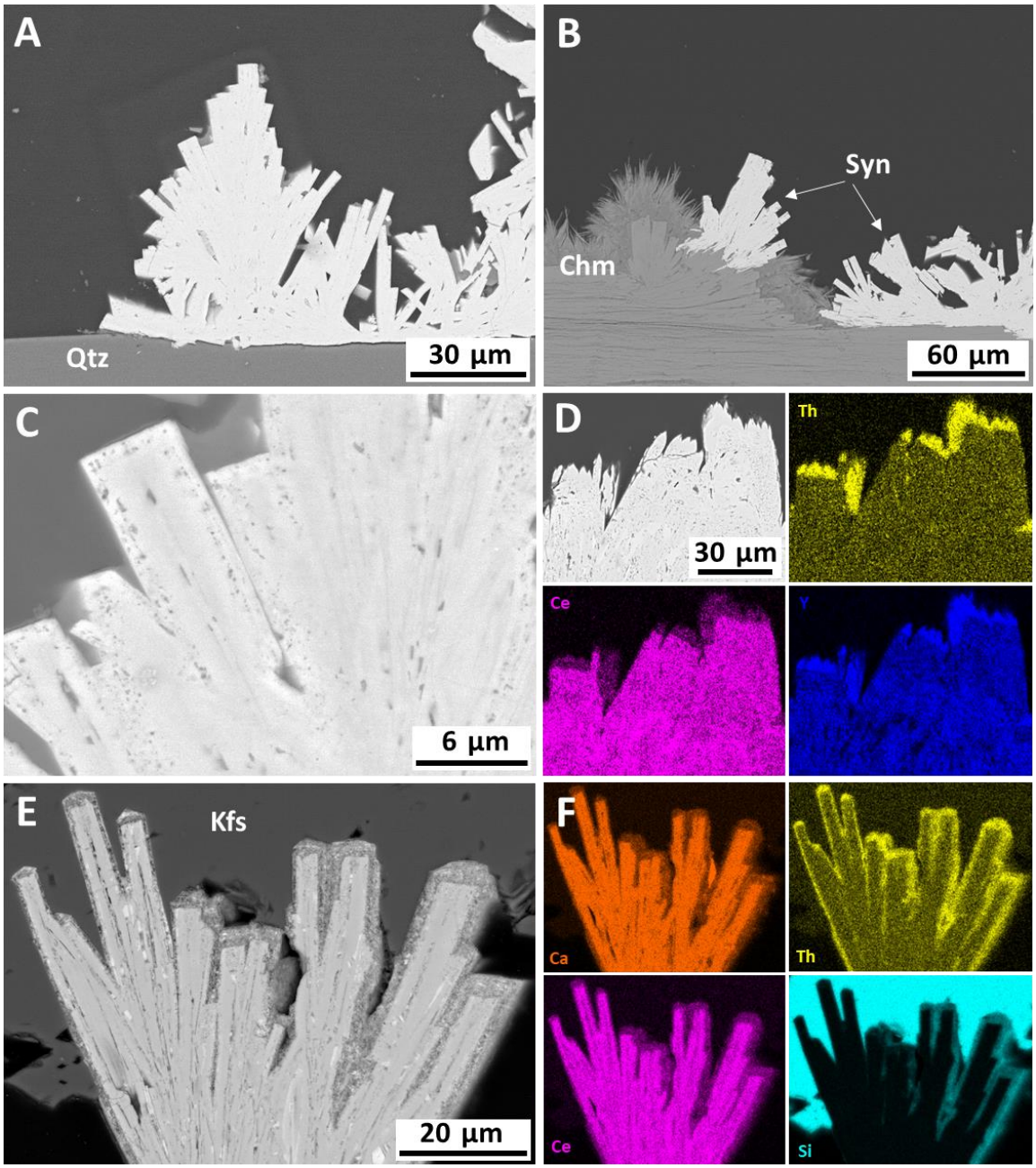

Figure 4.6. Backscattered-SEM images showing: (A, B) thick, flat and solid lamellae of synchysite-(Ce) (Syn) on quartz (Qtz) and on two different generations of chamosite (Chm); (C) enlargement of A showing the porosity concentrated on the rim of the lamellae; (D) EDS maps showing the Y poor regions and the enrichment in Th and Y at the tips of the lamellae; (E) synchysite-(Ce) framed by a porous rim on K-feldspar (Kfs); (F) EDS map of E showing the enrichment in Th and Si and the depletion in Ca and Ce in the porous rim. Darker grey in all BSE images is the epoxy resin.

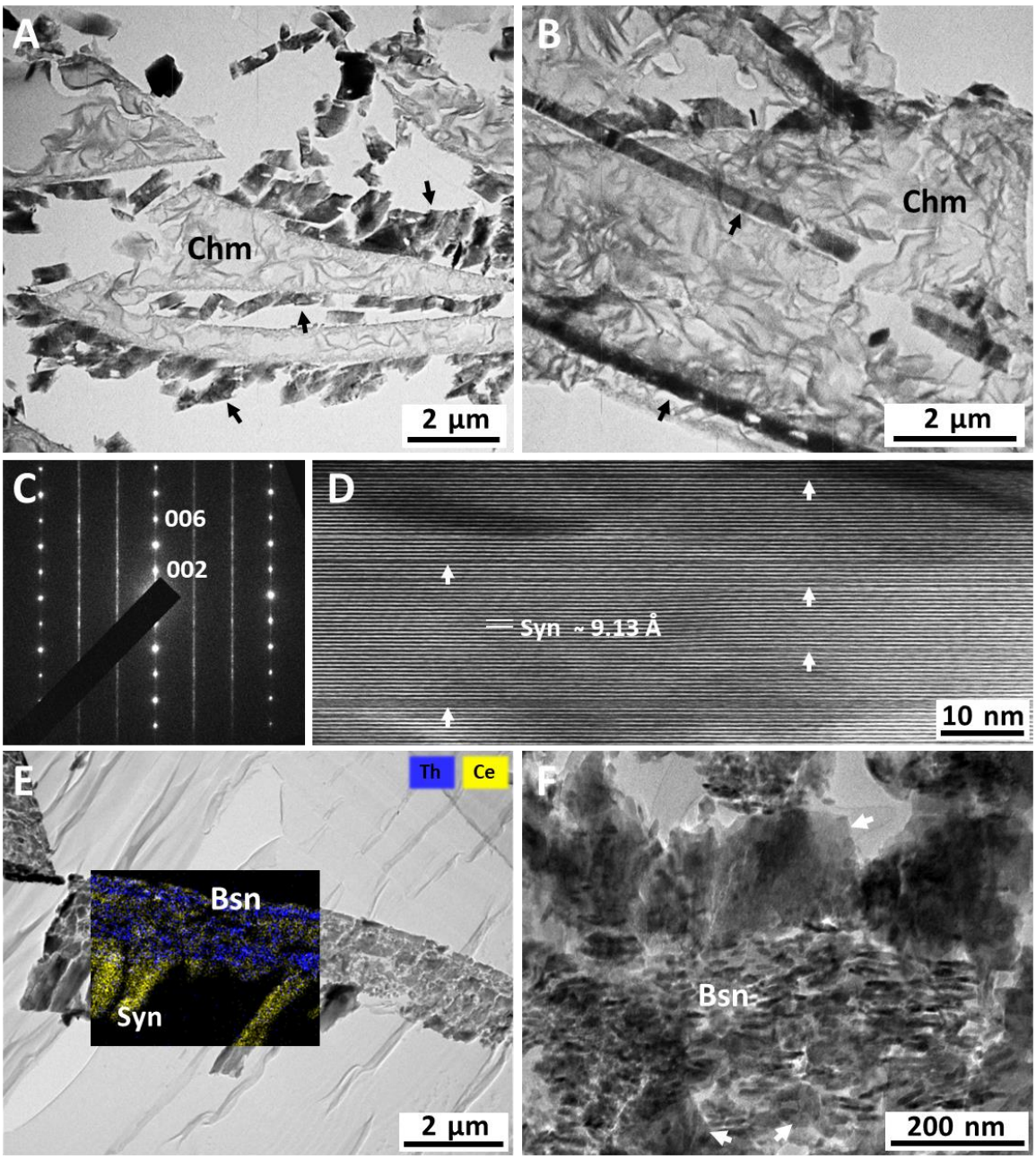

Figure 4.7. (A, B) Bright field TEM images of synchysite-(Ce) lamellae (black arrows) with chamosite (Chm). C) SAED pattern of synchysite-(Ce) along [110] showing polytypic and polysomatic disorder. (D) High resolution TEM image showing Ca-poor polysomatic faults (white arrows) within synchysite-(Ce) (Syn). (E) Bright field TEM image showing the porous rim of synchysite-(Ce) with superimposed EDS map showing the enrichment in Th. (F) Enlargement of E showing the presence of bastnäsite-(Nd) nanocrystals and synchysite-(Ce) (white arrows).

Bastnäsite-(Nd), in comparison with synchysite-(Ce), forms thinner and slightly bent lamellae with a widespread porosity (Fig 4.8). The SEM-EDS analysis reveals a composition different from that of any other polysome of the bastnäsite-synchysite series described so far (Table 4.1). The Ca/(Ca+REE) ratio varies between 0.09 and 0.15, which are close to the Ca/(Ca+REE) ratio of the B_6S and B_5S polysomes, 0.12 and 0.14, respectively. A peculiar characteristic of this phase is that Nd is the dominant REE, followed by La and Ce. Besides, Si, Al and Fe are almost

always present, suggesting additional phases intergrown with the CRFC at a scale not resolvable with SEM-EDS.

Raman spectra show the presence of a single symmetric stretching vibration $v_1(CO_3^{2-})$, typical of bastnäsite (Fig. 4.8E). However, in the bastnäsite-(Ce) described in Chapter 3 (Conconi et al., 2023a), this band is centred at 1095 cm^{-1}, while here it is observed at 1098 cm^{-1}. This Raman shift may derive from the different compositions of the compared bastnäsites. Indeed, the lanthanide contraction causes Nd to have a smaller ionic radius than Ce, forming possibly stronger bonds and consequently a positive Raman shift. Finally, the Raman spectra show intense bands between 220 and 660 cm^{-1} and at 1313 cm^{-1} that can be assigned to hematite (Kuebler et al., 2006). Consequently, intergrowths of, at least, hematite and CRFC can be inferred. At this stage, the origin of Si and Al detected by EDS remains unexplained, as well as if the observed Ca/(Ca+REE) ratio reflects ordered polysomes (B_6S or B_5S) or arises from disordered intergrowths of Ca-rich lamellae and bastnäsite.

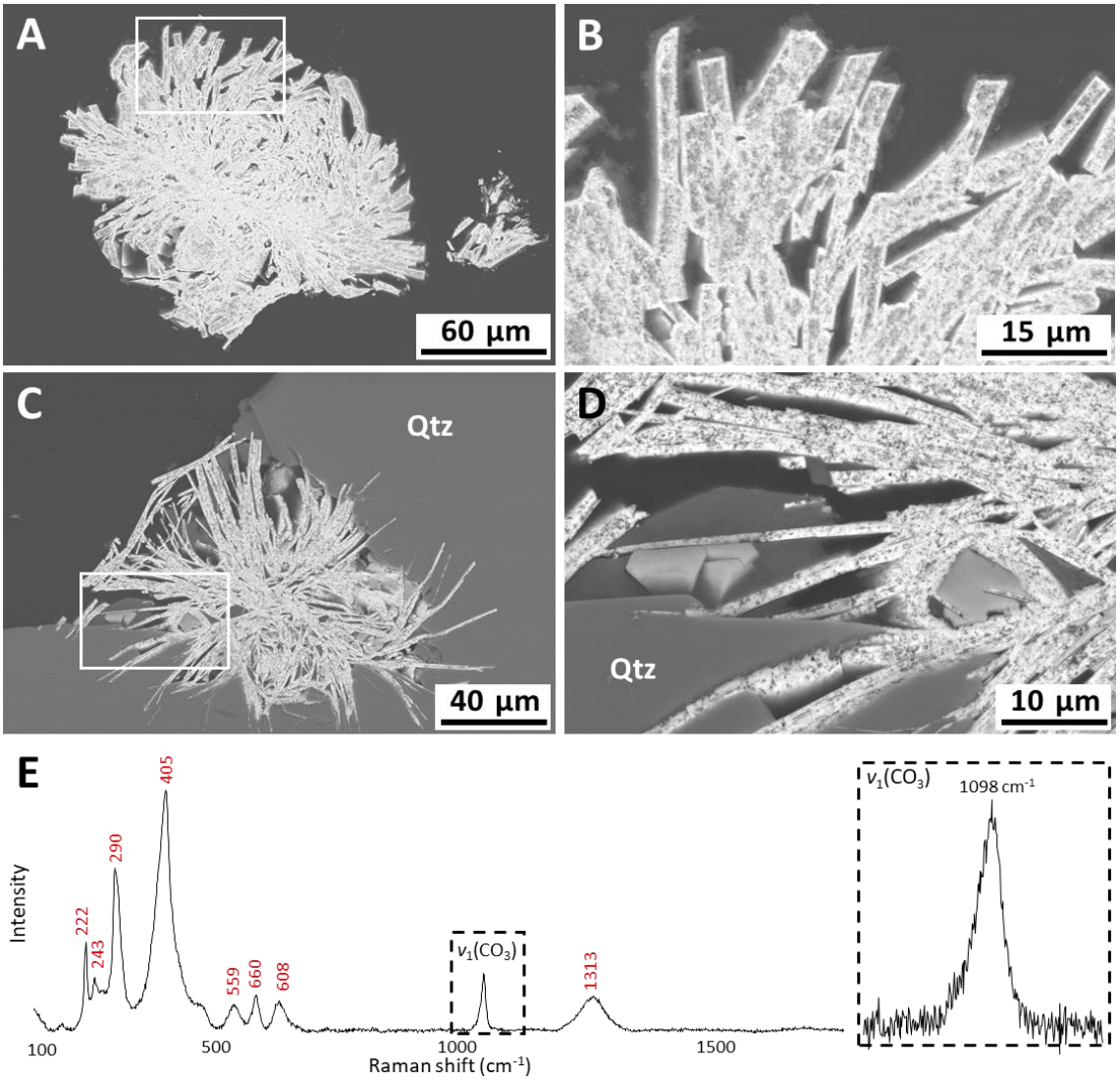

Figure 4.8. Backscattered-SEM images showing the microstructure of rosette-like bastnäsite-(Nd) (A, C) and their enlargement showing the porous microstructure (B, D). E) Raman spectrum of bastnäsite-(Nd), in which the symmetric stretching vibration (v_1) presents a band at 1098 cm^{-1}. Moreover, bands belonging to hematite (in red) are present.

At the TEM scale, bastnäsite-(Nd) shows a complex nanostructure recalling the gypsum or calcite "desert rose" (although at smaller scale), made of an intergrowth of bastnäsite and hematite nanocrystals, together with phyllosilicates, including kaolinite-like and undefined other phases (Fig. 4.9A, B). The bastnäsite-(Nd) forms nanorods generally less than 50 nm in length (Fig. 4.9C). Hematite was observed both as nanorods up to 200 nm in length and as irregular nanoparticles; generally, they are dispersed within bastnäsite, but sometimes form clusters. Phyllosilicates are present either along the rim of the rosette-like "petals" or within interstices left by bastnäsite-hematite intergrowths. Overall, this intergrown constitutes the porosity observed by SEM.
TEM-EDS analyses of bastnäsite nanocrystals show a Ca/(Ca+REE) ratio of 0.08 and a REE sum of 1.00 a.p.f.u (Table 4.1). No presence of Si, Al and Fe were detected as, instead, was observed in SEM-EDS, suggesting that Si and Al and part of the Fe are present in phyllosilicates, and most of the Fe in hematite. Sometimes, bastnäsite-(Nd) shows a "scaffold" nanostructure made of a core of bastnäsite-(Nd) nanocrystals walled by solid synchysite-(Ce), in turn surrounded by phyllosilicates (Fig. 4.9D).
Overall, lattice fringe images and the diffraction patterns of the bastnäsite-(Nd) show an ordered structure with constant (002) spacing of ~4.9 Å (Fig. 4.9E, F), i.e. it is not possible to ascertain the presence of Ca-bearing lamellae such as synchysite (~9.1 Å) or parisite (~14.0 Å) (in all these phases the (001) lattice fringes are forbidden by symmetry, *P*-62*c*, *Cc* and *C*2/*c*, respectively, so that only halved periodicity is observed in HR images). Therefore, we cannot but conclude that Ca, at least in nanocrystals, can enter the bastnäsite-(Nd) structure in solid solution with REE up to 0.08 a.p.f.u.

TEM-EDS analyses of phyllosilicates revealed the presence of at least three different species: an amorphous kaolinite-like phase and two other undefined phases (Table 4.2). The former shows Al and Si in almost 1:1 ratio, like kaolinite, and the corresponding SAED patterns is typical of amorphous material (Fig. 4.10). Instead, the two undefined phases have a Si/Fe ratio of almost 4:1 and 1:1, respectively. Other elements such as Na, K, Mg, Al and Ca are present in minor amounts. The crystal morphology unmistakably resembles phyllosilicate group minerals, and the measured lattice fringe spacing of either 14 or 16 Å may suggest chlorite- or smectite-like phases. However, SAED patterns and compositions do not unambiguously match any known phyllosilicate (Fig. 4.11). These phases may represent metastable clay precursors similar to those described by Tazaki (2005).

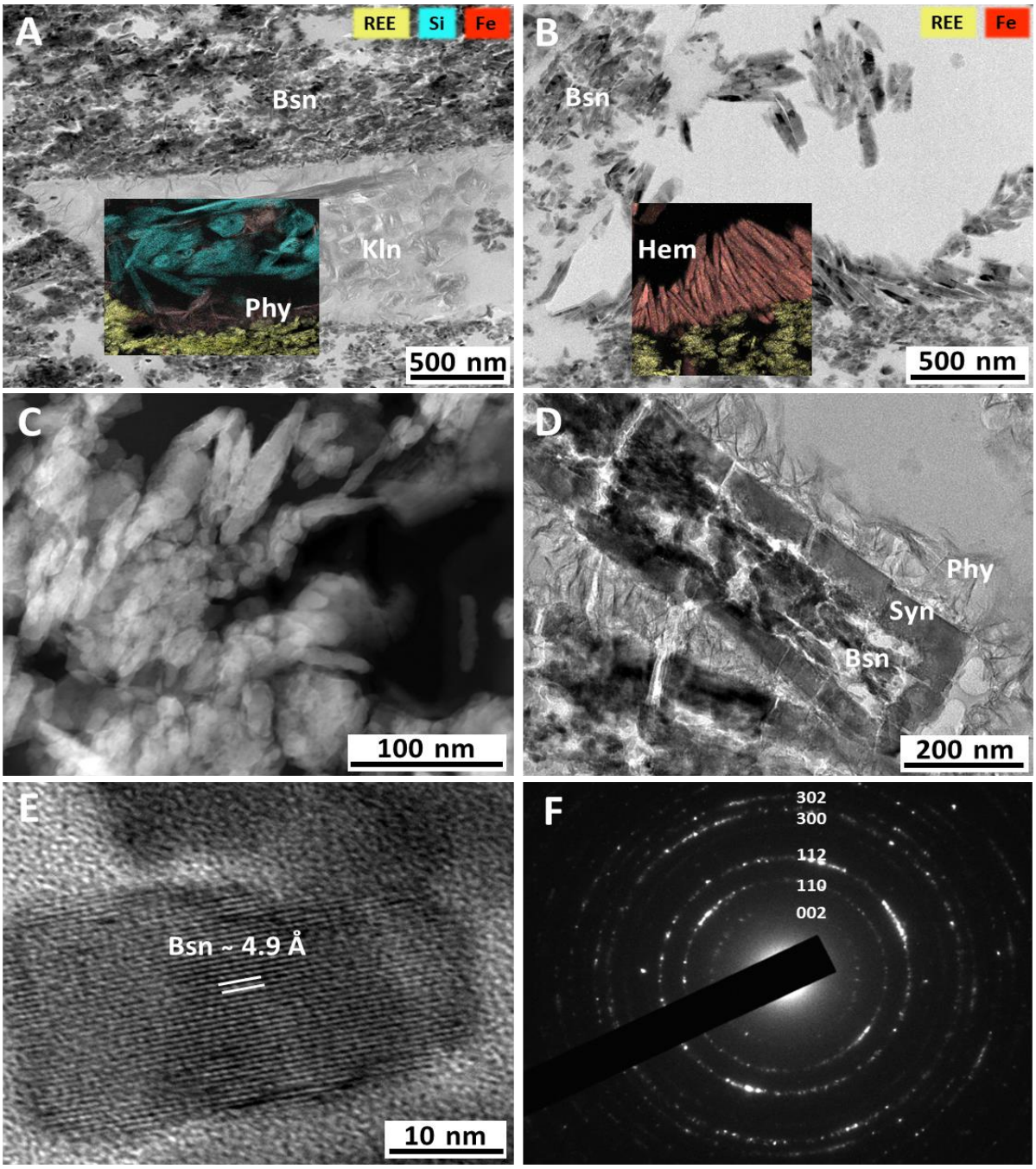

Figure 4.9. (A, B) Bright field TEM images with superimposed TEM-EDS maps showing the nanostructure of bastnäsite-(Nd) in which bastnäsite nanocrystals (Bsn) are intergrown with phyllosilicates (Phy), kaolinite-like (Kln) and hematite (Hem); C) HAADF STEM image showing the spindle shape of bastnäsite nanocrystals. D) "scaffold" nanostructure with bastnäsite nanocrystals walled by synchysite-(Ce) (Syn) and phyllosilicates (Phy). E) Lattice fringe image of bastnäsite-(Nd) showing a constant ~4.9 Å spacing. F) SAED patterns of bastnäsite nanocrystals showing the typical diffraction rings of polycrystalline materials (main rings indexed).

Table 4.1. SEM- and TEM-EDS analyses (a.p.f.u.) of synchysite (Syn) and bastnäsite (Bsn). Number of analyses and standard deviation in square and round brackets, respectively. Standard deviation in italics when larger than the attached values, meaning that most of the averaged values are below the detection limit (*b.d.l.*) whereas some have relatively high values. The a.p.f.u. were recalculated on the basis of one cation for bastnäsite and two cations for synchysite.

	SEM-EDS									TEM-EDS			
	Hexagonal prism			Blocky	Rosette like aggregates								
	Syn-(Ce) core [13]	Syn-(Ce) rim [15]	Syn-(Ce) out-rim [15]	Bsn-(Ce) [13]	Syn-(Ce) [21]	Syn-Y-poor [5]	Th-rich tips [4]	Porous rim [9]	Bsn-(Nd) [20]	Syn-(Ce) [27]	Syn-Y-poor [4]	Bsn-[Nd] [12]	Porous rim [11]
F	0.349 (0.062)	0.591 (0.130)	0.567 (0.166)	0.801 (0.033)	0.631 (0.196)	0.755 (0.038)	0.891 (0.309)	0.987 (0.161)	0.766 (0.196)	1.007 (0.147)	0.920 (0.070)	1.249 (0.139)	1.186 (0.170)
Ca	1.060 (0.008)	1.097 (0.029)	1.100 (0.018)	0.012 (0.004)	1.051 (0.028)	1.024 (0.049)	1.125 (0.109)	0.937 (0.022)	0.138 (0.028)	0.989 (0.064)	0.914 (0.035)	0.086 (0.007)	0.212 (0.040)
Y	0.036 (0.014)	0.231 (0.029)	0.203 (0.021)	0.020 (0.009)	0.185 (0.034)	0.036 (0.013)	0.364 (0.080)	0.114 (0.016)	0.095 (0.034)	0.143 (0.055)	0.041 (0.044)	0.114 (0.014)	0.035 (0.012)
La	0.108 (0.007)	0.091 (0.016)	0.067 (0.004)	0.179 (0.022)	0.148 (0.012)	0.246 (0.013)	0.128 (0.027)	0.226 (0.013)	0.209 (0.012)	0.189 (0.032)	0.252 (0.022)	0.233 (0.022)	0.245 (0.037)
Ce	0.413 (0.011)	0.294 (0.023)	0.277 (0.012)	0.506 (0.016)	0.363 (0.023)	0.504 (0.020)	0.080 (0.012)	0.236 (0.025)	0.150 (0.023)	0.396 (0.067)	0.548 (0.034)	0.214 (0.016)	0.135 (0.073)
Nd	0.244 (0.005)	0.157 (0.007)	0.153 (0.005)	0.178 (0.014)	0.149 (0.017)	0.129 (0.008)	0.042 (0.014)	0.205 (0.012)	0.243 (0.017)	0.189 (0.032)	0.171 (0.013)	0.263 (0.022)	0.204 (0.023)
Th	0.005 (0.003)	0.013 (0.006)	0.087 (0.016)	0.015 (0.002)	*0.004 (0.006)*	*b.d.l*	0.175 (0.018)	0.166 (0.022)	0.044 (0.006)	*0.016 (0.032)*	*b.d.l*	0.034 (0.006)	0.140 (0.042)
Pr	0.068 (0.003)	0.041 (0.002)	0.041 (0.004)	0.052 (0.004)	0.040 (0.003)	0.051 (0.002)	0.015 (0.007)	0.052 (0.005)	0.042 (0.003)	0.025 (0.022)	*0.019 (0.032)*	0.060 (0.007)	0.053 (0.018)
Sm	0.042 (0.004)	0.036 (0.005)	0.037 (0.003)	0.021 (0.004)	0.028 (0.006)	0.005 (0.003)	0.032 (0.008)	0.044 (0.012)	0.049 (0.006)	0.026 (0.019)	*b.d.l*	0.046 (0.015)	0.031 (0.007)
Gd	0.024 (0.05)	0.039 (0.004)	0.035 (0.003)	0.013 (0.003)	0.027 (0.007)	0.005 (0.002)	0.039 (0.007)	0.019 (0.010)	0.030 (0.007)	0.020 (0.015)	*b.d.l*	0.039 (0.008)	*0.008 (0.009)*
Σ REE	0.940 (0.008)	0.903 (0.029)	0.900 (0.018)	0.983 (0.006)	0.943 (0.030)	0.976 (0.049)	0.875 (0.109)	1.063 (0.022)	0.862 (0.030)	0.985 (0.049)	1.031 (0.039)	1.005 (0.053)	0.851 (0.043)
Ca/(Ca+REE)	0.530 (0.004)	0.549 (0.014)	0.550 (0.009)	0.012 (0.004)	0.527 (0.013)	0.512 (0.025)	0.562 (0.054)	0.468 (0.011)	0.138 (0.013)	0.501 (0.020)	0.470 (0.018)	0.079 (0.008)	0.199 (0.030)

Table 4.2. TEM-EDS analysis (At%) of phyllosilicates intergrown with bastnäsite-(Nd) nanocrystals: kaolinite and two undefined phases. Number of analyses in round brackets

El	Kaolinite phase (12)	Undefined I (20)	Undefined II (10)
O	63.69	63.37	60.01
Na		0.06	0.35
Mg		0.96	0.07
Al	17.89	4.65	2.34
Si	18.43	24.45	19.06
K		0.03	0.08
Ca		0.03	0.26
Fe		6.46	17.84

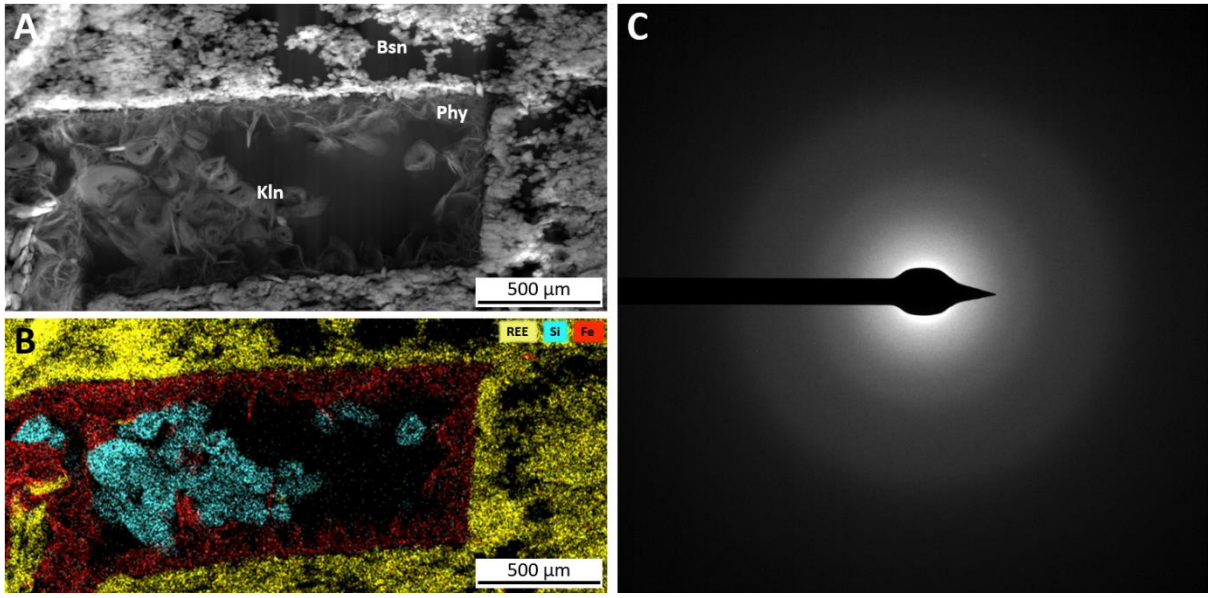

Figure 4.10. A) STEM image showing the presence of kaolinite subgroup phase (Kln) and undefined phyllosilicate (Phy) within bastnäsite-(Nd) nanocrystals (Bsn). B) EDS map of A. C) SAED pattern of kaolinite-like phase indicating an almost amorphous material.

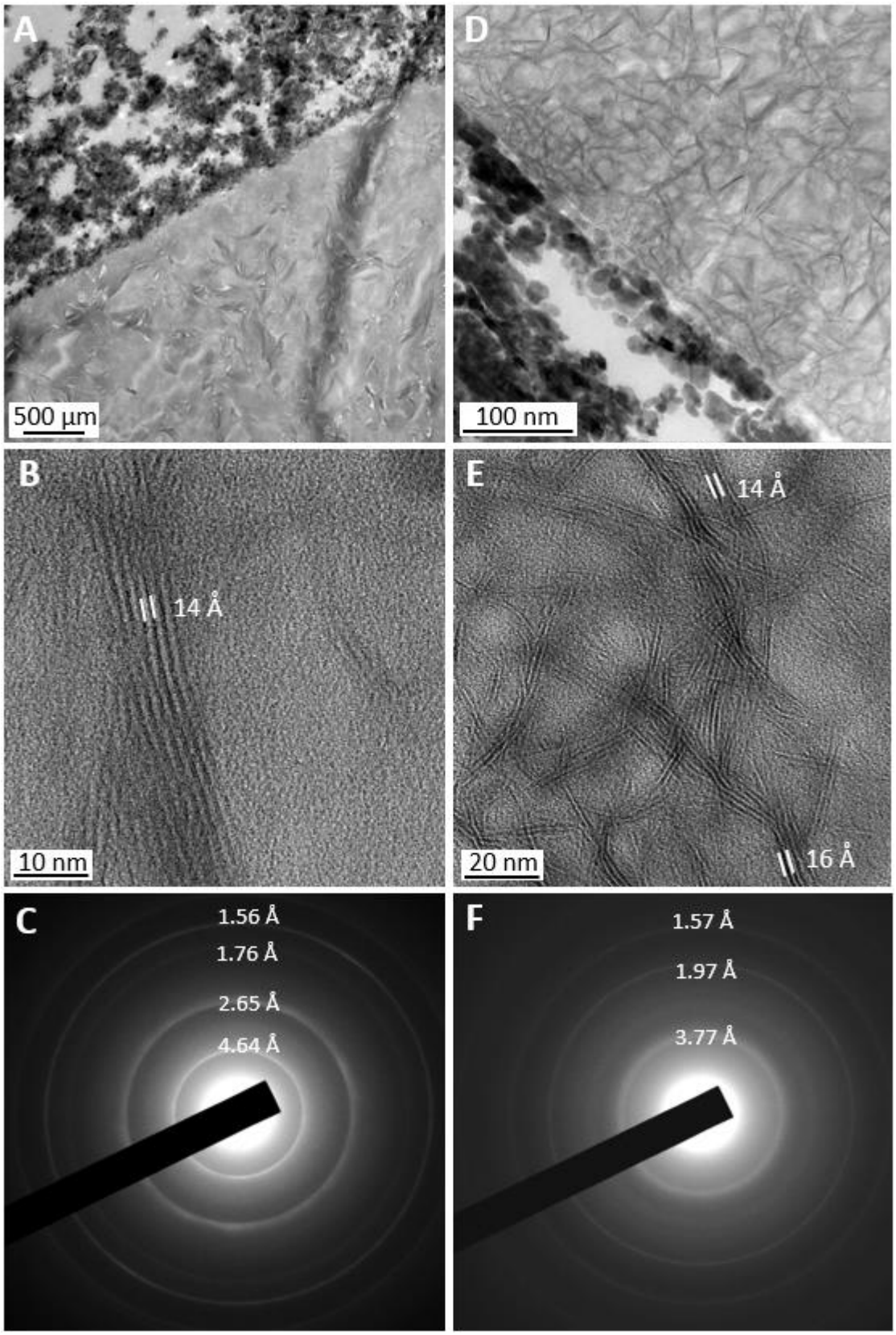

Figure 4.11. A, B and C) Bright field, lattice fringe and SAED pattern images of the first undefined phase (undefined I). D, E and F) Bright field, lattice fringe and SAED pattern images of the second undefined phase (undefined II). The SAED patterns of both phases are typical of a nanocrystalline material. The main diffraction rings are indicated.

4.5. Discussion and Conclusions

The miarolitic cavities of the granophyre of Cuasso al Monte are filled with minerals of hydrothermal origin. Indeed, several authors agree that a massive fluid circulation involved a significant portion of the Serie dei Laghi, including the granophyre (Pezzotta et al., 1999, 2005; Demartin et al., 2001; Vignola et al., 2012; Capitani et al., 2018). These fluids were also responsible for the alteration of K-feldspar, biotite and plagioclase. Based on the study of Sc-silicates, Pezzotta et al. (2005) proposed two different models to explain the precipitation of rare hydrothermal phases into miarolitic cavities and both agree that CRFC were formed as final product in a low temperature environment. REE as well as other elements (e.g. Ti, Nb, Ta, Sc, etc.) were made available by the activity of F-rich fluids, which have altered primary gadolinite-(Y), siderophyllite, feldspar, and other rock-forming minerals.

Capitani et al. (2018), on the basis of the textural relationships involving anatase, aeschynite and zircon from the same miarolitic cavities, depicted a scenario in which F-rich hydrothermal fluids altered primary minerals and then, on cooling, deposited accessory phases in a sequence that reflected fluids saturation and elements fractionation within a range of 250-100 °C. REE-carbonates were among the latest phases to crystallize and, in the case that hydrothermal fluids contained enough Ca^{2+} ions, synchysite was the first CRFC to precipitate, analogously to what observed in magmatic contexts (Förster, 2001 and references therein). Indeed, it has been observed experimentally, although at higher temperatures (300-400 °C), that the stability field of Ca-bearing CRFC (parisite in this case) is wider at high temperature than at low temperature, in comparison to bastnäsite, and expand with increasing $a(Ca^{2+})$ and decreasing $a(F^{-})$ (Gysi and William-Jones, 2015).

Laboratory experiments have been used to better constrain the precipitation pathway of REE bearing minerals (i.e. REE-carbonates and REE-hydroxylcarbonates) in nature. However, a general mechanism has not been conceived yet because of the many factors intervening in the REE-carbonates precipitation under hydrothermal conditions. Among the main factors affecting crystal morphology there are the dominant REE in the system, temperature and time rate of crystallization (Price et al., 2023; Rodriguez-Blanco et al., 2014; Szucs et al., 2023; Vallina et al., 2014), as already known for other, more common carbonates such as calcite (Liendo et al., 2022).

The zoning affecting synchysite-(Ce) prisms and the different compositions of rosette-like CRFC may be due to either fractional crystallization or leaching/deposition by a metasomatic fluid. The zoning affecting synchysite-(Ce) prism is core to rim and along the prism length (Fig. 4.2C). This pattern is inconsistent with a later metasomatic fluid, which should have affected homogeneously from the exterior to the interior the crystals along their length. Instead, the observed pattern is consistent with both a fluid that changed composition during the growth of the prism radially and longitudinally, and with the relative higher facility to crystallize light-REE CRFC respect to their heavy-REE-counterpart (Rodriguez-Blanco et al., 2014; Szucs et al., 2021). Indeed, Ce, La and Nd enter the crystal structure earlier than Y, which notably behaves as a heavy-REE.

Synchysite-(Ce), both in rosettes or prisms, as well as the other CRFC, are often found included at the rims of euhedral quartz and feldspar or on them and on chamosite. Synchysite-(Ce) was also found included in fluorite. This means that all the detected CRFC morphologies and

compositions crystallized in the latest stage of feldspar, quartz and chamosite crystallization and shortly after.

The pink colour of feldspar is commonly attributed to the presence of microscopic hematite inclusions deposited by post-magmatic hydrothermal fluid, which may also cause albitization of K-feldspar (Kaur et al., 2012). A Na-replacement in K-feldspar was actually observed towards the rim of the crystals (Fig. 4.12), and hematite is abundant within CRFC. Therefore, even if we did not focus our TEM investigation on K-feldspar, which in that case would have unveiled any presence of hematite, we can reasonably assume that the vivid reddish colour of K-feldspar is due to metasomatism.

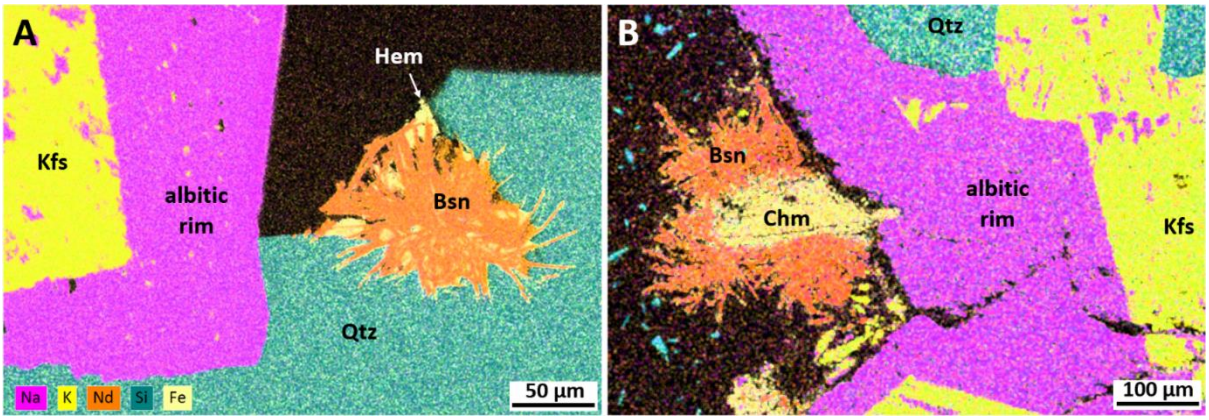

Figure 4.12. SEM-EDS maps showing a Na-enrichment of the rim of K-feldspar (Kfs) and bastnäsite (Bsn) in quartz (Qtz) (A) and on the albitic rim of K-feldspar (B). Hem and Chm refer to hematite and chamosite, respectively

Albitization of feldspar and hydrothermal crystallization of quartz and chamosite may occur over a broad temperature range: albitization of feldspar between 350–450 °C (Kaur et al., 2012 and references therein); quartz crystallization between 100–700 °C (Rusk et al., 2008) and chamosite crystallization between 80–600 °C (Fulignati, 2020; Bourdelle, 2021). Thus, we can reasonably hypothesize an upper temperature limit of approximately 350-450 °C as the initiation of crystallization of CRFC, with the different compositions and morphologies attributed to fluid fractionation under decreasing temperature.

Indeed, Vallina et al. (2014), studying the crystallization of hydroxylbastnäsite-(Nd) ($NdCO_3OH$) through hydrothermal synthesis at variable temperatures (165-220 °C), found that different shapes and crystal sizes can be obtained as a function of temperature and rate of heating. The more regular and idiomorphic morphologies (triangular pyramids and spine-shaped aggregates) were obtained when the supersaturation conditions were reached more slowly (at low temperature and slow heating rate), whereas, more irregular cauliflower-like and fishbone (dendritic) morphologies were obtained when the supersaturation conditions were reached quickly. Analogous observations were made before by Gai et al. (2014).

On the other hand, there is a relatively large body of evidence from hydrothermal syntheses of REE-carbonates indicating that the REE composition influences the resulting crystal morphology. For instance, Rodriguez-Blanco et al. (2014) synthetizing REE-lanthanites ($REE_2(CO_3)_3 \cdot 8H_2O$) from aqueous solutions at ambient temperature found that in all experiments lanthanites formed from a poorly ordered nanoparticulate precursor and that the differences in ion size and ionic potential as well as differences in dehydration energy of the

REE^{3+} ions control the crystallization kinetics, unit-cell dimensions and morphology of the final crystalline lanthanites. In particular, lanthanites containing heavier REE^{3+} ions (Nd^{3+} or Pr^{3+}) developed smaller crystallites compared to their lighter La^{3+}- or Ce^{3+}-bearing counterparts. Moreover, while lanthanite-(La) developed well-formed and euhedral shapes, heavier REE^{3+}-bearing lanthanites (Ce, Pr and Nd) progressively developed more subhedral shapes with crystal imperfections (twinning). Price et al. (2023) synthetizing La-Nd carbonates from aqueous solutions at 30 °C, found that the final (stable) pure La-carbonate, pure-Nd-carbonate and mixed La-Nd carbonate had different morphologies and crystal sizes. As for Rodriguez-Blanco et al. (2014), they found that the precursor of lanthanites was an amorphous REE nanoparticle aggregate. Szucs et al. (2023) studying the crystallization of REE carbonates at hydrothermal conditions (21-220 °C) through mineral replacement reactions, starting from dolomite and aragonite seeds, found that maintaining constant the parameters during the synthesis, notably the reaction temperature, duration and the nature of the seeds, the final morphology was different for different targeted REE. At the highest investigated temperature range (165-220 °C), hydroxylbastnäsite ($REECO_3OH$) was the stable phase, while lanthanite was favoured at lower temperatures (21-80 °C). Although all the above examples deal with simplified systems, lacking fluorine as component and employing only few REE, it is reasonable to assume that in more complex REE-Ca-CO_3-F systems, the composition of the fluid could, at least in part, control the morphology of the crystallizing REE carbonate.

In this work, synchysite-(Ce), other than included in quartz and feldspar, was also found included in fluorite. This may suggest that the fluid, initially with a high concentration of Ca and F, reached the conditions for the crystallization of fluorite and synchysite-(Ce), subtracting Ca and entering into the conditions to crystallize bastnäsite-(Ce). In this scenario, bastnäsite-(Nd) is the last CRFC to crystallize, in agreement with thermodynamic studies (Gysi and Williams-Jones, 2015). Its "desert-rose" microstructure is consistent with a low temperature phase – desert roses are supposed to form in evaporitic environment at ambient conditions – and the nanoparticle structure may represent the nanoparticle precursors described in the experiments (Rodriguez-Blanco et al., 2014; Vallina et al., 2014; Price et al., 2023) that never matured into larger and regular crystals due to the low temperature, which hindered elemental diffusion and aggregation.

In summary, this scenario suggests: (i) synchysite-(Ce) prisms formed early in the crystallization sequence from a Ca- and F-rich fluid, at relatively low cooling rate; (ii) the Ca-depleted fluid then reached the condition to form blocky bastnäsite-(Ce), still at relatively low cooling rates; (iii) the fluid reached again, at slightly lower temperatures, supersaturation conditions for Ca and Ce, crystallizing rosette-like synchysite-(Ce). Indeed, the large number of "petals" of synchysite-(Ce) may represent fast nucleation events under a relatively high cooling rate that resulted into undeveloped prisms; (iv) the remaining fluid, at that point depleted in Ca and Ce and at low temperature, crystallized rosette-like bastnäsite-(Nd) (Figure 4.13).

The scaffold nanostructure made of bastnäsite-(Nd) nanocrystals walled by solid synchysite-(Ce) may suggests that the hydrothermal fluid supersaturation conditions oscillated slightly between those suitable for the crystallization of bastnäsite-(Nd) and those suitable for synchysite-(Ce).

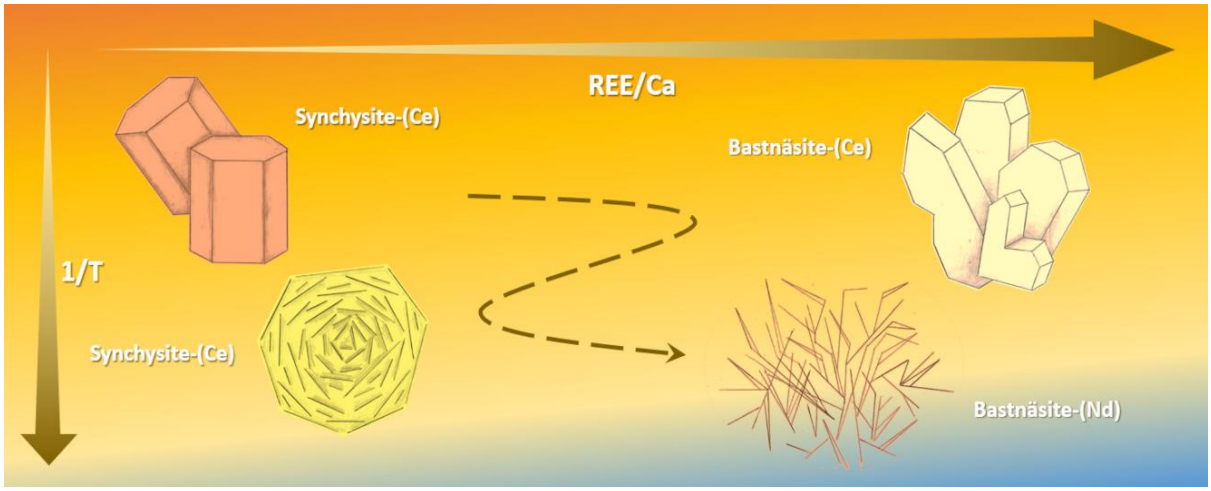

Figure 4.13. Drawing showing the possible crystallization pathway of CRFC in Cuasso al Monte.

Kaolinite type minerals, notably low temperature phases (Marumo, 1989; Erkoyun and Kadir, 2010; Yuan et al., 2014), are intergrown with CRFC, and may represent the residue of the silicate fluid deriving from the leaching of primary feldspars and iron-rich phases of the granophyre and associated volcanic rocks. The presence of these phyllosilicates, together with hematite, may have hampered (physically) the development of larger single crystals of bastnäsite-(Nd). On the other hand, the bastnäsite nanostructure is also consistent with the fact that Nd-carbonate is more difficult to crystallize than light-REE-carbonates, and usually leads to smaller crystals (Rodriguez-Blanco et al., 2014; Szucs et al., 2021). Moreover, the bastnäsite-(Nd) nanoparticles closely resemble the REE-nanoparticle aggregate precursors often observed experimentally (e.g. Vallina et al., 2014; Rodriguez-Blanco et al., 2014; Price et al., 2023) and may represent the final morphology assumed at the end of crystallization under low temperature, high cooling rate and fast nucleation process from a supersaturated solution. Finally, Th sometimes observed in the rim of the CRFC crystals, may derive from hydrothermal alteration of zircon and other accessory phases in the granophyre (e.g. thorite and monazite). It has been observed that Th has affinity for Y (i.e. Y-Th zoning in hexagonal prism synchysite-(Ce)) and enters the crystal structure of CRFC at the latest stage of crystallization.

Chapter 5

Average Structure and Microstructure of Synchysite-(Ce) from Cuasso al Monte (Italy)

5.1 Introduction

Like the other members of the series, synchysite-(Ce) has a layered topology with planar carbonate groups "standing-on-edge" with respect to the overall structural layering (Grice, 2007). One significant consequence of this structural layering is the formation of syntaxial intergrowths, resulting in ordered and disordered domains with polysomatic and polytypic connections (Donnay and Donnay, 1953; Wang et al., 1994; Ni et al., 2000; Capitani, 2019, 2020). The existence of syntaxial intergrowths and related disordering has for a long time hampered the solution of the crystal structure of CRFC. The crystal structure of synchysite-(Ce) was only solved relatively recently by Wang et al. (1994); while that of bastnäsite-(Ce) was solved just a year earlier (Ni et al., 1993) and that of parisite-(Ce), the only intermediate member whose structure has been successfully refined, somewhat later (Ni et al., 2000).

In this chapter, the synchysite-(Ce) with hexagonal prism morphology from Cuasso al Monte, previously described in Chapter 4, has been studied with a multi-methodological approach, namely SCXRD, Raman spectroscopy, TEM-EDS and 3DED, to determine its structure and microstructure. The study has several objectives: i) to compare the structure and microstructure of synchysite-(Ce) from Cuasso al Monte with the few available literature data; ii) to compare SCXRD and 3DED structural data, with 3DED applied for the first time to this mineral group; and iii) to gather insights into crystal growth and REE fractionation.

This chapter, with modification, is currently under review as: "*Conconi, R., Merlini, M., Fumagalli, P., Mugnaioli, E., Folco, L., Capitani, G., 2024c. Average Structure and Microstructure of Synchysite-(Ce) from Cuasso al Monte (Varese, Italy), European Journal of Mineralogy"*

5.2 Samples and Methods

The synchysite-(Ce) crystals from Cuasso al Monte studied here are the same as those presented in Chapter 4 (Figs. 4.2 and 4.3). These crystals show a hexagonal prismatic morphology, are microscopic in size and have a reddish colour with evident zoning (Fig. 5.1). Overall, five crystals were prepared and studied. A table reporting the type of analysis performed for each individual crystal is provided in the Table 5.1.

Single crystals (or what appeared to be) were extracted from miarolitic cavities, mounted on glass fibres and studied using SCXRD diffractometry. Structure refinement was attained by the full-matrix least-squares on F^2 method implemented in the Shelx (version 2018/3) program (Sheldrick, 2015). The refinement was done in the *C*2/*c* space group using the structure of Wang et al. (1994) as initial guess. The synchysite structure comprises two symmetry distinct sites for Ca atoms (Ca1 in special and Ca2 in general position) and two for Ce atoms (Ce1 in special and Ce2 general position). The occupancies of these sites were refined as Ca vs. Yb and Ca vs. Ce for Ca-sites and Ce-sites, respectively, to take into account the exceeding electron density respect the ideal one, and constraining the occupancy to 1 atom per site. Ce, Ca (and Yb) were refined anisotropically, C, O and F isotropically. Soft restraints were used only for the C-O bond distances.

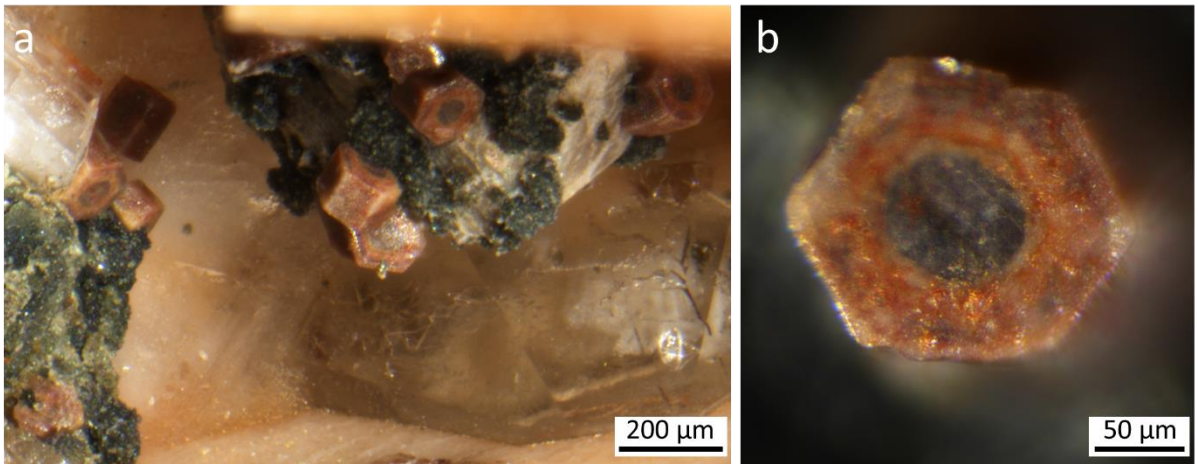

Figure 5.1. (a) Optical micrograph photos showing the hexagonal prism synchysite-(Ce) into the miarolitic cavity and (b) showing the zoning.

Table 5.1. Summary of the analytical techniques employed on each individual sample

Sample	SEM-EDS	Raman	SCXRD	TEM-EDS	3DED	Notes
FCBN1			x			Lost
FCBN2	x		x			
FCBN3	x	x	x			
FCBN4			x			Lost
FCBN5				x	x	2 thin foils

After SCXRD study, the samples were embedded in epoxy resin, with the basal (001) section parallel to the resin surface, polished with alumina (final grain size 0.3 µm) and studied using Raman spectroscopy and SEM-EDS.

Finally, the FIB technique was used to prepare TEM lamellae. The lamellae were extracted from the (001) synchysite surface, to have the **c***-axis on the observation plane at the TEM. Two lamellae were extracted from areas with different elemental distributions, guided by SEM-EDS maps. Specifically, one lamella (thin foil 1, TF01) was extracted halfway between the Ce-rich core and the Y-rich rim of the FCBN5 sample; the second lamella (thin foil 2, TF02) was extracted halfway between the Y-rich rim and the Th-rich outer rim of the same crystal (Fig. 5.2). The lamellae were then studied using both TEM-EDS and 3DED. Regarding 3DED, several data collections were obtained in different areas of the lamellae to cover the chemical zoning detected by SEM-EDS. *Ab initio* structure solutions attempted using the SIR-2019 software (Burla et al., 2015) resulted in approximate synchysite structures with heavy atoms in their expected position, but missing some C and O atoms. Therefore, structure refinement was performed using the structure of Wang et al. (1994) as initial model, as well as was done for the SCXRD refinement. The software Jana 2020 (Petříček et al., 2023) was used for dynamical structure refinement. Soft restraints were applied to C-O bonds and O-C-O angles, and CO_3 groups were constrained to remain planar. Several refinement schemes were attempted for the occupancy of the Ca- and Ce-sites, but satisfactory results were obtained by setting the Ca content to 0.90 and Th to 0.10 in both Ca-sites, and Ce content to 0.90 and Th to 0.10 in both Ce-sites.

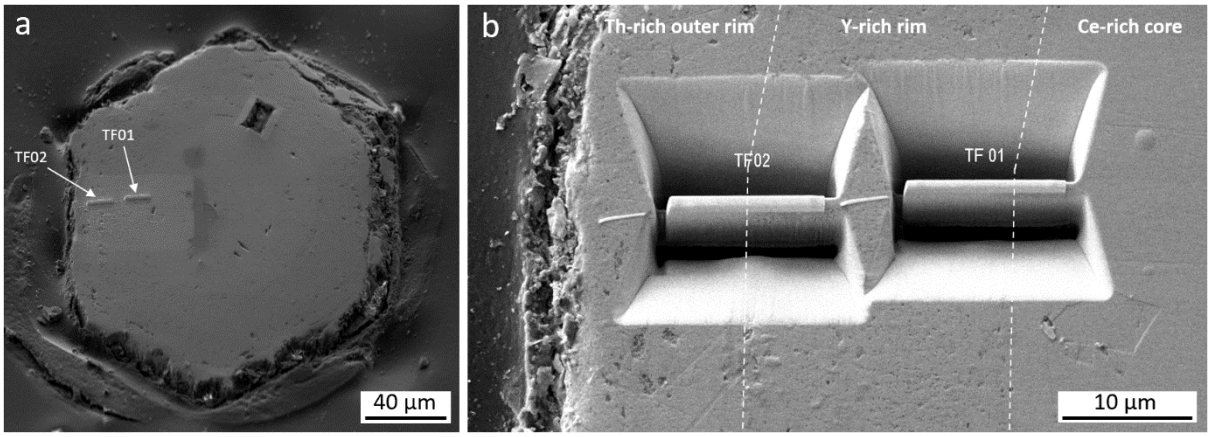

Figure 5.2. (a) Secondary electron SEM image of sample FCBN5 showing the Pt strips deposited on the sites where the two thin foils were extracted. A third one, at the centre top of the hexagonal prism, went lost. (b) The two lamellae seen at higher magnification after FIB excavation and before extraction.

5.3 Results

5.3.1 Average structure: Single crystal X-ray diffraction

All four SCXRD structure refinements yielded acceptable and similar results. Relevant experimental and crystallographic data are reported in Table 5.2 along with data from Wang et al. (1994) and 3DED data for comparison. While the polytypic disorder posed the primary challenge during structure refinements, additional factors such as chemical zoning, fluid and solid inclusions and partial metamictization also played a role. Despite these complexities, the refinements provided valuable insights into structural parameters.

Based on the chemical analyses, the Ca-sites should be fully occupied by Ca, and the Ce-sites by REE and Th, as Ca remains nearly constant and close to its ideal value of one a.p.f.u. Meanwhile, Ce, La and Nd are directly correlated with each other and inversely correlated with Y, which, in turn, is inversely correlated with Th at the outer rim of the crystals. However, from the initial refinement cycles, it was clear that the apparent electron density at the Ca-sites was higher than the expected ~20 electrons and the electron density at the Ce-sites exceeded the expected ~58 electrons. Therefore, to address this discrepancy, a fictitious Ca vs. Yb and Ca vs. Ce occupancy model was refined for the Ce-sites and both the Ca-sites. The refinement converged to similar values for both the Ca1- and Ca2-sites, as well as for the Ce1- and Ce2-sites, resulting in the values reported in Table 5.2, namely 30-31 electrons for the Ca-sites, and 59-65 electrons for the Ce-sites. Although these values clearly do not perfectly align with the measured chemical composition, this discrepancy is likely correlated with crystal defects.

Overall, the four refined crystals are very similar in terms of crystal geometry and closely resemble the reference sample (Table 5.3), although the latter shows slightly larger cell and very slightly longer bond lengths, in particular C1-O, Ca1-O, Ce1-F and Ce2-O bonds, probably due to the different compositions. Indeed, according to Wang et al. (1994), their refined crystal from Mont Saint-Hilaire (Quebec), has composition: $Ca_{0.94}Ce_{0.62}La_{0.32}Th_{0.01}Eu_{0.008}Y_{0.02}C_{1.96}O_6F_{0.64}$, whereas the crystals studied here are core-rim zoned with average an compositions: $Ca_{1.04}Ce_{0.39}Nd_{0.18}La_{0.15}Y_{0.08}Pr_{0.05}Sa_{0.04}Gd_{0.03}Th_{0.04}$

$(CO_3)_2F_{0.70}$ (FCN2) and $Ca_{1.01}Ce_{0.37}Nd_{0.20}Y_{0.17}La_{0.09}Pr_{0.05}Sa_{0.05}Gd_{0.03}Th_{0.03}$ $(CO_3)_2F_{0.72}$ (FCN3). $^{IX}Ce^{3+}$ (ionic radius 1.196 Å) and $^{IX}La^{3+}$ (1.216 Å), which are more abundant in the reference sample, have ionic radii larger than $^{IX}Nd^{3+}$ (1.163) and $^{IX}Y^{3+}$ (1.075), which are more abundant in the samples studied here, therefore explaining the difference.

Table 5.2. Crystal and SCXRD structure refinement data for the four crystals refined (FCBN1-4) along with the reference (REF) sample (Wang et al., 1994) and 3DED data (TF01, Ce-rich core, FCBN5).

	FCBN1	FCBN2	FCBN3	FCBN4	3DED	REF
a (Å)	12.2002(9)	12.2757(9)	12.2774(13)	12.2195(13)	12.3544(40)	12.329(2)
b (Å	7.0427(3)	7.0870(5)	7.0900(6)	7.0519(8)	7.1239(25)	7.110(1)
c (Å)	18.6081(13)	18.6559(12)	18.6619(18)	18.621(2)	18.8712(80)	18.741(2)
β (°)	102.603(7)	102.662(7)	102.663(11)	102.601(11)	102.53(22)	102.68(1)
Volume (Å^3)	1560.33(18)	1583.57(19)	1584.9(3)	1565.9(3)	1621.3(10)	1602.8 (3)
Calc. Dens. (g/cm^3)	4.640	4.572	4.463	4.517	3.915	3.969
Data/restr./param.	1778/9/88	1803/9/88	1747/9/88	1814/9/88	1402/15/126	2319/?/95
Good.-of-fit on F^2	1.141	1.140	1.130	1.128	2.249	2.448
Ref. Occup. (e^-)	65/65	60/61	61/62	59/60	58.7/58.7	??
Ce1/Ce2/Ca1/Ca2	31/31	31/30	30/30	31/30	24.4/24.5	
R_{int}	0.0251	0.0243	0.0212	0.0526	0.1131	0.016
$R_{4\sigma}$	0.1085	0.1072	0.1168	0.1120	0.1541	0.036
R_1	0.1437	0.1449	0.1514	0.1775	0.2637	??

The CO_3 bond lengths distribution are comparable among the four refined structures, but the CO_3 polyhedra are slightly more distorted than in the reference structure, with one systematically longer and one systematically shorter distance (Table 5.3). This difference may be due to the polytypic disorder affecting the samples from Cuasso al Monte, since polytypic disorder mostly involves the shifting of CO_3-layers (see ahead).

The bond length distribution of the Ca1-site, in special position, is very similar across the four refined structures and to the reference, with one bond systematically longer, one systematically shorter and two intermediate distances (Table 5.3). The bond length distribution of the Ca2-site, in general position, is also very similar in the four refined structures, but differs from the reference, where the site is reported as 7-fold coordinated, while it is 8-fold coordinated in our structures. However, the average bond length matches perfectly.

The Ce1-O bond length distribution is comparable among the four refined structures and the reference, with one systematically shorter distance. The Ce1-F bond distances are all similar within two standard deviations for the four refined structures, as they are for the reference, although on average slightly longer for the latter. The Ce2-O bond length distribution is also consistent between the four refined structures and the reference, with two systematically shorter

distances. The Ce2-F bonds show one systematically shorter distance in the four refined structures, whereas they are all similar in the reference. Nonetheless, the average values of both Ce1-F and Ce1-O bonds are comparable to those in the reference.

As regards the atomic displacement factors, despite the high level of disorder, they remain within normal values for all atomic species and for all four refined crystals. Atomic positions and displacement factors are reported in Table 5.4 and 5.5.

Table 5.3. Bond lengths (A) and angles (°) for the four crystals refined with SCXRD (FCBN1-4). For comparison, the structure refinement from 3DED data (TF01, Ce-rich core, FCBN5) and the reference (REF) sample (Wang et al., 1994) are reported.

	FCBN1	FCBN2	FCBN3	FCBN4	3DED	REF
C1-O1	1.37 (3)	1.37 (3)	1.35 (3)	1.38 (4)	1.22 (2)	1.32 (2)
-O2	1.23 (2)	1.23 (2)	1.28 (3)	1.25 (3)	1.29 (2)	1.30 (2)
-O3	1.17 (3)	1.17 (3)	1.20 (3)	1.18 (3)	1.25 (2)	1.24 (3)
Mean	**1.26**	**1.26**	**1.28**	**1.27**	**1.25**	**1.29**
C2-O4	1.37 (3)	1.37 (3)	1.38 (3)	1.39 (4)	1.23 (2)	1.31 (3)
-O5	1.28 (2)	1.28 (2)	1.27 (3)	1.29 (3)	1.31 (2)	1.29 (3)
-O6	1.20 (2)	1.20 (2)	1.24 (3)	1.22 (3)	1.24 (2)	1.27 (2)
Mean	**1.29**	**1.29**	**1.30**	**1.30**	**1.26**	**1.29**
C3-O7	1.17 (3)	1.17 (3)	1.20 (2)	1.22 (3)	1.22 (3)	1.27 (2)
-O8	1.36 (4)	1.36 (4)	1.34 (3)	1.29 (4)	1.27 (3)	1.26 (3)
-O9	1.25 (2)	1.25 (2)	1.24 (2)	1.23 (3)	1.24 (2)	1.26 (2)
Mean	**1.26**	**1.26**	**1.26**	**1.25**	**1.25**	**1.27**
Ca1-O2 x2	2.47 (1)	2.49 (1)	2.48 (2)	2.53 (2)	2.40 (2)	2.47 (1)
-O5 x2	2.44 (1)	2.46 (2)	2.44 (2)	2.46 (2)	2.41 (2)	2.47 (2)
-O8 x2	2.36 (3)	2.36 (3)	2.38 (3)	2.39 (4)	2.53 (2)	2.37 (1)
-O9 x2	2.67 (2)	2.68 (2)	2.71 (2)	2.65 (2)	2.99 (2)	2.75 (2)
Mean	**2.49**	**2.50**	**2.50**	**2.51**	**2.58**	**2.52**
Ca2-O1	2.34 (2)	2.36 (2)	2.33 (3)	2.40 (4)	2.53 (2)	2.37 (1)
-O2	2.45 (1)	2.42 (1)	2.42 (2)	2.36 (2)	2.53 (3)	2.45 (2)
-O2	2.68 (2)	2.69 (2)	2.72 (2)	2.68 (2)	2.61 (2)	-
-O4	2.36 (2)	2.32 (2)	2.34 (3)	2.33 (3)	2.45 (2)	2.35 (1)
-O5	2.68 (1)	2.67 (2)	2.71 (2)	2.64 (2)	2.68 (2)	2.66 (1)
-O5	2.47 (1)	2.47 (1)	2.49 (1)	2.47 (2)	2.65 (3)	2.47 (2)
-O9	2.45 (2)	2.46 (2)	2.45 (2)	2.47 (2)	2.37 (2)	2.45 (1)
-O9	2.41 (2)	2.44 (2)	2.42 (2)	2.42 (2)	2.36 (2)	2.43 (2)
Mean*	**2.45**	**2.45**	**2.45**	**2.44**	**2.52**	**2.45**
Ce1-F1	2.36 (2)	2.32 (2)	2.38 (2)	2.33 (2)	2.59 (4)	2.42 (2)
-F2 x2	2.34 (2)	2.38 (1)	2.35 (2)	2.37 (2)	2.29 (2)	2.40 (2)
Mean	**2.35**	**2.36**	**2.36**	**2.35**	**2.39**	**2.41**
Ce1-O3 x2	2.59 (2)	2.63 (2)	2.61 (2)	2.56 (3)	2.62 (3)	2.58 (1)
-O4 x2	2.42 (2)	2.51 (3)	2.45 (3)	2.47 (3)	2.51 (2)	2.52 (1)
-O7 x2	2.58 (2)	2.57 (2)	2.58 (2)	2.58 (2)	2.55 (2)	2.57 (1)
Mean	**2.53**	**2.57**	**2.55**	**2.54**	**2.56**	**2.56**
Ce2-F1	2.37 (1)	2.41 (1)	2.39 (1)	2.39 (1)	2.31 (2)	2.38 (1)
-F2	2.32 (1)	2.36 (1)	2.33 (1)	2.33 (2)	2.30 (2)	2.38 (2)
-F2	2.41 (1)	2.39 (1)	2.46 (2)	2.40 (2)	2.59 (3)	2.41 (2)
Mean	**2.37**	**2.39**	**2.39**	**2.37**	**2.40**	**2.39**
Ce2-O1	2.48 (2)	2.48 (2)	2.49 (3)	2.46 (4)	2.46 (2)	2.50 (1)
-O3	2.57 (2)	2.57 (2)	2.59 (2)	2.57 (3)	2.55 (2)	2.62 (1)
-O6	2.57 (2)	2.54 (2)	2.58 (2)	2.52 (3)	2.61 (2)	2.60 (1)
-O6	2.60 (2)	2.65 (2)	2.62 (2)	2.66 (3)	2.68 (2)	2.62 (1)

-O7	2.53 (2)	2.56 (2)	2.55 (2)	2.54 (3)	2.60 (2)	2.56 (1)
-O8	2.51 (3)	2.53 (3)	2.54 (3)	2.49 (4)	2.65 (2)	2.50 (1)
Mean	**2.54**	**2.56**	**2.56**	**2.54**	**2.59**	**2.57**

*For comparison with the reference, the average does not consider the Ca2-O2 longest bond distance.

Table 5.4. Atomic coordinates (x 10^4) and equivalent isotropic displacement parameters (A^2 x 10^3) for (from top to bottom) samples FCBN1 to FCBN4. U_{eq} is defined as one third of the trace of the orthogonalized U_{ij} tensor.

	X	y	z	U_{eq}		x	y	z	U_{eq}
Ce1	5000	2543(2)	2500	18(1)	O1	4341(17)	2970(30)	8791(12)	40(5)
Ce11	5000	2543(2)	2500	18(1)	O2	9242(11)	740(20)	520(8)	8(3)
Ce2	6680(1)	2515(2)	7502(1)	14(1)	O3	9513(17)	650(30)	1751(11)	36(5)
Ce21	6680(1)	2515(2)	7502(1)	14(1)	O4	4914(17)	1940(30)	3767(12)	41(5)
Ca1	2500	2500	5000	20(2)	O5	6108(11)	743(19)	494(7)	5(3)
Ca11	2500	2500	5000	20(2)	O6	6654(15)	530(30)	1735(10)	30(5)
Ca2	9142(2)	2477(4)	5005(2)	21(1)	O7	3079(16)	1350(30)	1773(10)	29(4)
Ca21	9142(2)	2477(4)	5005(2)	21(1)	O8	7070(20)	1250(40)	8792(16)	72(9)
C1	9675(16)	1060(30)	1171(10)	9(4)	O9	2653(15)	1060(30)	513(9)	25(4)
C2	3953(15)	1020(20)	3834(9)	2(4)	F1	5000	810(30)	7500	25(5)
C3	2932(15)	680(30)	1183(9)	2(3)	F2	8420(12)	780(20)	7675(8)	25(3)
Ce1	5000	2536(2)	2500	18(1)	O1	4338(18)	3000(30)	8785(12)	52(6)
Ce11	5000	2536(2)	2500	18(1)	O2	9243(11)	690(20)	499(7)	17(3)
Ce2	6679(1)	2508(2)	7502(1)	18(1)	O3	9518(18)	690(30)	1756(11)	51(6)
Ce21	6679(1)	2508(2)	7502(1)	18(1)	O4	4885(19)	1900(40)	3806(13)	59(7)
Ca1	2500	2500	5000	26(2)	O5	6079(12)	740(20)	472(8)	21(3)
Ca11	2500	2500	5000	26(2)	O6	6582(16)	540(30)	1773(10)	41(5)
Ca2	9140(2)	2483(4)	5003(2)	24(1)	O7	3100(15)	1320(30)	1780(9)	33(4)
Ca21	9140(2)	2483(4)	5003(2)	24(1)	O8	7070(20)	1230(40)	8802(16)	83(9)
C1	9671(15)	1060(30)	1150(10)	12(4)	O9	2667(14)	1040(30)	517(9)	29(4)
C2	3894(14)	980(30)	3838(9)	6(3)	F1	5000	740(30)	7500	32(5)
C3	2903(16)	600(30)	1182(9)	14(4)	F2	8399(11)	800(20)	7684(7)	28(3)
Ce1	5000	2544(3)	2500	18(1)	O1	4340(20)	2950(40)	8798(14)	51(7)
Ce11	5000	2544(3)	2500	18(1)	O2	9224(14)	680(30)	509(9)	19(4)
Ce2	6679(1)	2509(2)	7502(1)	16(1)	O3	9547(17)	680(30)	1764(11)	34(5)
Ce21	6679(1)	2509(2)	7502(1)	16(1)	O4	4930(20)	1940(40)	3782(15)	55(7)
Ca1	2500	2500	5000	20(2)	O5	6118(11)	750(20)	490(7)	7(3)
Ca11	2500	2500	5000	20(2)	O6	6626(18)	560(30)	1748(11)	40(6)
Ca2	9141(3)	2473(5)	5001(2)	21(1)	O7	3088(16)	1370(30)	1775(10)	25(4)
Ca21	9141(3)	2473(5)	5001(2)	21(1)	O8	7070(20)	1190(40)	8798(16)	66(8)
C1	9684(17)	1130(30)	1170(11)	10(4)	O9	2660(14)	1090(30)	509(9)	21(4)
C2	3950(18)	1080(30)	3851(11)	14(5)	F1	5000	810(30)	7500	27(5)
C3	2916(15)	700(20)	1170(9)	0(3)	F2	8443(13)	750(20)	7692(9)	31(4)
Ce1	5000	2538(3)	2500	22(1)	O1	4370(30)	3030(50)	8770(20)	102(12)
Ce11	5000	2538(3)	2500	22(1)	O2	9263(15)	620(30)	503(10)	28(5)
Ce2	6680(1)	2504(2)	7502(1)	21(1)	O3	9500(20)	600(40)	1761(14)	68(8)
Ce21	6680(1)	2504(2)	7502(1)	21(1)	O4	4930(20)	1870(50)	3792(16)	74(9)
Ca1	2500	2500	5000	34(2)	O5	6065(14)	750(30)	471(9)	22(4)
Ca11	2500	2500	5000	34(2)	O6	6588(18)	510(40)	1760(11)	46(6)
Ca2	9137(2)	2470(5)	5001(2)	22(1)	O7	3091(18)	1250(30)	1797(11)	39(5)
Ca21	9137(2)	2470(5)	5001(2)	22(1)	O8	7040(30)	1230(50)	8780(20)	114(14)
C1	9629(18)	1010(30)	1168(11)	13(5)	O9	2657(14)	1020(30)	516(9)	20(4)
C2	3913(18)	1060(30)	3843(11)	13(5)	F1	5000	760(30)	7500	23(5)
C3	2892(18)	590(30)	1174(11)	11(5)	F2	8408(14)	770(30)	7678(9)	37(5)

Table 5.5. Anisotropic displacement parameters for (A^2 x 10^3) for (from top to bottom) samples FCBN1 to FCBN4. The anisotropic displacement factor exponent takes the form: $-2\pi^2[h^2a^{*2}U_{11} + ... + 2hka^*b^*U_{12}]$.

	U_{11}	U_{22}	U_{33}	U_{23}	U_{13}	U_{12}
Ce1	18(1)	22(1)	13(1)	0	3(1)	0
Ce11	18(1)	22(1)	13(1)	0	3(1)	0
Ce2	16(1)	14(1)	13(1)	0(1)	3(1)	0(1)
Ce21	16(1)	14(1)	13(1)	0(1)	3(1)	0(1)
Ca1	26(3)	22(2)	14(2)	1(2)	8(2)	1(2)
Ca11	26(3)	22(2)	14(2)	1(2)	8(2)	1(2)
Ca2	20(2)	23(2)	21(2)	1(1)	3(1)	-4(1)
Ca21	20(2)	23(2)	21(2)	1(1)	3(1)	-4(1)
Ce1	17(1)	20(1)	16(1)	0	2(1)	0
Ce11	17(1)	20(1)	16(1)	0	2(1)	0
Ce2	18(1)	21(1)	15(1)	0(1)	3(1)	0(1)
Ce21	18(1)	21(1)	15(1)	0(1)	3(1)	0(1)
Ca1	25(2)	30(3)	23(2)	6(2)	8(2)	4(2)
Ca11	25(2)	30(3)	23(2)	6(2)	8(2)	4(2)
Ca2	23(2)	24(2)	24(2)	6(1)	3(1)	-1(1)
Ca21	23(2)	24(2)	24(2)	6(1)	3(1)	-1(1)
Ce1	20(1)	22(1)	11(1)	0	2(1)	0
Ce11	20(1)	22(1)	11(1)	0	2(1)	0
Ce2	17(1)	17(1)	12(1)	0(1)	2(1)	-1(1)
Ce21	17(1)	17(1)	12(1)	0(1)	2(1)	-1(1)
Ca1	29(3)	17(2)	16(2)	4(2)	7(2)	0(2)
Ca11	29(3)	17(2)	16(2)	4(2)	7(2)	0(2)
Ca2	19(2)	28(2)	15(2)	5(1)	2(1)	-2(1)
Ca21	19(2)	28(2)	15(2)	5(1)	2(1)	-2(1)
Ce1	26(1)	23(1)	17(1)	0	6(1)	0
Ce11	26(1)	23(1)	17(1)	0	6(1)	0
Ce2	21(1)	24(1)	18(1)	0(1)	6(1)	0(1)
Ce21	21(1)	24(1)	18(1)	0(1)	6(1)	0(1)
Ca1	40(3)	43(4)	23(3)	5(2)	11(2)	6(3)
Ca11	40(3)	43(4)	23(3)	5(2)	11(2)	6(3)
Ca2	22(2)	21(2)	24(2)	3(1)	6(1)	-6(2)
Ca21	22(2)	21(2)	24(2)	3(1)	6(1)	-6(2)

5.3.2.Microstructure: SEM-EDS and Raman spectroscopy

As previously shown in Chapter 4, SEM-EDS analysis of synchysite-(Ce) (Table 5.6) reveals a distinct core-rim chemical zoning with three different areas: i) a core enriched in Ce, La and Nd; ii) a rim enriched in Y and iii) an outer rim enriched in Th (Fig. 5.3a). Moreover, micro-inclusions of hematite (confirmed by Raman spectroscopy) and thorite ($ThSiO_4$) were detected at the rim. The Ca-content and the Ca/(Ca+REE) ratio are very close to the ideal values for synchysite, i.e. 1.00 a.p.f.u. and 0.50, respectively, suggesting very low polysomatic disorder. The amount of F, significantly below the ideal value of 1 a.p.f.u., is probably due to diffusion of this element under the highly focused electron beam.

Table 5.6. SEM-EDS analyses of synchysite-(Ce) major elements (averaged spot analysis in bracket) and related standard deviations (std).

	core (FCN2)		rim (FCN2)		core (FCN3)		rim (FCN3)		outer rim (FCN3)	
	mean (10)	std	mean (6)	std	mean (13)	std	mean (3)	std	mean (11)	std
F	0.76	0.07	0.64	0.16	0.51	0.09	0.86	0.11	0.80	0.25
Ca	1.02	0.01	1.06	0.02	0.99	0.01	1.00	0.01	1.03	0.02
Fe	0.00	0.00	0.02	0.01	0.01	0.00	0.03	0.00	0.03	0.01
Y	0.05	0.02	0.11	0.01	0.04	0.01	0.24	0.01	0.23	0.03
La	0.19	0.01	0.11	0.01	0.10	0.01	0.11	0.00	0.06	0.00
Ce	0.45	0.01	0.33	0.01	0.44	0.02	0.36	0.01	0.30	0.01
Pr	0.05	0.00	0.04	0.00	0.07	0.00	0.04	0.00	0.04	0.00
Nd	0.18	0.02	0.18	0.01	0.26	0.01	0.17	0.00	0.16	0.01
Sm	0.03	0.01	0.05	0.00	0.06	0.02	0.04	0.00	0.04	0.00
Gd	0.02	0.00	0.04	0.00	0.03	0.00	0.04	0.00	0.04	0.00
Th	0.00	0.00	0.07	0.01	0.01	0.00	0.01	0.00	0.08	0.02
Si	0.01	0.00	0.01	0.00	0.01	0.01	0.01	0.01	0.01	0.01
Al	0.00	0.00	0.02	0.03	0.00	0.00	0.00	0.00	0.00	0.00
∑REE	0.98		0.94		1.01		1.00		0.97	
Ca/(Ca+REE)*	0.51		0.53		0.50		0.50		0.52	

*Analyses with Fe content higher than 0.03 a.p.f.u., especially present at the rim, were interpreted as contaminated by hematite and excluded from the average.

Raman identification of CRFC was done looking at the symmetric stretching vibration of the carbonate group $v_1(CO_3)$, since it is diagnostic of the different polysomes of the bastnäsite-synchysite series. Indeed, the number of bands and their heights ratio vary according to the Ca/(Ca+REE) content and the resulting type of CO_3-layers, i.e. if located between two REE-layers or between one REE- and one CaF-layer. The number of bands is one for bastnäsite, two for synchysite and three for intermediate polysomes (see Chapter 3; Conconi et al. 2023a). The Raman spectra collected show that the $v_1(CO_3)$ symmetric stretching vibration has two bands at 1082 and 1099 cm^{-1}, suggesting synchysite (Fig. 5.3c).

It is well known that Raman spectroscopy is sensitive to the degree of metamictization, as demonstrated, for instance, in zircon (Nasdala et al., 1995) and in titanite (Heller et al., 2019). In the case of the studied CRFC, we found that spectra collected along different core-rim transects show differences in the shape of the $v_1(CO_3)$ stretching vibration bands. In particular, moving towards the rim, the bands become broader and the relative heights between the two bands also change (Fig. 5.3f). This evidence, linked to the greater background noise that

characterise the data collected at the rim, suggest a reduction of crystallinity at the rim compared to the core, probably due to metamictic damage caused by α-decay of Th.

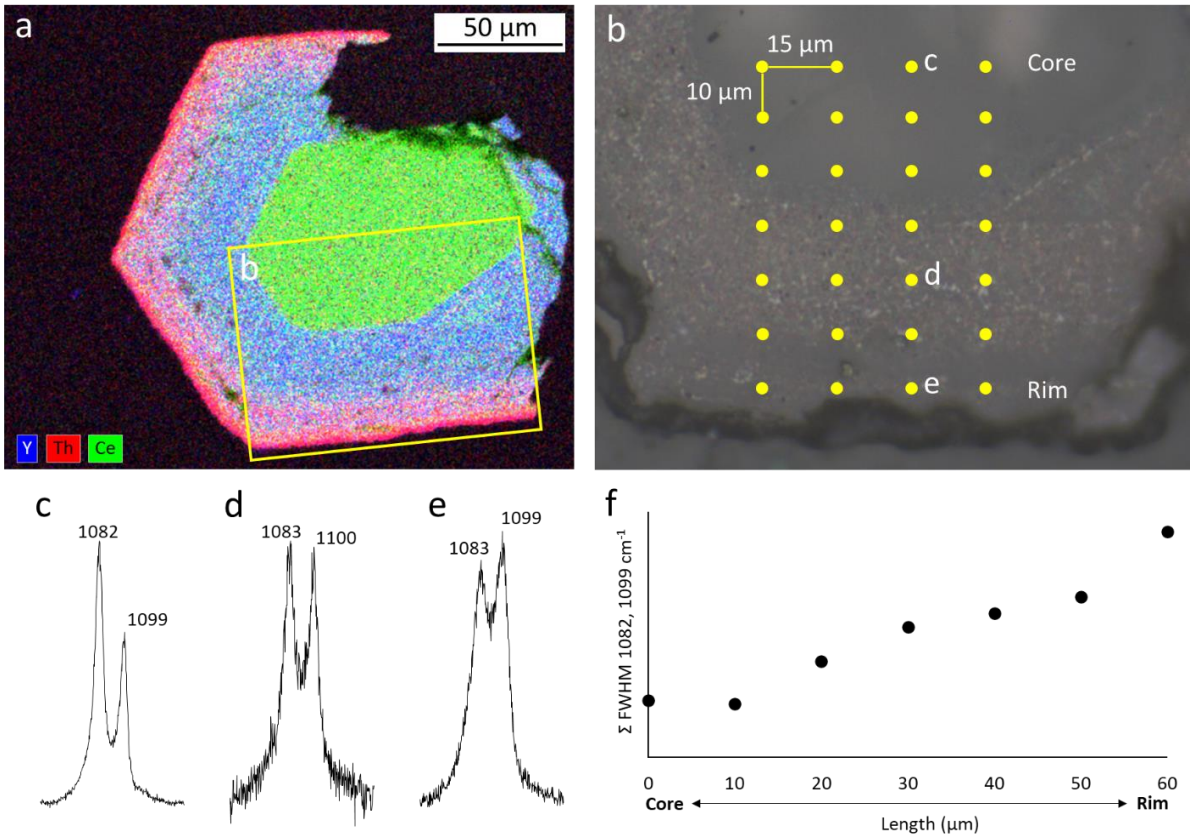

Figure 5.3. Sample FCBN3. (a) SEM-EDS map showing the chemical zoning and the area where Raman analysis was performed (yellow square). (b) Optical micrograph showing the points where Raman spectra were collected. (c, d and e) Raman spectra of the symmetric stretching vibration of the carbonate group $\nu_1(CO_3)$ collected at the centre (Ce-rich) in the rim (Y-rich) and in the outer rim (Th-rich), respectively. Note how bands broaden approaching the rim. Indeed, the sum of the full width at half maximum (FWHM) of the two bands increases from core to rim, suggesting metamictic damage induced by Th decay (f).

5.3.3 Nanostructure and local structure: TEM and 3DED

TEM observations on FIB lamellae revealed a complex nanostructure in the synchysite-(Ce) crystals. Indeed, stacking faults and solid and fluid inclusions were clearly visible in bright field images. Fluid inclusions appeared aligned along stacking faults and sometimes confined within major stacking faults (Fig. 5.4a, b). In contrast, solid inclusions, identified as hematite through EDS spectra and SAED patterns, were found as agglomerates of randomly oriented lamellar precipitates, ~200 nm in length. These hematite lamellae often cross-cut the stacking faults and fluid inclusion alignments at right angles, making them roughly parallel to **c***.

SAED patterns taken along <130> appear perfectly ordered, however rotating the crystal by 30° around **c***, the corresponding <110> patterns show *hhl* rows with $h \neq 3n$ affected by diffuse streaks (Fig. 5.4d). This pattern is typical of polytypic disorder. Interestingly, what initially appeared as continuous streaking at low camera lengths, once observed at higher camera lengths (higher magnification) showed a certain regularity in intensity modulation, suggesting a kind of superstructural order with periodicity of ~93 Å. Not surprisingly, this value is

commensurate with the synchysite quarter-cell (~4.6 Å), whose diffraction spots appeared strengthened on the diffraction pattern (Fig. 5.4e).

TEM-EDS analyses are reported in Table 5.7. Although they cannot be directly compared with SEM-EDS analyses because they were acquired from a different crystal (FCBN5) and quantified using a different method (standardless), they confirm the chemical zoning detected by SEM-EDS and the relative REE abundances. The REE sum (up to 1.04 a.p.fu.) and the Ca/(Ca+REE) ratio (0.45-0.48), which are slightly different from the ideal values of 1.00 and 0.50, respectively, are within the experimental error range of the TEM-EDS analysis. However, the presence of Ca-free bastnäsite-like lamellae along the long-range sequence cannot be entirely excluded.

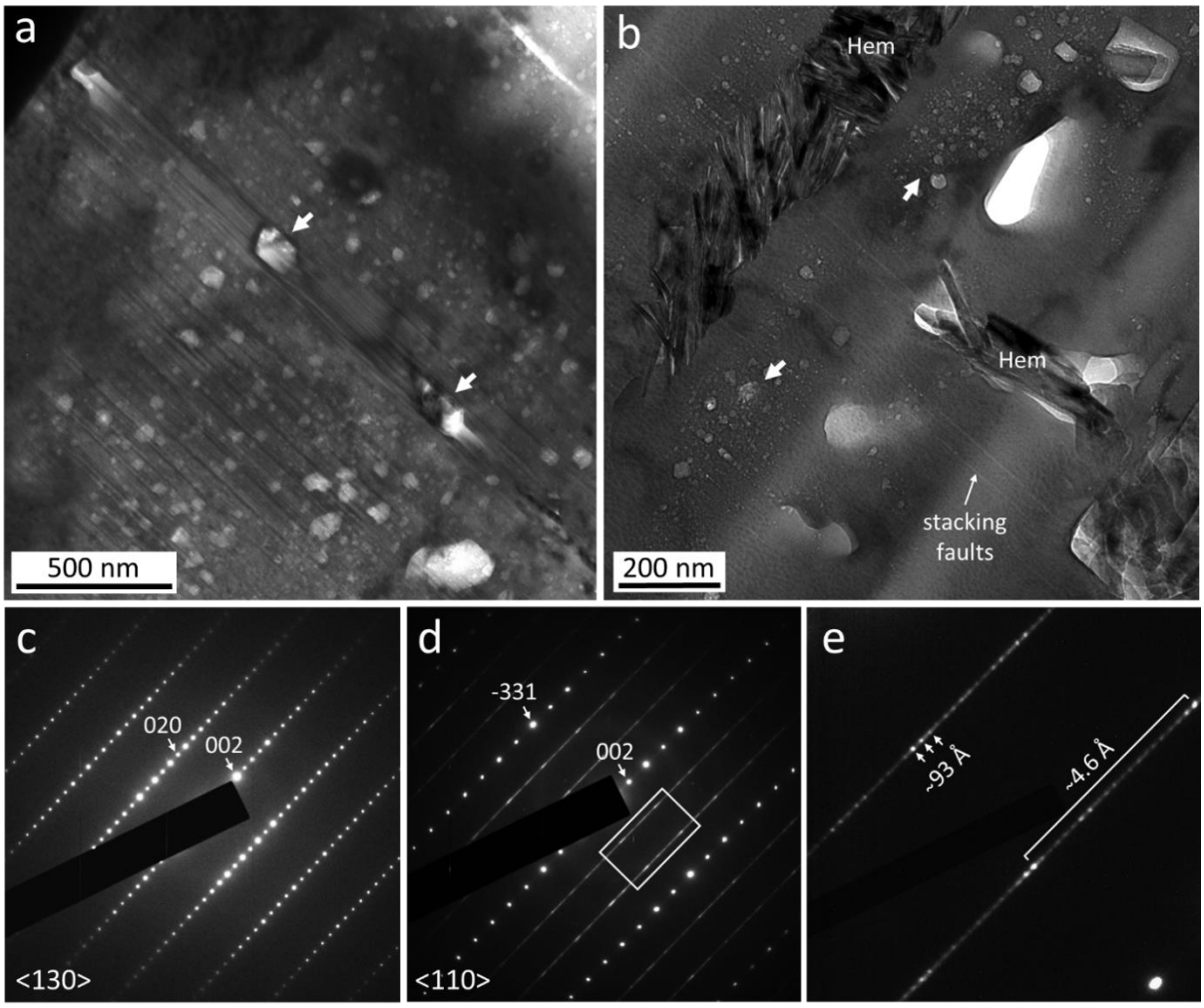

Figure 5.4. a) and (b) BF images showing stacking faults, fluid inclusions (arrows) and hematite (Hem) nano-crystals. c) SAED pattern seen down <130> and (d) down <110>. Note the streaking along *hhl* rows with $h \neq 3n$, indicating polytypic disorder. At longer camera lengths (higher magnification), what appears as a continuous streak in (d) reveals a supercell periodicity of ~93 Å (e).

Table 5.7. TEM-EDS analyses (a.p.f.u.) of Ce-rich core, Y-rich rim and Th-rich outer rim areas of the synchysite sample (FCN5). Standard deviations (std) in brackets.

	Thin foil 1				Thin foil 2			
	Ce-rich core		Y-rich rim		Y-rich rim		Th-rich outer rim	
	mean(5)	std	mean(4)	std	mean(8)	std	mean(5)	std
F	0.86	0.08	1.06	0.07	0.83	0.12	0.90	0.18
Ca	0.85	0.08	0.95	0.03	0.91	0.03	0.89	0.03
Y	0.07	0.02	0.18	0.03	0.18	0.06	0.14	0.03
La	0.12	0.01	0.12	0.03	0.12	0.02	0.13	0.03
Ce	0.42	0.04	0.38	0.05	0.35	0.02	0.37	0.04
Pr	0.05	0.01	0.04	0.01	0.03	0.01	0.03	0.01
Nd	0.28	0.02	0.21	0.01	0.21	0.01	0.20	0.02
Sm	0.06	0.01	0.04	0.01	0.04	0.01	0.04	0.01
Gd	0.03	0.01	0.03	0.01	0.03	0.01	0.03	0.01
Th	0.01	0.01	0.02	0.02	0.03	0.01	0.08	0.04
Σ_{REE}	1.04	0.07	1.03	0.02	0.99	0.03	1.01	0.06
X_{Ca}	0.45	0.04	0.48	0.01	0.48	0.01	0.47	0.02

X_{Ca} = Ca/(Ca+REE).

The lower crystallinity of the Th-rich outer rim of synchysite, compared to the innermost Th-poor areas detected by Raman spectroscopy, was confirmed by TEM. In Figure 5.5, SAED patterns taken along <130> from both the Th-rich and Th-poor areas are compared. Assuming that the beam damage induced by FIB operations and the thickness are constant across the boundary, the observed larger FWHM and lower peak to background ratio of the Th-rich area may be attributed to its lower crystallinity, due to the α-decay of Th.

Ten 3DED data collections were obtained from two lamellae extracted from the FCBN5 sample. The best of these (n. 7, from the Ce-rich core) in terms of R_{int} and provisional R-factors was selected for dynamical structural refinement. Relevant crystallographic and collection data are reported in Table 5.2 and bond length distances in Table 5.3, respectively, along with data from Wang et al. (1994) and from the SCXRD study for comparison. The general R-indexes are significantly worse compared to both the SCXRD indexes and those of Wang et al. (1994). Along the same lines, the bond geometry, obtained by imposing soft restraints for C-O bonds, angles and constraining the CO_3 groups to be planar, is slightly worse, though still within acceptable limits (e.g., Ca1-O2 = 2.99(2) Å). The refined 3DED cell parameters and volume are slightly larger than those refined by SXCRD data, but the difference is well within the error affecting TEM data (~2-3%), unless the latter are acquired without an internal standard (e.g., Capitani et al., 2016). The larger volume resulting from 3DED data and the much higher (unreliable) electron density refined with SCXRD lead to a density calculated from 3DED data

(3.915 g/cm^3) that is lower than for SCXRD data (4.463-4.640 g/cm^3), but more closely approaches the actual density.

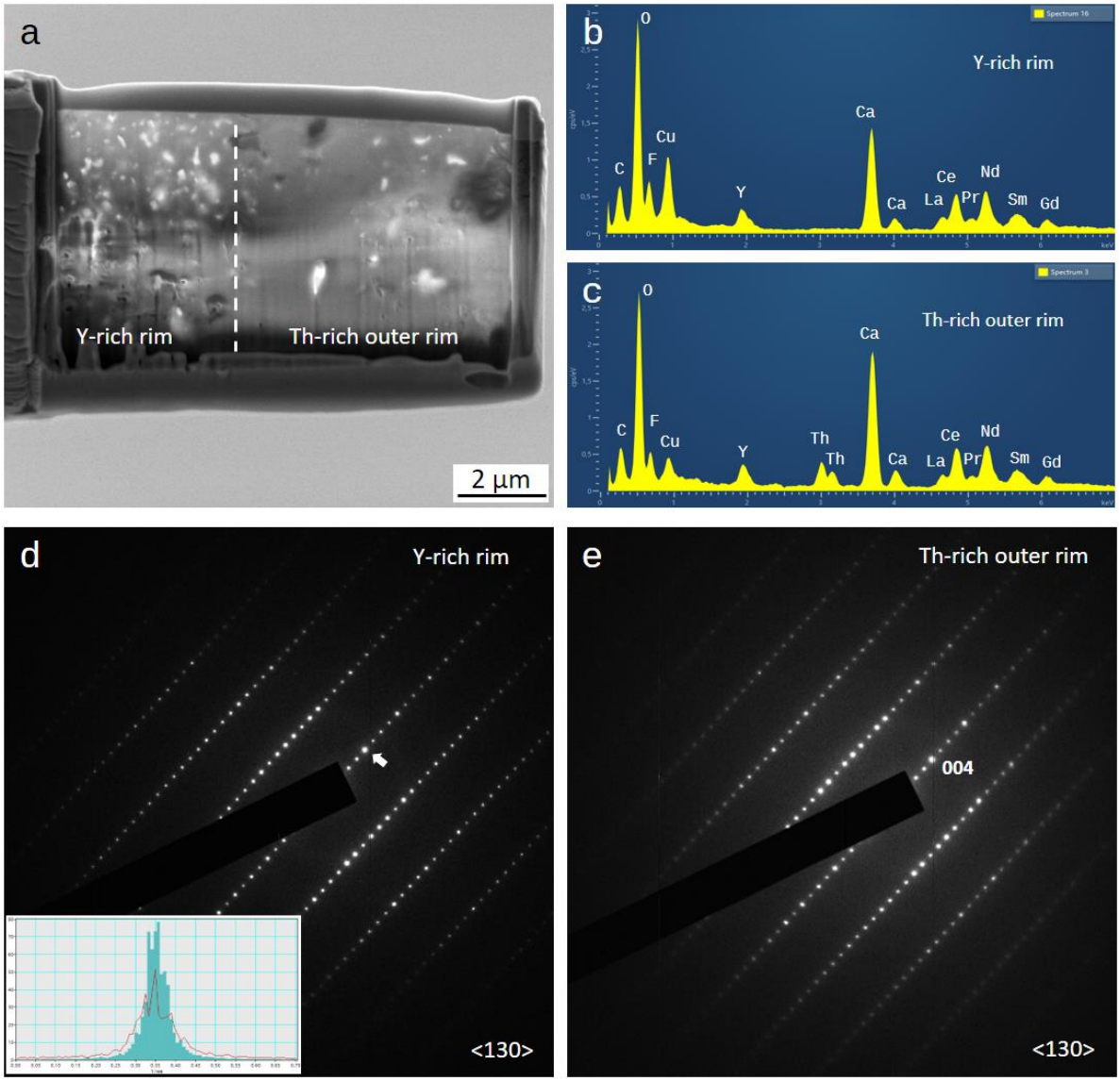

Figure 5.5. Sample FCBN5. (a) Low magnification TEM image of the thin foil (TF02) extracted halfway between the Y-rich rim and the Th-rich outer rim of the sample. The dashed line approximately indicates the boundary. (b) EDS spectrum taken from the Y-rich area and (c) from the Th-rich area. (d) SAED pattern along <130> taken in the Y-rich area and (e) in the Th-rich area. Inset in (d) are line scan profiles across the 004 spot: cyan filled profile from the Y-rich area; red line profile from the Th-rich area. Note the larger FWHM of the latter and the lower peak to background ratio.

5.4 Discussion and Conclusions

Synchysite crystals are often affected by polytypic disorder. The structure of synchysite can be described as alternating (001) $CaCe(CO_3)_2F$ half-cells (~9 Å thick each, resulting in the ~18.6 Å *c* parameter), systematically shifted on (001) along [-110] and [-1-10] by *a*/3. The stacking vectors, when projected onto the (001) plane, are therefore related by +60° and –60° rotations (Wang et al., 1994; Capitani, 2020). However, shifts along [010] and [-1-10] (or random ±60° rotations) are also possible, leading to polytypic disorder. This disorder does not affect the Ca

and Ce atoms, which maintain their sub-hexagonal symmetry, while the C and F atoms remain aligned along **c***, although in a random sequence. As for the CO_3 groups, they exhibit random in-plane orientations (Fig. 5.6). This observation may explain the distortion of the CO_3 polyhedra in the average structure obtained by SCXRD. On the other hand, the high deviation from the expected values of the electron density at the Ca and Ce sites cannot be easily explained, except by invoking an indirect effect of polytypic disorder and other defects on the overall data quality and consequently on site occupancy.

In addition to polytypic disorder, the studied synchysite crystals show other types of microstructural defects and inhomogeneities, such as chemical zoning, hematite inclusions and fluid inclusions. Chemical zoning, apart from causing local variations in the scattering power and X-ray absorption, also leads to partial metamictization of the structure in areas with high concentrations of Th, as demonstrated by Raman spectroscopy and SAED, resulting in inelastic scattering. Similarly, solid and fluid inclusions contribute to local variations in scattering and X-rays absorption, with the latter also causing inelastic scattering. Together these defects degrade the peak to background ratio, reduce the reliability of the measured intensities and lower the overall data quality. Despite the significant deviation from an ideal crystal, the structural refinements obtained are surprisingly good and may contribute to the limited crystal structure database for CRFC.

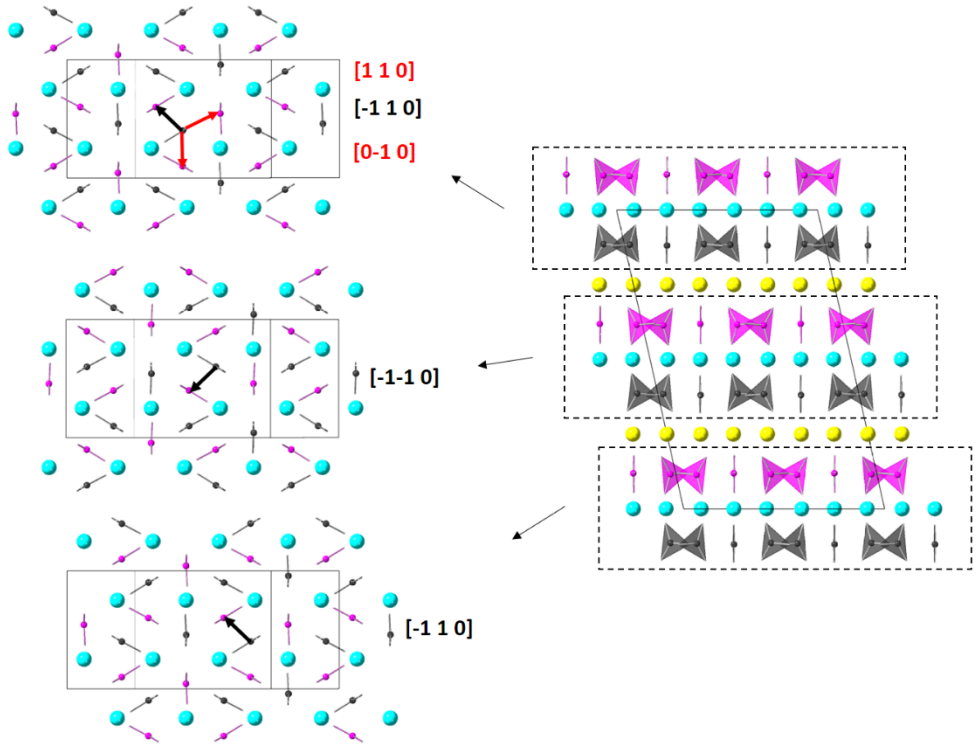

Figure 5.6. Structure of synchysite as seen along [001]* (left) and along [010] (right). Figures on the left correspond to the dashed portion on the right. Operating stacking vectors in ordered synchysite are indicated in black; additional allowed stacking vectors operating in disordered synchysite in red (grey and violet = CO_3 polyhedra; sky blue = Ca; yellow = Ce; F atoms are omitted for clarity).

Chapter 4 described a variety of CRFC with different morphologies and compositions from the Red Porphyry of Cuasso al Monte, including the synchysite-(Ce) hexagonal prisms studied here. These minerals are believed to have formed sequentially from a hydrothermal fluid as temperature decreased and fluid fractionation occurred, within a temperature range between 350°C and 100°C, with synchysite-(Ce) being the first to form. The microstructure described in this chapter provides additional insights into the crystal growth conditions of synchysite-(Ce) from Cuasso al Monte.

What initially appears to be a polytypic disordered structure, might actually be a superstructure with ~93 Å periodicity. If this is the case, it cannot have a thermodynamic stability field and must have formed through a screw dislocation mechanism, as has been suggested for long-range polytypes of micas (Pandey et al., 1982) and moissanite (Pandey and Krishna, 1975).

However, growth by screw dislocation is incompatible with the zoning observed under the optical microscope (Fig. 5.1). Growth through screw dislocation proceeds from the core to the rim and from bottom to top, making it incapable of forming the sharp chemical boundary between the core and rim observed in this synchysite-(Ce). Thus, it is plausible that the core initially grew via a screw dislocation mechanism. Subsequently, the crystals likely underwent a second stage of growth on the outer faces of the core from a liquid enriched in Y. This was followed by a diffusive exchange or substitution of REE by Th in the outer rim. Indeed, the gradual increase in Th in the Y-rich rim towards the surface of the crystal is pointing to a diffusive exchange. Moreover, TEM observations reveal that fluid inclusions are concentrated at the crystal rims, suggesting that the later stages of crystallization occurred from a more dilute, aqueous, Y-rich solution. Finally, hematite inclusions crosscut polytypic faults, indicating that they filled voids or fractures formed after crystallization.

The reliability of electron diffraction intensities may be partially compromised by dynamical effects and the excitation error (i.e. reflections measured out of their exact Bragg conditions), which lead to underestimated intensities. However, these issues are mostly mitigated by precession and dynamical refinement (Palatinus et al., 2015; Gemmi and Lanza, 2019). For synchysite-(Ce), 3DED data refinement converged to a reasonable model only after the CO_3 geometry was restrained and constrained. Even so, at least one unreliable value for the Ca-O distance was observed. The model obtained by SCXRD data appears more reliable than that from 3DED data, both in terms of R-indices and bond geometry. However, other factors should be considered. First, diffuse scattering is very strong even in electron diffraction data. In this case, few defects may have an enormous impact on diffraction data obtained from a volume of ~2 x 10^5 nm^3 (Mugnaioli and Gorelik, 2019). Moreover, synchysite contains heavy elements, such as lanthanides and actinides mixed with light elements such as C and O, which may lead to uncompensated absorption effects. Indeed, 3DED data reduction does not include absorption correction, as the sample is generally considered too thin for absorption to be significant. However, this may not be the true for FIB lamellae, where the thickness increases significantly at high tilt angles.

Chapter 6
Conclusions

In the present study, CRFC belonging to the bastnäsite-synchysite series were investigated to establish a relationship between their micro- and nano-structure and the genetic mechanisms driving their crystallization. A multimethodological approach was employed, using various analytical techniques, including SEM-EDS, EBSD, Raman spectroscopy, TEM-EDS, 3DED, and SCXRD.

Initially, a roadmap for identifying CRFC polysomes was developed. The results demonstrate that Raman spectroscopy effectively distinguishes CRFC members based on the symmetric $v_1(CO_3)$ stretching vibration of the carbonate group (CO_3^{2-}). Specifically, the end-members, bastnäsite and synchysite, are readily differentiated from intermediate polysomes by their distinctive Raman bands: bastnäsite shows a band at 1095 cm^{-1}, while synchysite displays two bands at 1081 cm^{-1} and 1099 cm^{-1}. Intermediate terms, such as parisite, present three bands at approximately 1081 cm^{-1}, 1091-1095 cm^{-1}, and 1099 cm^{-1}, varying in relative intensity. Although Raman spectroscopy can effectively determine the Ca/(Ca+REE) ratio in CRFC, it may not be suitable for distinguishing between ordered and disordered intergrowths with similar composition. For this reason, TEM-EDS remains the ultimate technique for polysome identification. However, also TEM has its own intricacies. Since most high resolution TEMs have a limited tilt range, the sample needs to be pre-oriented before preparation; for this purpose EBSD can be very useful. Indeed, EBSD can easily distinguish CRFC among other phases and correctly provides their orientation relationship, but under routine application, it fails to distinguish among different polysomes.

The micro- and nano-scale analysis revealed diverse structures among the CRFC samples, which can provide insights into the mechanisms responsible for their crystallization. In Mount Malosa CRFC (Chapter 3), the most common microstructure is rhythmic parisite-bastnäsite intergrowths alongside with a number of more or less ordered intermediate polysomes. The observed microstructure indicates a primary growth mechanism where CRFC crystallized from a fluid near thermodynamic equilibrium, with conditions repeatedly crossing the parisite–bastnäsite stability boundary. This suggests that crystallization may induce rhythmic changes in fluid composition. Indeed, an increase in $a(CO_3)^{2-}$ (or aF^-, or both) in the fluid would cause the crystallization of parisite at the expenses of bastnäsite. The protracting of this situation, would result in an increase in $aREE^{3+}$ in the remaining fluid, thus creating conditions favourable for the crystallization of bastnäsite (or other polysomes with lower Ca content than parisite). In other words, the crystallization process itself may induce rhythmic changes in fluid composition at the crystallization front, leading to syntactic intergrowths.

On the other hand, in Cuasso al Monte (Chapter 4 and 5), the CRFC occur in three different morphologies: i) rosette-like aggregates formed by hexagonal lamellae: ii) hexagonal prisms aggregates and iii) blocky subhedral aggregates. The rosette-like aggregates consist of either synchysite-(Ce) or bastnäsite-(Nd). Synchysite-(Ce) has a nanostructure where rosette-like "petals" are single crystals, while bastnäsite-(Nd) shows a complex nanostructure made of an intergrowth of bastnäsite, hematite and phyllosilicates nanocrystals. The hexagonal prism aggregates are synchysite-(Ce), showing a core-rim zoning. The zoning concerns the distribution of Ce, La, Nd, Y and Th, with the rim enriched in Y and the outer rim in Th and both depleted in Ce, La and Nd compared to the core. Micro-inclusions of Fe-oxides and thorite

were detected at the rim. Moreover, TEM analysis suggests a possible new synchysite-(Ce) polytype with a ~93 Å **c**-parameter. Lastly, the blocky subhedral aggregates are bastnäsite-(Ce) with no notable micro- or nano-structure. Overall, these evidences suggest the following crystallization sequence: (i) synchysite-(Ce) prisms formed early from a Ca- and F-rich fluid, at relatively low cooling rate; (ii) the Ca-depleted fluid then reached the condition to form blocky bastnäsite-(Ce), still at relatively low cooling rates; (iii) the fluid reached again, at slightly lower temperatures, supersaturation conditions for Ca and Ce, crystallizing rosette-like synchysite-(Ce). Indeed, so many "petals" of synchysite-(Ce) may represent fast nucleation events under a relatively high cooling rate that resulted into undeveloped prisms; (iv) the remaining fluid depleted in Ca and Ce and at low temperature, crystallized rosette-like bastnäsite-(Nd). Furthermore, the nanostructure of rosette-like bastnäsite-(Nd) and hexagonal prism synchysite-(Ce) suggests specific growth mechanisms. The former resembles REE-nanoparticle aggregate precursors observed in experimental syntheses of REE-carbonates, possibly representing the final morphology after rapid nucleation in a supersaturated solution under low temperature and high cooling rates. On the other hand, hexagonal prism synchysite-(Ce) displays a periodicity of ~93 Å along the **c**-axis, indicating that may be a new long range polytype of synchysite-(Ce); this implies a potential screw dislocation growth mechanism, similar to those seen in long range polytypes of mica and moissanite. TEM observations also reveal fluid inclusions concentrated at crystal rims, suggesting late-stage crystallization from a more diluted, Th- and Y-rich solution.

In conclusion, this study highlights that advancements in imaging and analytical techniques have enabled the acquisition of chemical and structural information with exceptional spatial resolution, which is crucial for fully characterizing the material under analysis. Indeed, information obtained from the micro- to the nano-scale has proven important in explaining macro-scale process, such as crystallization and elements partitioning. Understanding these processes is of paramount importance, especially considering that CRFC are the primary ore for REE.

References

Adler, H.H., Kerr, P.F., 1963. Infrared spectra, symmetry and structure relations of some carbonate minerals. American Mineralogist 48, 839–853.

Bakos, F., Del Moro, A., Visona, D., 1990. The Hercynian volcano-phitonic association of Ganna (Lake Lugano, Central Southern Alps, Italy). European Journal of Mineralogy 2, 373–384. https://doi.org/10.1127/ejm/2/3/0373

Balaram, V., 2019. Rare earth elements: A review of applications, occurrence, exploration, analysis, recycling, and environmental impact. Geoscience Frontiers 10, 1285–1303. https://doi.org/10.1016/j.gsf.2018.12.005

Baronnet, A., 1992. Chapter 7. Polytypism and stacking disorder. In: Minerals and Reactions at the Atomic Scale: Transmission Electron Microscopy, ed. Peter R. Buseck, Berlin, Boston: De Gruyter, 231-288. https://doi.org/10.1515/9781501509735-011

Boriani, A., Burlini, L., Caironi, V., Giobbi Origoni, E., Sassi, A., Sesana, E., 1988. Geological and petrological studies on the Hercynian plutonism of Serie dei Laghi - Geologic map of its occurrence between Valsesia and Lago Maggiore (N-Italy). Rendiconti Società Italiana Mineralogia Petrologia 43, 367-384.

Bourdelle, F., 2021. Low-Temperature Chlorite Geothermometry and Related Recent Analytical Advances: A Review. Minerals 11, 130. https://doi.org/10.3390/min11020130

Burla, M.C., Caliandro, R., Carrozzini, B., Cascarano, G.L., Cuocci, C., Giacovazzo, C., Mallamo, M., Mazzone, A,. Polidori, G., 2015. Crystal structure determination and refinement via SIR2014, Journal of Applied Crystallography 48, 306–309, https://doi.org/10.1107/S1600576715001132

Buseck, P.R., 1992, Minerals and Reactions At the Atomic scale: Transmission Electron Microscopy. Mineralogical Society of America. Reviews in Mineralogy 27.

Buseck, P.R., Self, P., 1992. Electron energy loss spectrometry (EELS) and electron channelling (ALCHEMI). Minerals and Reactions At the Atomic scale: Transmission electron Microscopy, Mineralogical Society of America, 141–180. Reviews in Mineralogy 27.

Buzgar, N., Apopei, A.I., 2009. The Raman study of certain carbonates. Geologie 55, 97–112.

Capitani, G., Mellini, M., 2000a. Crystallization sequence of the Campiglia M.ma skarn. Neues Jahrbuch für Mineralogie 3, 97–115.

Capitani, G., Mellini, M., 2000b. The johannsenite-hedenbergite complete solid solution: clinopyroxenes from the Campiglia Marittima skarn. European Journal of Mineralogy 12, 1215–1227. https://doi.org/10.1127/0935-1221/2000/0012-1215

Capitani, G., Grobety, B., Mellini, M., 2000c Growth twinning in johannsenite-hedenbergite clinopyroxenes. Neues Jahrbuch für Mineralogie 12, 543–555.

Capitani, G., Doukhan, J.C., Malcherek, T., Carpenter, M., 2002. Early partial melting in annealed natural cordierites. European Journal of Mineralogy 14, 879–890, https://doi.org/ 10.1127/0935-1221/2002/0014-0879.

Capitani, G., Mellini, M., 2006. The crystal structure of a second antigorite polysome (m=16), by single-crystal synchrotron diffraction. American Mineralogist 91, 394–399, https://doi.org/10.2138/am.2006.1919.

Capitani, G., Mugnaioli, E., Guastoni, A., 2016. What is the actual structure of samarskite-(Y)? A TEM investigation of metamict samarskite from the garnet codera dike pegmatite (Central Italian Alps). American Mineralogist 101, 1679-1690. https://doi.org/10.2138/am-2016-5605

Capitani, G., Mugnaioli, E., Gentile, P., 2018. Submicrometer yttrian zircon coating and arborescent aeschynite microcrystals on truncated bipyramidal anatase: An electron microscopy study of miarolitic cavities in the Cuasso al Monte granophyre (Varese, Italy). American Mineralogist 103, 480–488. https://doi.org/10.2138/am-2018-6242

Capitani, G., 2019. HRTEM investigation of bastnäsite–parisite intergrowths from Mount Malosa (Malawi): ordered sequences, polysomatic faults, polytypic disorder, and a new parisite-(Ce) polymorph. European Journal of Mineralogy 31, 429–442. https://doi.org/10.1127/ejm/2019/0031-2824

Capitani, G., 2020. Synchysite-(Ce) from Cinquevalli (Trento, Italy): Stacking Disorder and the Polytypism of (Ca,REE)-Fluorcarbonates. Minerals 10, 77. https://doi.org/10.3390/min10010077

Castaing, R., 1951. Application of Electron Probes to Metallographic Analysis. University of Paris, Ph.D. dissertation.

Ciobanu, C., Kontonikas-Charos, A., Slattery, A., Cook, N., Wade, B., Ehrig, K., 2017. Short-Range Stacking Disorder in Mixed-Layer Compounds: A HAADF STEM Study of Bastnäsite-Parisite Intergrowths. Minerals 7, 227. https://doi.org/10.3390/min7110227

Ciobanu, C.L., Cook, N.J., Slattery, A.D., Ehrig, K., Liu, W.Y., 2022. Nanoscale intergrowths in the bastnäsite–synchysite series record transition toward thermodynamic equilibrium. MRS Bulletin 47, 250–257. https://doi.org/10.1557/s43577-022-00318-1

Cliff, G., Lorimer, G.W., 1975. The quantitative analysis of thin specimens. Journal of Microscopy 103, 203–207. https://doi.org/10.1111/j.1365-2818.1975.tb03895.x.

Conconi, R., Fumagalli, P., Capitani, G., 2023a. A multi-methodological study of the bastnäsite-synchysite polysomatic series: Tips and tricks of polysome identification and the origin of syntactic intergrowths. American Mineralogist 108, 1658–1668. https://doi.org/10.2138/am-2022-8678

Conconi, R., Ventruti, G., Nieto, F., Capitani, G., 2023b. TEM-EDS microanalysis: Comparison among the standardless, Cliff & Lorimer and absorption correction

quantification methods. Ultramicroscopy 254, 113845. https://doi.org/10.1016/j.ultramic.2023.113845

Conconi, R., Abad Ortega, M. M., Nieto, F., Buono, P., Capitani, G., 2024a. TEM-EDS microanalysis: Comparison between different electron sources, accelerating voltages and detection systems. Ultramicroscopy (Under Review)

Conconi, R., Gentile, P., Fumagalli, P., Nieto, F., Capitani, G., 2024b. CaREE-fluorcarbonates: A variety of morphologies, compositions and nanostructures with insights into REE partitioning and mobility. Lithos (Under Review)

Conconi, R., Merlini, M., Fumagalli, P., Mugnaioli, E., Folco, L., Capitani, G., 2024c. Average Structure and Microstructure of Synchysite-(Ce) from Cuasso al Monte (Varese, Italy). European Journal of Mineralogy (Under Review)

Damen, T.C., Porto, S.P.S., Tell, B., 1966. Raman Effect in Zinc Oxide. Physical Review 142, 570–574. https://doi.org/10.1103/PhysRev.142.570.

Demartin, F., Minaglia, A., Gramaccioli, C.M., 2001. Characterization of gadolinite-group minerals using crystallographic data only: the case of hingganite-(y) from Cuasso al Monte, Italy. The Canadian Mineralogist 39, 1105–1114. https://doi.org/10.2113/gscanmin.39.4.1105

Dino, G.A., Cavallo, A., Rossetti, P., Garamvölgyi, E., Sándor, R., Coulon, F., 2020. Towards Sustainable Mining: Exploiting Raw Materials from Extractive Waste Facilities. Sustainability 2020, 2383. https://doi.org/10.3390/su12062383

Donnay, G., Donnay, J.D.H., 1953 The crystallography of bastnäsite, parisite, röntgenite and synchysite. American Mineralogist 38, 932–963

Eibl, O., 1993. New method for absorption correction in high-accuracy, quantitative EDX microanalysis in the TEM including low-energy X-ray lines. Ultramicroscopy 50, 179–188, https://doi.org/10.1016/0304-3991(93)90008-L.

Erkoyun, H., Kadir, S., 2011. Mineralogy, micromorphology, geochemistry and genesis of a hydrothermal kaolinite deposit and altered Miocene host volcanites in the Hallaçlar area, Uşak, western Turkey. Clay Minerals 46, 421–448. https://doi.org/10.1180/claymin.2011.046.3.421

European Commission, Directorate-General for Internal Market, Industry, Entrepreneurship and SMEs, Grohol, M., Veeh, C. (2023) Study on the critical raw materials for the EU 2023: final report. Publications Office of the European Union. https://data.europa.eu/doi/10.2873/725585

Fagnani, G., 1946. Il porfido quarzifero di Cavagnano (Porto Ceresio). Atti della Società Italiana di Scienze Naturali 85, 85-96.

Förster, H.-J., 2001. Synchysite-(Y)-synchysite-(Ce) solid solutions from Markersbach, Erzgebirge, Germany: REE and Th mobility during high-T alteration of highly

fractionated aluminous A-type granites. Mineralogy and Petrology 72, 259–280. https://doi.org/10.1007/s007100170019

Fregola, R.A., Capitani, G., Scandale, E., Ottolini, L., 2009. Chemical control of 3T stacking order in Li-poor biotite mica. American Mineralogist 94, 334–344, https://doi.org/ 10.2138/am.2009.3004.

Frost, R.L., Dickfos, M.J., 2007. Raman spectroscopy of halogen-containing carbonates. Journal of Raman Spectroscopy 38, 1516–1522. https://doi.org/ 10.1002/jrs.1806.

Fulignati, P., 2020. Clay Minerals in Hydrothermal Systems. Minerals 10, 919. https://doi.org/10.3390/min10100919

Gai, S., Li, C., Yang, P., Lin, J., 2014. Recent Progress in Rare Earth Micro/Nanocrystals: Soft Chemical Synthesis, Luminescent Properties, and Biomedical Applications. Chemical Reviews 114, 2343–2389. https://doi.org/10.1021/cr4001594

Gemmi, M., Lanza, A.E., 2019. 3D electron diffraction techniques. Acta Crystallographica B Structural Science Crystal Engineering and Materials 75, 495–504. https://doi.org/10.1107/S2052520619007510

Gemmi, M., Mugnaioli, E., Gorelik T.E., Kolb, U., Palatinus, L., Boullay, P., Hovmöller, S., Abrahams, J.P., 2019. 3D Electron Diffraction: The Nanocrystallography Revolution. ACS Central Science 5, 1315-1329. https://doi.org/10.1021/acscentsci.9b00394

Guastoni, A., Nestola, F., Giaretta, A., 2009. Mineral chemistry and alteration of rare earth element (REE) carbonates from alkaline pegmatites of Mount Malosa, Malawi. American Mineralogist 94, 1216–1222. https://doi.org/10.2138/am.2009.3185

Guastoni, A., Kondo, D., Nestola, F., 2010. Bastnäsite-(Ce) and Parisite-(Ce) From Mt. Malosa, Malawi. Gems & Gemology 46, 42–47. https://doi.org/10.5741/GEMS.46.1.42

Gysi, A.P., Williams-Jones, A.E., 2015. The thermodynamic properties of bastnäsite-(Ce) and parisite-(Ce). Chemical Geology 392, 87–101. https://doi.org/10.1016/j.chemgeo.2014.11.001

Grice, J.D., Maisonneuve, V., Leblanc, M., 2007. Natural and synthetic fluoride carbonates. Chemical Reviews 107, 114–132. https://doi.org/10.1021/cr050062d

Heinrich, K.F.J., Yakowitz, H., 1975. Absorption of primary X rays in electron probe microanalysis. Analytical Chemistry 47.

Heller, B., Lünsdorf, N., Dunkl, I., Molnár, F., Eynatten, H., 2019. Estimation of radiation damage in titanites using Raman spectroscopy. American Mineralogist 104, 857-868. https://doi.org/10.2138/am-2019-6681

Henderson, P., 1984. Rare earth element geochemistry. Elsevier.

Herrington, R., 2021. Mining our green future. Nature Reviews Materials 6, 456–458. https://doi.org/10.1038/s41578-021-00325-9

Horie, K., Tsutsumi, Y., Cho, M., Morishita, Y., Hidaka, H., 2010. Crystallization of REE minerals and redistribution of U, Th, and REE at contact boundary between granite and gabbro during hydrothermal alteration. Physics and Chemistry of the Earth 35, 284-291. https://doi.org/10.1016/j.pce.2010.03.035.

Horita, Z., Sano, T., Nemoto, M., 1987. Simplification of X-ray absorption correction in thin-sample quantitative microanalysis. Ultramicroscopy 21, 271–276, https://doi.org/10.1016/0304-3991(87)90152-5.

Kanazawa, Y., Kamitani, M., 2006. Rare earth minerals and resources in the world. Journal of Alloys and Compounds 408–412, 1339-1343, https://doi.org/10.1016/j.jallcom.2005.04.033.

Kaur, P., Chaudhri, N., Hofmann, A.W., Raczek, I., Okrusch, M., Skora, S., Baumgartner, L.P., 2012. Two-Stage, Extreme Albitization of A-type Granites from Rajasthan, NW India. Journal of Petrology 53, 919–948. https://doi.org/10.1093/petrology/egs003

Koto, K., Morimoto, N., Narita, H., 1976. Crystallographic relationships of the pyroxene and pyroxenoids. The Journal of the Japanese Association of Mineralogists 71, 248-254.

Kuebler, K., Wang, A., Freeman, J.J., Jolliff, B.L., 2006. Database of Raman mineral spectra for planetary surface exploration. In 37th Annual Lunar and Planetary Science Conference, 1907.

Liendo, F., Arduino, M., Deorsola, F.A., Bensaid, S., 2022. Factors controlling and influencing polymorphism, morphology and size of calcium carbonate synthesized through the carbonation route: A review. Powder Technology 398, 117050. https://doi.org/10.1016/j.powtec.2021.117050

Mariano, A.N., Mariano, A., 2012. Rare Earth Mining and Exploration in North America. Elements 8,369-376. https://doi.org/10.2113/gselements.8.5.369

Marumo, K., 1989. Genesis of kaolin minerals and pyrophyllite in Kuroko deposits of Japan: Implications for the origins of the hydrothermal fluids from mineralogical and stable isotope data. Geochimica and Cosmochimica Acta 53, 2915–2924. https://doi.org/10.1016/0016-7037(89)90168-3

Mellini, M., Menichini, R., 1985. Proportionality factors for thin film TEM/EDS microanalysis of silicate minerals. Rendiconti della Società Mineralogica Italiana 40, 261–266.

Meng, D., Wu, X., Mou, T., and Li, D., 2001a. Determination of six new polytypes in parisite-(Ce) by means of high-resolution electron microscopy. Mineralogical Magazine 65, 797–806 https://doi.org/10.1180/0026461016560010.

Meng, D., Wu, X., Mou, T., Li, D., 2001b. Microstructural investigation of new polytypes of parisite-(ce) by high-resolution transmission electron microscopy. Canadian Mineralogist 39, 1713–1724. https://doi.org/10.2113/gscanmin.39.6.1713

Meng, D., Wu, X., Han, Y., Meng, X., 2002. Polytypism and microstructures of the mixed-layer member B2S, CaCe3(CO3)4F3 in the bastnaesite-(Ce)–synchysite-(Ce) series. Earth and Planetary Science Letter 203, 817–828. https://doi.org/10.1016/S0012-821X(02)00947-0

Migdisov, A., Williams-Jones, A., 2002. A spectrophotometric study of neodymium(III) complexation in chloride solutions. Geochimica et Cosmochimica Acta 66, 4311–4323. https://doi.org/10.1016/S0016-7037(02)00995-X

Migdisov, A., Williams-Jones, A., 2007. An experimental study of the solubility and speciation of neodymium(III) fluoride in F-bearing aqueous solutions. Geochimica et Cosmochimica Acta 71, 3056–3069. https://doi.org/10.1016/j.gca.2007.04.004

Migdisov, A., Williams-Jones, A., Normand, C., Wood, S., 2008. A spectrophotometric study of samarium(III) speciation in chloride solutions at elevated temperatures. Geochimica et Cosmochimica Acta 72, 1611–1625. https://doi.org/10.1016/j.gca.2008.01.007

Migdisov, A., Williams-Jones, A., 2014. Hydrothermal transport and deposition of the rare earth elements by fluorine-bearing aqueous liquids. Mineralium Deposita 49, 987–997. https://doi.org/10.1007/s00126-014-0554-z

Migdisov, A., Williams-Jones, A. E., Brugger, J., Caporuscio, F. A., 2016. Hydrothermal transport, deposition, and fractionation of the REE: Experimental data and thermodynamic calculations. Chemical Geology 439, 13–42. https://doi.org/10.1016/j.chemgeo.2016.06.005

Mitchell, D.R., 2007. HRTEM filter. Digital Micrograph Script Database (ver. 2019.11.01) (Online). Available: http://www.dmscripting.com/hrtem_filter.html FELMI. Graz University of Technology, Austria.

Mugnaioli, E., Gemmi, M., 2018. Single-crystal analysis of nanodomains by electron diffraction tomography: mineralogy at the order-disorder borderline. Zeitschrift für Kristallographie 233, 163-178. https://doi.org/10.1515/zkri-2017-2130

Mugnaioli, E., Gorelik, T.E., 2019. Structure analysis of materials at the order-disorder borderline using three-dimensional electron diffraction. Acta Crystallographica B Structural Science Crystal Engineering and Materials 75, 550-563. https://doi.org/10.1107/S2052520619007339

Narita, H., Koto, K., Morimoto, M., 1977. The crystal structure of MnSiO3 polymorphs (rhodonite- and pyroxmangite-type). Mineralogical Journal 8, 329-342. https://doi.org/10.2465/MINERJ.8.329

Nasdala, L., Irmer, G., Wolf, D., 1996. The degree of metamictization in Zircons: a Raman spectroscopic study. European Journal of Mineralogy 7, 471-478. https://doi.org/10.1127/ejm/7/3/0471

Newbury, D.E., Swyt, C.R., Myklebust, R.L., 1995. ”Standardless” quantitative electron probe microanalysis with energy-dispersive X-ray spectrometry: is it worth the risk? Analytical Chemistry 67, 1866–1871.

Newbury, D.E. 1998. Standardless quantitative electron-excited X-ray microanalysis by energy-dispersive spectrometry: what is its proper role? Microscopy and Microanalysis 4, 585–597. https://doi.org/10.1017/S1431927698980564.

Newbury, D.E., Ritchie, N.W.M., 2013. Is scanning electron/energy dispersive X-ray spectrometry (SEM/EDS) quantitative? Scanning 35, 141–168. https://doi.org/10.1002/sca.21041.

Newbury, D.E., Ritchie, N.W.M., 2015. Performing elemental microanalysis with high accuracy and high precision by scanning electron microscopy/silicon drift detector energy-dispersive X-ray spectrometry (SEM/SDD-EDS). Journal of Material Science 50, 493–518. https://doi.org/10.1007/s10853-014-8685-2

Newbury, D.E., Ritchie, N.W.M., 2019. Electron-excited X-ray microanalysis by energy dispersive spectrometry at 50: analytical accuracy, precision, trace sensitivity and quantitative compositional mapping. Microscopy and Microanalysis 25, 1075–1105. https://doi.org/10.1017/S143192761901482X

Ngwenya, B., 1994. Hydrothermal rare earth mineralisation in carbonatites of the Tundulu complex, Malawi: Processes at the fluid/rock interface. Geochimica et Cosmochimica Acta 58, 2061–2072. https://doi.org/10.1016/0016-7037(94)90285-2

Nieto, F., Ortega-Huertas, M., Peacor, D., Arostegui, J., 1996. Evolution of illite/smectite from early diagenesis through incipient metamorphism in sediment of the BasqueCantabrian Basin, Clay and Clay Minerals 44, 304–323. https://doi.org/10.1346/CCMN.1996.0440302.

Nieto, F., Livi, K.J.T., Oberti, R., 2013. Minerals At the Nanoscale. EMU Notes in Mineralogy, Mineralogical Society of Great Britain and Ireland 14, London.

Ni, Y., Hughes, J.M., Mariano, A.N., 1993. The atomic arrangement of bastnasite-(Ce), Ce(CO3)F, and structural elements of synchysite-(Ce), rontgenite-(Ce), and parisite-(Ce). American Mineralogist 78, 415–418

Ni, Y., Post, J.E., Hughes, J.M., 2000. The crystal structure of parisite-(Ce), Ce2CaF2(CO3)3. American Mineralogist 85, 251–258. https://doi.org/10.2138/am-2000-0126

Palatinus, L., Petříček, V., Corrêa, C.A., 2015. Structure refinement using precession electron diffraction tomography and dynamical diffraction: theory and implementation. Acta Crystallographica Section A: Foundations and Advances 71, 235−244. https://doi.org/10.1107/S2053273315001266

Pandey, D., Krishna, P., 1975. Influence of stacking faults on the growth of polytype structures. II - Silicon carbide polytypes. Philosophical Magazine 31, 1133-1148. http://dx.doi.org/10.1080/00318087508226832

Pandey, D., Baronnet, A., Krishna, P., 1982).Influence of Stacking Faults on the Spiral Growth of Polytype Structures in Mica. Physics and Chemistry of Minerals 8, 268-278. https://doi.org/10.1007/BF00308248

Pearson, R., 1963. Hard and soft acids and bases. Journal of the American Chemical Society 85, 3533–3539. https://doi.org/10.1021/ja00905a001

Peiravi, M., Dehghani, F., Ackah, L., Baharlouei, A., Godbold, J., Liu, Jia., Mohanty, M., Ghosh, T., 2021. A Review of Rare-Earth Elements Extraction with Emphasis on Non-conventional Sources: Coal and Coal Byproducts, Iron Ore Tailings, Apatite, and Phosphate Byproducts. Mining, Metallurgy & Exploration 38, 1–26. https://doi.org/10.1007/s42461-020-00307-5

Petříček, V., Palatinus, L., Plášil, J., Dušek, M., 2023. Jana2020 – a new version of the crystallographic computing system Jana. Zeitschrift für Kristallographie - Crystalline Materials 238, 271–282. https://doi.org/10.1515/zkri-2023-0005

Pezzotta, F., Diella, V., Guastoni, A., 1999. Chemical and paragenetic data on gadolinite-group minerals from Baveno and Cuasso al Monte, southern Alps, Italy. American Mineralogist 84, 782–789. https://doi.org/10.2138/am-1999-5-612

Pezzotta, F., Diella, V., Guastoni, A., 2005. Scandium silicates from the Baveno and Cuasso al Monte NYF-granites, Southern Alps (Italy): Mineralogy and genetic inferences. American Mineralogist 90, 1442–1452. https://doi.org/10.2138/am.2005.1478

Pinarelli, L., Boriani, A., Del Moro, A., 1993. The Pb isotopic systematics during crustal contamination of subcrustal magmas: the Hercynian magmatism in the Serie dei Laghi (Southern Alps, Italy). Lithos 31, 51–61. https://doi.org/10.1016/0024-4937(93)90032-8

Pinarelli, L., Moro, A.D., Boriani, A., Caironi, V., 2002. Sr,Nd isotope evidence for an enriched mantle component in the origins of the Hercynian gabbro-granite series of the "'Serie dei Laghi'" (Southern Alps, NW Italy). European Journal of Mineralogy 14, 403–415. https://doi.org/10.1127/0935-1221/2002/0014-0403

Pouchou, J.L. and Pichoir, F. (1991) Quantitative Analysis of Homogeneous or Stratified Microvolumes Applying the Model "PAP". In: Heinrich, K.F.J. and Newbury, D.E., Eds., Electron Probe Quantification, Plenum Press, New York, 31-75. https://doi.org/10.1007/978-1-4899-2617-3_4

Powell, C.J., Heinrich, K.F.J., Newbury, D.E., Yakowitz, H., 1976. Evaluation of formulas for inner- shell ionization cross sections. Use of Monte Carlo Calculations in Electron Probe Microanalysis and Scanning Electron Microscopy, National Bureau of Standards Special Publication, Gaithersburg, MD.

Price, G.D., Yeomans, J., 1986. A model for polysomatism. Mineralogical Magazine 50, 149–156. https://doi.org/10.1017/minmag.1986.050.355.20.

Price, D.L., Butler, I.B., Ngwenya, B.T., Kirstein, L.A., McDermott, F., O'Neill, T., 2023. Crystallisation pathways of a mixed La Nd carbonate – Ambient temperature synthesis of the mineral lanthanite. Chemical Geology 617, 121265. https://doi.org/10.1016/j.chemgeo.2022.121265

Rodriguez-Blanco, J.D., Vallina, B., Blanco, J.A., Benning, L.G., 2014. The role of REE $^{3+}$ in the crystallization of lanthanites. Mineralogical Magazine 78, 1373–1380. https://doi.org/10.1180/minmag.2014.078.6.03

Rusk, B.G., Lowers, H.A., Reed, M.H., 2008. Trace elements in hydrothermal quartz: Relationships to cathodoluminescent textures and insights into vein formation. Geology 36, 547. https://doi.org/10.1130/G24580A.1

Salvi, S., Williams-Jones, A., 1996. The role of hydrothermal processes in concentrating high-field strength elements in the Strange Lake peralkaline complex, northeastern Canada. Geochimica et Cosmochimica Acta60, 1917–1932. https://doi.org/10.1016/0016-7037(96)00071-3

Sanità, E., Conconi, R., Lorenzon, S., Di Rosa, M., Capitani, G., Mugnaioli, E., 2024. Application of an improved TEM-EDS protocol based on charge balance for accurate chemical analysis of sub-micrometric phyllosilicates in low-grade metamorphic rocks. Clays and Clay Minerals 72, e31, https://doi.org/10.1017/cmn.2024.32.

Secco, L., Guastoni, A., Nestola, F., Redhammer, G.J., Dal Negro, A., 2007. Crystal chemistry of aegirine as indicator of P-T conditions. Mineralogical Magazine 71, 321, https://doi.org/10.1180/minmag.2007.071.3.321.

Sheldrick, G.M., 2015. Crystal structure refinement with SHELXL. Acta Crystallographica Section C Structural Chemistry 1, 3-8. https://doi.org/10.1107/S2053229614024218.

Sheridan, P.J., 1989 Determination of experimental and theoretical kAsifactors for a 200kV analytical electron microscope. Journal of Electron Microscopy Techniques 11, 41–61. https://doi.org/10.1002/jemt.1060110107

Szucs, A.M., Stavropoulou, A., O'Donnell, C., Davis, S., Rodriguez-Blanco, J.D., 2021. Reaction Pathways toward the Formation of Bastnäsite: Replacement of Calcite by Rare Earth Carbonates. Crystal Growth & Design 21, 512–527. https://doi.org/10.1021/acs.cgd.0c01313

Szucs, A.M., Maddin, M., Brien, D., Guyett, P.C., Rodriguez-Blanco, J.D., 2023. Targeted Crystallization of Rare Earth Carbonate Polymorphs at Hydrothermal Conditions via Mineral Replacement Reactions. Global Challenges 7, 2200085. https://doi.org/10.1002/gch2.202200085

Tazaki, K., 2005. Microbial Formation of a Halloysite-Like Mineral. Clays Clay Minerals 53, 224–233. https://doi.org/10.1346/CCMN.2005.0530303

Thompson, J.B., 1978. Biopyriboles and polysomatic series. American Mineralogist 63, 239–249.

Ungemach, H., 1935. Sur la syntaxie et al polytypie. Zeitschrift für Kristallographie 91, 1–22.

Vallina, B., Rodriguez-Blanco, J.D., Blanco, J.A., Benning, L.G., 2014. The effect of heating on the morphology of crystalline neodymium hydroxycarbonate, $NdCO_3OH$. Mineralogical Magazine 78, 1391–1397. https://doi.org/10.1180/minmag.2014.078.6.05

Van Cappellen, E., 1990. The parameterless correction method in X-ray microanalysis. Microscopy Microanalysis Microstructure 1, 1–22, https://doi.org/10.1051/mmm:01990001010100.

Van Cappellen, E., Doukhan, J.C., 1994. Quantitative transmission X-ray microanalysis of ionic compounds. Ultramicroscopy 53, 343–349.

Van Landuyt, J., Amelinckx, S., 1975. Multiple beam direct lattice imaging of new mixed-layer compounds of the bastnäsite-synchysite series. American Mineralogist 60, 351–358.

Veblen, D.R., Buseck, E.R., 1979. Chain-width order and disorder in biopyriboles. American Mineralogist 64, 687-700.

Veblen, D.R., 1991. Polysomatism and polysomatic series: A review and applications. American Mineralogist 76, 801–826.

Veblen, D. R., 1992. Chapter 6. Electron microscopy applied to nonstoichiometry, polysomatism and replacement reactions in minerals. In: Minerals and Reactions at the Atomic Scale: Transmission Electron Microscopy, ed. Peter R. Buseck, Berlin, Boston: De Gruyter, 181-230.

Vidal, O., Goffé, B., and Arndt, N., 2013. Metals for a low-carbon society. Nature Geoscience 6, 894–896. https://doi.org/10.1038/ngeo1993

Vignola, P., Hatert, F.D.R., Bersani, D., Diella, V., Gentile, P., Risplendente, A., 2012. Chukhrovite-(Ca), $Ca_{4.5}Al_2(SO_4)F_{13}\cdot 12H_2O$, a new mineral species from the Val Cavallizza Pb–Zn–(Ag) mine, Cuasso al Monte, Varese province, Italy. European Journal of Mineralogy 24, 1069-1076. 10.1127/0935-1221/2012/0024-2247.

Wang, L., Ni, Y., Hughes, J.M., Bayliss, P., Drexler, J.W., 1994. The atomic arrangement of synchysite-(Ce), CeCaF(CO3)2. Canadian Mineralogist 32, 865–871.

Wang, Z.-Y., Fan, H.-R., Zhou, L., Yang, K.-F., She, H.-D., 2020. Carbonatite-Related REE Deposits: An Overview. Minerals 10, 965. https://doi.org/10.3390/min10110965

Watanabe, M., Horita, Z., Nemoto, M., 1996. Absorption correction and thickness determination using ζ-factor in quantitative X-ray microanalysis. Ultramicroscopy 65, 187–198, https://doi.org/10.1016/S0304-3991(96)00070-8.

Watanabe, M., Williams, D.B., 2006. The quantitative analysis of thin specimens: a review of progress from the Cliff-Lorimer to the new zeta-factor methods. Journal of Microscopy 211, 89–109, https://doi.org/10.1111/j.1365-2818.2006.01549.x.

Wenk, H.R., 1976. Electron Microscopy in Mineralogy. Springer, Berlin.

White, W.B., 1974. The carbonate minerals. In V.C. Farmer, Ed., The Infrared Spectra of Minerals, 227–284. Mineralogical Society.

Williams, D.B., Newbury, D.E., Goldstein, J.I., Fiori, C.E., 1984. On the use of ionization cross sections in analytical electron microscopy. Journal of Microscopy 136, 209–218. https://doi.org/10.1111/j.1365-2818.1984.tb00529.x.

Williams, D.B., Goldstein, J.I., Heinrich, K.F.J., Newbury, D.E., 1991. Quantitative X-ray microanalysis in the analytical electron microscope. Electron Probe Quantification, Springer, Boston, MA. pp. 371–398, https://doi.org/10.1007/978-1-48992617-3_18.

Williams, D.B., Carter C.B., 1996. Transmission Electron Microscopy: A Textbook for Materials Science. Springer US, Boston, MA.

Williams-Jones, A., Wood, S., 1992. A preliminary petrogenetic grid for REE fluorocarbonates and associated minerals. Geochimica et Cosmochimica Acta 56, 725738.

Williams-Jones, A., Samson, I.M., Olivo, G,R., 2000. The Genesis of Hydrothermal fluorite-REE deposits in the Gallinas Mountains, New Mexico. Economic Geology 95, 327-342. https://doi.org/10.2113/gsecongeo.95.2.327

Williams-Jones, A., Migdisov, A., Samson, I., 2012. Hydrothermal Mobilisation of the Rare Earth Elements - a Tale of ”Ceria” and ”Yttria”. Elements 8, 355–360. https://doi.org/10.2113/gselements.8.5.355

Winter, J.D., 2001. An Introduction to Igneous and Metamorphic Petrology. Prentice Hall Inc., Upper Saddle River.

Wood, J.E., Williams, D.B., Goldstein, J.I., Lorimer, G.W., Jacobs, M.H., 1984. Determination of Cliff-Lorimer k factors for a Philips EM 400T. Quantitative Analysis with High Spatial Resolution. The Metal Society London, 24–30.

Wood, S., 1990. The aqueous geochemistry of the rare-earth elements and yttrium 1. Review of available low-temperature data for inorganic complexes and the inorganic REE speciation of natural waters. Chemical Geology 82, 159–186. https://doi.org/10.1016/0009-2541(90)90080-Q

Wu, X., Meng, D., Pan, Z., and Yang, G., 1998. Transmission electron microscope study of new, regular, mixed-layer structures in calcium-rare-earth fluorcarbonate minerals. Mineralogical Magazine 62, 55–64, https://doi.org/10.1180/002646198547468.

Wu, X., Yang, G., Meng, D., Pan, Z., Li, D., Dai, J., 1994. A study of new polytypes in the calcium rare-earth fluoro-carbonate minerals under high resolution transmission electron microscope. Acta Petrologica et Mineralogica 13

Yang, G.M., Tao, K., Zhang, P., 1998. The symmetry transformations of modules in baestnasite-vaterite polysomatic series. Neues Jahrbuch für Mineralogie Monatshefte, 1–12.

Yuan, Y., Shi, G., Yang, M., Wu, Y., Zhang, Z., Huang, A., Zhang, J., 2014. Formation of a hydrothermal kaolinite deposit from rhyolitic tuff in Jiangxi, China. Journal of Earth Science 25, 495–505, https://doi.org/10.1007/s12583-014-0439-1

Zeug, M., Nasdala, L., Ende, M., Habler, G., Hauzenberger, C., Chanmuang N., C., Škoda, R., Topa, D., Wildner, M., Wirth, R., 2021. The parisite–(Ce) enigma: challenges in the identification of fluorcarbonate minerals. Mineralogy and Petrology 115, 1–19. https://doi.org/10.1007/s00710-020-00723-x

Zhou, B., Li, Z., Chen, C., 2017. Global Potential of Rare Earth Resources and Rare Earth Demand from Clean Technologies. Minerals 20 7, 203. https://doi.org/10.3390/min7110203

Acknowledgements

A large number of people have contributed to the scientific and personal support that made this thesis and my research years a fulfilling experience. I am profoundly grateful to all of them.

First and foremost, I would like to express my deepest gratitude to **Prof. Giancarlo Capitani**, my Ph.D. supervisor, for his guidance and support throughout these years. His mentorship has been fundamental in my academic journey, and his enthusiasm for mineralogy and electron microscopy has deeply inspired my own passion for this field. It is incredible how much can be understood by observing minerals at the nanoscale. Beyond his academic excellence, he is an exceptional person and professor, whose dedication and kindness have been a constant source of motivation and inspiration.

I extend my thanks to **Prof. Patrizia Fumagalli**, who warmly welcomed me and taught me how to use Raman spectroscopy. Her kindness and patience have not only enriched my scientific knowledge but also provided a remarkable example of professionalism and dedication.

I am equally grateful to **Prof. Fernando Nieto** and **PhD. Maria del Mar**, who kindly hosted me at the Centro de Instrumentación Científica at the University of Granada. Their expertise and mentorship were fundamental in shaping my academic and personal growth during time there.

Many colleagues and collaborators have provided valuable scientific support throughout this work. I am especially thankful to **Dr. Paolo Gentile**, who provided a significant portion of the samples studied in this thesis. His guidance during our mineral exploration in Cuasso al Monte, along with his assistance with SEM analyses and insightful discussion about minerals, proved invaluable. A special thanks to **Dr. Fabrizio Vergani** for his support during the countless hours spent calibrating the EDS and WDS spectrometer, and to **Dr. Lucia Galimberti**, who generously taught me how to prepare the samples and offered continuous help since my bachelor's thesis. **Prof. Enrico Mugnaioli** deserves my gratitude for introducing me to electron diffraction and for his guidance in acquiring and processing the data. Similarly, I extend my thanks to **Prof. Marco Merlini** for his assistance with single-crystal X-ray diffraction data acquisition and analysis. I am also grateful to **Prof. Luigi Folco**, who kindly prepared the focused ion beam sections.

Finally, I am indebted to **Prof. Bernard Grobéty** and **PhD. Mauro Gemmi** for reviewing this thesis and providing valuable suggestions and advice for improving the manuscript.

A special thank you goes to all the colleagues who may not have been directly involved in this thesis but collaborated with me on scientific projects and public engagement initiatives. Each of you has left an indelible mark on my journey, and I carry your contributions with me.

Lastly, I am profoundly grateful to my friends and family for their patience, encouragement, and support throughout my studies. Without you, this achievement would not have been possible.